Department of Earth and Planetary Sciences
Massachusetts Institute of Technology
Cambridge, Massachusetts 02139

RESEARCH IN SEISMOLOGY

Final Report to

Air Force Office of Scientific Research

ARPA Order No. - 1827-1 / 2134

Program Code No. - 2F10

Name of Contractor - Massachusetts Institute of Technology

Effective Date of Contract - 1 April 1971

Contract Expiration Date - 31 May 1975

Amount of Contract - $787,389.00

Contract No. - F44620-71-C-0049

Principal Investigators - Frank Press, 617/253-3382
M. Nafi Toksöz, 617/253-6382
Keiiti Aki, 617/253-6397
Sean C. Solomon, 617/253-3786

Program Manager - William J. Best, 202/693-0162

Short Title of Work - Research in Seismology

Sponsored by
Advanced Research Projects Agency
ARPA Order No. 1827-1 / 2134

Qualified requestors may obtain additional copies from the Defense Documentation Center. All others should apply to the National Technical Information Service.

Approved for public release, distribution unlimited.

SECURITY CLASSIFICATION OF THIS PAGE (When Data Entered)

REPORT DOCUMENTATION PAGE

READ INSTRUCTIONS BEFORE COMPLETING FORM

1. REPORT NUMBER: AFOSR TR-75-1663
2. GOVT ACCESSION NO.
3. RECIPIENT'S CATALOG NUMBER

4. TITLE (and Subtitle): RESEARCH IN SEISMOLOGY.
5. TYPE OF REPORT & PERIOD COVERED: Final 4/1/71 - 5/31/75
6. PERFORMING ORG. REPORT NUMBER

7. AUTHOR(s): Frank Press, M. Nafi Toksöz, Keiiti Aki, Sean C. Solomon
8. CONTRACT OR GRANT NUMBER(s): F44620-71-C-0049, ARPA Order-1827

9. PERFORMING ORGANIZATION NAME AND ADDRESS: Massachusetts Institute of Technology, Cambridge, MA 02139
10. PROGRAM ELEMENT, PROJECT, TASK AREA & WORK UNIT NUMBERS: 62701E, AO 1827-10

11. CONTROLLING OFFICE NAME AND ADDRESS: Advanced Research Projects Agency/NMR, 1400 Wilson Boulevard, Arlington, VA 22209
12. REPORT DATE: 1975
13. NUMBER OF PAGES: 187

14. MONITORING AGENCY NAME & ADDRESS (if different from Controlling Office): Air Force Office of Scientific Research/NP, 1400 Wilson Boulevard, Arlington, VA 22209 — 189 p.
15. SECURITY CLASS. (of this report): UNCLASSIFIED
15a. DECLASSIFICATION DOWNGRADING SCHEDULE

16. DISTRIBUTION STATEMENT (of this Report)

Approved for public release; distribution unlimited.

Final rpt. 1 Apr 71-31 May 75.

17. DISTRIBUTION STATEMENT (of the abstract entered in Block 20, if different from Report)

DDC RECEIVED JAN 22 1976 D

18. SUPPLEMENTARY NOTES

19. KEY WORDS (Continue on reverse side if necessary and identify by block number)

Attenuation
Body Waves
Earthquakes
Earth structure
Seismic arrays
Seismic discrimination
Seismology
Source mechanism
Surface waves
Wave propagation

Among the topics included in this report are:

20. ABSTRACT (Continue on reverse side if necessary and identify by block number)

The research efforts under the contract F44620-71-C-0049 "Research in Seismology" are summarized. These include: studies in seismic source theory, inversion of seismic data for three dimensional earth structures, regional crust-upper mantle structures under LASA and in Asia, source mechanisms of Asian earthquakes, and attenuation and scattering of seismic waves. A list of published papers and theses completed during the contract period is given at the end of the report.

DD FORM 1 JAN 73 1473 EDITION OF 1 NOV 65 IS OBSOLETE

UNCLASSIFIED 220 000

SECURITY CLASSIFICATION OF THIS PAGE (When Data Entered)

ABSTRACT

The research efforts under the contract F44620-71-C-0049 "Research in Seismology" are summarized. These include: studies in seismic source theory, inversion of seismic data for three dimensional earth structures, regional crust-upper mantle structures under LASA and in Asia, source mechanisms of Asian earthquakes, and attenuation and scattering of seismic waves. A list of published papers and theses completed during the contract period is given at the end of the report.

TABLE OF CONTENTS

1. INTRODUCTION

The work done under the contract F44620-71-C-0049 "Research in Seismology" during the period 1 April 1971 - 31 May 1975 can be grouped into three broad categories:

1. Seismic source mechanisms.
2. Earth structure.
3. Seismic wave propgation, scattering and attenuation.

Under each one of the three areas both theoretical studies and applications to field data were carried out. In source mechanism studies, radiation of seismic waves from an expanding fault model was calculated numerically, and source mechanisms and focal depths of earthquakes in central Asia were determined from surface wave spectra. In earth structure, techniques were developed to invert the travel time in terms of the three dimensional earth models. These techniques were utilized to determine regional structure (under LASA and under California) and lateral velocity variations in the earth's mantle.

In summarizing research efforts, generally the results are described very briefly. When the material is available in open literature in the form of published papers, referable theses, or papers in press nearing publication, only the abstracts are given. Recently completed papers are included in full in the report. In addition to these, a list of publications and a list of theses completed during the contract period are given at the end.

2. SEISMIC SOURCE MECHANISMS: THEORY

2.1 Dynamics of an expanding circular fault by R. Madariaga

ABSTRACT

We study a plane circular model of a frictional fault using numerical methods. The model is dynamic since we specify the effective stress at the fault. In one model we assume that the fault appears instantaneously in the medium; in another, that the rupture nucleates at the center and that rupture proceeds at constant subsonic velocity until it suddenly stops. The total source slip is larger at the center and the rise time is also longer at the center of the fault. The dynamic slip overshoots the static slip by 15%-35%. As a consequence, the stress drop is larger than the effective stress and the apparent stress is less than one half the effective stress.

The far-field radiation is discussed in detail. We distinguish three spectral regions. First, the usual constant low frequency level. Second, an intermediate region controlled by the fault size and, finally, the high frequency asymptote. The central region includes the corner frequency and is quite complicated. The corner frequency is shown to be inversely proportional to the width of the far-field displacement pulse which, in turn, is related to the time lag between the stopping phases. The average corner frequency of S waves ν_o^s is related to the final source radius, a, by $\nu_o^s = .21\ \beta/a$. The corner frequency of P waves is larger than ν_o^s by an average factor of 1.5.

2.2 Time-Dependent Strain Accumulation and Release at Island Arcs: Implications for the 1946 Nankaido Earthquake by A.T. Smith, Jr.

ABSTRACT

Underthrusting and the elastic-rebound theory are consistent with the gross static deformations after earthquakes for island-arc regions such as Japan, Alaska, and Chile. Yet anomalous, time-dependent post-earthquake adjustments suggest additional processes. Here the asthenosphere or mantle becomes the element that both determines the post-seismic deformation and controls the accumulation of strain. The lithosphere and asthenosphere represent a coupled system. A large earthquake strains the entire system; stress relaxation in the viscous asthenosphere follows and allows the post-seismic readjustments.

The convergence zone is first considered as a semi-infinite, elastic plate overlying a viscoelastic foundation. Analytic solutions for short-period deformations place bounds on the behavior for the surface deformations, boundary conditions on the fault interface, and stress-propagation following an earthquake. Detailed models are then considered using a novel, time-dependent, finite element solution for the convergence zone. The solution avoids propagation of errors in time and readily accommodates inversion theory. The method clearly defines the behavior for realistic models.

Thus, scaling with the fault depth and lithospheric thickness controls the shape for simple, planar fault models, while the time scale depends on the asthenospheric viscosity. Different boundary conditions imposed on the fault, whether a constant dislocation or a constant stress with time, strongly affect the resulting deformations and stresses. Finally, stresses introduced by thermal density anomalies within the descending lithosphere are compared to earlier models and focal mechanisms near Hokkaido.

Generalized-matrix inversion theory now places bounds on the effective viscosity and fault parameters using geodetic data, focal mechanisms, and tectonic setting for the 1946 Nankaido earthquake (M 8.2) in southwest Japan. Using the assumption of stress relaxation in the asthenosphere, the data constrains the fault geometry to a shallow 15° dip, followed by a 60° dip from 26 km depth to the base of the lithosphere at 60 km depth. Near the hypocenter the slip is 3 meters, while the maximum slip is less than 15 meters. Other models with constant dip or shallower dip beyond 25 km do not satisfy these constraints. The viscosity of the asthenosphere now becomes 10^{20} poise. The results suggest segmentation of the lithosphere and deformations that generate the embayed shoreline, sedimentary basins off southwest Japan, seismicity, and focal mechanisms.

2.3 A Dislocation Approach to Plate Interaction by

R.L. Brown, Jr.

ABSTRACT

A dislocation can be described in terms of a surface of discontinuity or the line which circumscribes this surface. We have applied the solutions of Yoffe (1960) and Comninou (1973) for an angular dislocation line to the problem of calculating the fields due to general polygonal dislocations.

Next, a numerical method has been developed explicitly for finite sources (Finite Source Method or FSM) which allows the computation of fields from a dislocation that penetrates several layers of a layered half-space. The speed of the FSM allows the calculation of many models which are not economically possible by other means. It is used here to model earthquakes in layered media and plate bottom effects due to the interaction of lithospheric plates.

Finally, the problem of the mutual interaction of lithospheric plates in relative motion has been posed in terms of dislocation theory (anti-dislocations). Dislocation models of various portions of the San Andreas fault in California are proposed and evaluated by comparing them with seismic and geodetic data. We find, for example, that fault creep near Hollister acts to obscure any locking at depth and that as much as 70% of the fault could be locked (down to 20 km) and still be consistent with the geodetic data.

The models also suggest that the depth of locking (or non-slipping portion of the fault) varies from 10 to 80 km along the San Andreas. Under San Francisco the depth of locking appears to be 20 to 40 km while just north and south of this region the locking is from 10 to 15 km deep. Our models are also indicative of a more northerly component of motion for the Pacific with respect to the American plate than would be expected if the San Andreas were a simple strike-slip fault. South of Cholame the depth of locking begins a rapid increase and appears to lock to 80 km in the Tejon bend portion of the San Andreas. We are not able, however, to distinguish between an actual locking of the fault, capable of taking high stresses, or simply a low stress state.

2.4 On the Interaction of Two Scales of Convection in the Mantle by F.M. Richter and B. Parsons

ABSTRACT

A system in which convection takes place in the upper mantle on two distinct horizontal length scales is proposed. This is consistent with the existence of the plates themselves, the relatively constant heat flux background in older ocean basins, and the knowledge of convection in fluid layers gained from laboratory and numerical experiments.

The large-scale circulation consists of the plates themselves and the return flow necessary to conserve mass. The small-scale flow, analogous to Rayleigh-Benard convection or variants of this, which have been the main target of numerical study, provides the necessary vertical heat transport in the upper mantle that supplies the required heat flux at the base of the lithosphere. The depth of convection is taken to be down to the 650-km seismic discontinuity, and this depth characterizes the horizontal length scale of the small-scale convection. This system is studied by means of a set of laboratory experiments that explore the interaction of the small-scale convection with the large-scale flow. The experiments show the plausibility of convection on two scales. Furthermore, they suggest that beneath fast-moving plates (absolute velocities around 10 cm yr^{-1}) the small-scale convection will align itself as rolls in the direction of the large-scale flow in geologically short times. However, beneath very slow moving plates the times required for the alignment of convective rolls are long in comparison with times over which no changes in plate motions are to be expected. Here the convective planform is more likely to take the form of upwelling and downwelling spouts. Thus this simple system of a convecting layer beneath a moving boundary contains the possibility of explaining a wide variety of surface features. Observational tests of the consequences

of the two-scale idea are suggested, and the assumptions on which this idea is based are critically discussed.

3. SEISMIC SOURCE MECHANISMS: ASIA

3.1 Static and Dynamic Fault Parameters of the Saitama Earthquake of July 1, 1968 by K. Abe

The source mechanism of the Saitama earthquake (36.07°N, 139.40°E, M_s = 5.4) of July 1, 1968, is studied on the basis of P-wave first motion, aftershock, long-period surface-wave data and low-magnification long-period seismograms recorded in the near-field. A precise location of the aftershocks is made using P and S-P time data obtained by a micro-earthquake observatory network. The synthetic near-field seismograms based on the Haskell model are directly compared with the observed near-field seismograms for wave and amplitude to determine the dynamic fault parameters. The results obtained are as follows: source geometry, reverse dip slip with considerable right-lateral strike-slip component; dip direction, N6°E; dip angle 30°; fault dimension, 10 x 6 km^2; rupture velocity, 3.4 km/sec in the direction S30°E; average dislocation, 92 cm; average dislocation velocity, 92cm/sec; seismic moment, $1.9 \cdot 10^{25}$ dyn-cm; stress drop, 100 bar. The effective stress is about the same as the stress drop.

For major earthquakes in the Japanese Islands, the dislocation velocity, $\langle\dot{D}\rangle$, is found to be proportional to the stress drop, σ. This relation can be expressed by $\langle\dot{D}\rangle \simeq (\beta/\mu)\sigma$, where β is the shear velocity and μ is the rigidity. This result has an importance in engineering seismology because the stress drop scales the seismic motion in the vicinity of an earthquake fault.

3.2 A Fault Model for the Niigata Earthquake of 1964 by K. Abe

ABSTRACT

The source mechanism of the Niigata earthquake of 1964 ($M_S \sim 7.5$) is studied in detail on the basis of the P wave first motion, S wave polarization angle, long-period surface wave, aftershock, precise levelling, tide gage, and tilt measurement data. The long-period surface wave data and geodetic data are interpreted consistently in terms of a thrust fault reaching the earth's surface and having a dip of 56° toward N81°W, a dimension of 80 km (length) x 30 km (width), and an average dislocation of 3.3 m. The seismic moment is 3.2×10^{27} dyne-cm. The stress drop is estimated to be 70 bars. This value is not very different from the stress drops obtained for moderate to large shallow earthquakes which occurred in the Japan Islands. The fault plane

geometry obtained here is slightly different from that determined from the P wave first motions. Combining this result with the weak beginning of the initial P waves, we may interpret the entire faulting process in terms of a multiple faulting which consists of the two events: the initial localized rupture is followed, after about 4 sec, by the major faulting, which is responsible for the excitation of long-period waves.

3.3 Thermal and Mechanical Models of Continent-Continent Convergence Zones by P. Bird and M.N. Toksöz

ABSTRACT

The thermal regimes of continent-continent convergence zones are modelled by a finite-difference technique, assuming that there is some subduction of continental crust. Gravity and heat flow profiles are generated from the thermal models. Subducted crust and slab remain cool except at the upper surface where frictional heating is important. Crustal rocks may be metamorphosed or melted by friction while the plates are converging, or by radioactive self-heating more than 30 m.y. after the plates have stopped. In the former case, melting requires frictional shear stresses between 500 and 2000 bars at a plate velocity of 5 cm/year. At lower velocities the upper limit of frictional stress is greater.

The total work performed in continental subduction may be minimized if the angle of underthrusting becomes more shallow, changing the location of subduction.

A model for the geometry of oceanic and continental slabs in the Zagros Mountains is presented which satisfies gravity, heat flow, seismic, and geological constraints. Continental underthrusting is beginning along a new fracture at the edge of the Persian Gulf, isolating the Arabian continental shelf from the subduction process. Slippage along this fault is Pleistocene and probably does not exceed 30 km. Subduction of continental crust at the Crush Zone is probably insignificant.

Introduction

Subduction of continental crust as the cause of orogenies and mountain-building is a concept with a long history. The geologic evidence is clearest in the Alpine-Himalayan belt, and as early as 1916 Emile Argand developed a theory of Alpine orogeny in which Africa moved North and overrode Europe. Unlike the previous geosynclinal theory of Hall (1860) and Dana (1873), this provided an explanation for the asymmetry of many mountain ranges, in which deformation proceeds from the mafic to the silicic side with a series of overthrusts in one direction. More recently, the theory of plate tectonics has suggested a mechanism and allowed us to identify certain eugeosynclines as converging plate margins towards which an opposing continental shelf (the miogeosyncline) is transported by sea-floor spreading and subduction (Dewey and J. Bird, 1970). One natural explanation of the thick low-density roots of mountain ranges is that the collision of continents is followed by some amount of underthrusting of continental crust.

In continental convergence belts, particularly the Himalayas and the Zagros, geology records both the oceanic and continental phases of subduction. On the Northern margin of both ranges there is an elevated plateau, intruded by voluminous andesites and basalts associated with the former subduction of an oceanic plate beneath the plateau. Adjacent to the plateau there is a suture zone with steep contacts,

deformed turbidities with clastic blocks (trench sediments) and ultramafic ophiolite complexes indicating the location of the first contact between continents. These suture zones, however,are not very active seismically or geomorphically. Instead, the elevation of the mountain range occurs in a folded and overthrust zone from 100 to 300 km wide on the other side of the suture zone. These deformed zones are not regionally metamorphosed, but the Himalayan orogenic belt contains scattered granites which may originate along the thrust plane from frictional melting as the crust of the mountain range thickens by underthrusting. The convergence belts are terminated by a downwarping alluvial basin, formed over the advancing plate as it bends down to begin subducting under the range. A possible sequence of development of these features is given by Figure 1, in which the Zagros stage is shown as B and the Himalayan stage as C.

The location of crustal subduction is further marked by seismicity and gravity anomalies. Earthquakes occur in diffuse bands dipping away from the margin of the alluvial foredeeps. Fault-plane solutions for these events (Fitch, 1970; Nowroozi, 1972) confirm the mechanisms to be shallow underthrusting. The Bouguer gravity anomaly fields (Wilcox et al., 1972; Qureshy, et al., 1974) reveal large minima elongated along the ranges and centered between foredeep and suture zone. This is additional evidence of continental subduction.

In this paper we have assumed the validity of plate tectonics and convergence by subduction as a starting point. This allows calculation of the critical geophysical parameters of temperature, density, seismic velocity, and stress, and it is only with knowledge of these fields that we can assess the self-consistency of the plate-tectonic interpretation of mountain-building. With this goal, we have considered a number of idealized cases illustrating general principles, and progressed to an interpretation of the Zagros Mountains, in which the structures described are just beginning to develop.

We begin with a calculation of temperature fields in continental subduction. In the second section we investigate the effects of the low density of continental crust and great thickness of shield lithosphere, and the ways in which these may force the location and/or the angle of subduction to change. Finally, we present a model for the Zagros Mts., where the transition from oceanic to continental subduction has been occurring over the last million years.

Calculation of Thermal Models

Thermal modeling of downgoing slabs of oceanic lithosphere has already been performed by Minear and Toksöz (1970a) and Toksöz et al. (1971, 1973). Using the same technique, we have concentrated on the details of the shallow structure of continental

subduction zones where the vertical displacement is assumed to be less than 100 km. We begin with simple hypothetical models to show the range of possible thermal regimes.

To calculate the thermal models of converging plates of continental lithosphere we solve the heat equation

$$C \frac{\partial T}{\partial t} = \nabla(K\nabla T) + H \qquad (1)$$

where T = temperature, t = time, C is heat capacity, K is thermal conductivity, and H is heat production. In the finite difference solution of (1) we use a 41 by 41 grid with a vertical increment of 5 km. The details of the computational technique and its accuracy have been extensively discussed by Minear and Toksöz (1970a, 1970b, 1971) and Toksöz et al. (1971, 1973).

The parameters of primary interest in these calculations are subduction rate, subduction angle, and the amount of shear-strain heating. Less critical parameters are held constant from model to model; all the constants used are presented in Table 1.

Low angles of subduction, not more than 30° in dip, were employed because fault-plane solutions in continental convergence sites such as the Himalayas and Zagros have consistently shown shallow underthrusting (Fitch, 1970; Nowroozi, 1972). Also, the great buoyancy of continental crust will tend to prevent subduction at large dips, as will be discussed below.

Frictional heating (or shear-strain heating) at the top of the slab is an important parameter. These two terms are used interchangeably in this paper because the actual mechanism is unimportant in thermal modelling. Whether there is stick-slip behavior or viscous creep (Turcotte and Oxburgh, 1969) the heat production per unit area of fault is just

$$Q = \int \dot{e}\tau \, dZ = \tau V \qquad (2)$$

where Q is in ergs/cm^2-sec, τ is shear stress in dynes/cm^2, $\dot{e}$ strain rate and V is the relative plate velocity in cm/sec.

Although τ is an uncertain parameter, its upper and lower bounds can be established. Stress drops in earthquakes provide a lower limit. Evidence of metamorphism or melting in each particular range can be used to fix the shear stresses, and it will be shown that there is a universal upper limit. A set of theoretical thermal regimes are calculated for continental convergence models. The results strongly depend on model parameters, which cannot be fixed uniquely. In the models discussed below, the relative effects of different parameters are illustrated. A summary of models and model parameters are listed in Table 1.

The first case considered is that of slow convergence at 1 cm/yr and at the relatively large dip angle of 30°. Because

continental convergence occurs at the site of former oceans (as shown in Fig. 1) rather than along new lineations within a plate, there is a previously-subducted oceanic slab ahead of the continental material. This oceanic slab absorbs heat through its cold upper surface while subducting and creates a cool zone in the overriding lithosphere before the continents come together.

The thermal regime after 80 km of convergence is shown in Figure 2. Even at this low velocity the radioactivity of the crustal material has little effect. The frictional heating rate is proportional to slab velocity (equation 2) and hence is also low. Thus the continental crust remains cold except near its leading surface which is locally heated to 400°C and could undergo blueschist metamorphism. The dominant influx of cold material is also reflected in the heat flow above the slab, which is depressed by some 0.6 HFU at 40 km behind the subduction zone.

A Bouguer gravity anomaly has also been calculated for this model by assuming that the structure is flat and two-dimensional. The temperature anomalies are converted to density anomalies using thermal expansion coefficients of 3.0×10^{-5}/°C for the upper crust, 2.5×10^{-5} for the lower crust, and 3.2×10^{-5} for the mantle (Skinner, 1966). Because the oceanic slab consists mostly of cold mantle material, this is the only

contribution to its density anomaly. The continental crust introduces a large compositional density anomaly by displacing heavier mantle rock, and this overshadows the positive thermal density anomaly. By balancing the negative crustal and positive thermal mass anomalies, we calculate that this amount of subducted crust could be balanced by a minimum oceanic slab only 25 km longer than that of Fig. 2. This is assuming a mantle thermal expansion of 6×10^{-5}/°C (Sleep, 1975); for a lower coefficient the slab must be longer.

A second calculation at a lower dip is shown in Figure 3. The convergence rate of 6 cm/yr is closer to the rates computed for the Zagros and Himalayan ranges from sea-floor spreading poles and rates (LePichon, 1968). Stress has been slightly increased on the shallow parts of the fault where most earthquakes seem to occur; it is 1 kilobar for depths between 80 and 40 km, 1.2 kb for 35 to 25 km, and 1.5 kb from 20 to 10 km.

Frictional heating is 6 to 9 times greater than in the previous case, and produces a marked high-temperature zone along the top of the slab around the fault surface. Temperatures in this hot zone are above the solidus of water-saturated granite and are about 50°C below the dry-muscovite-granite solidus of Brown and Fyfe (1970). These solidus temperatures would be reached if subduction were to continue.

Heat flow and gravity anomalies associated with this model

are also shown in Fig. 3. There is a small high heat flow anomaly and broad gravity anomaly. From these, the position of the slab is only generally indicated. If local isostasy were operative during the subduction process, the region some 100 km behind the trench line would be uplifted to 3 km average elevation.

This model illustrates the possibility that frictional heating could produce strong metamorphism or partial melting in a thin zone near the fault. But it does not explain the regional metamorphism which seems to occur late in the history of each orogenic belt. To test the possibility that this orogeny is produced by radioactive heating of thickened crust, we allowed the calculation in this second case to continue for 100 m.y. with no motion of the slab. After the influx of cold surface rock stops, the extra radioactive heat production in the region of overlapped crust eventually dissipates the regional cold anomaly and creates a heated region.

The difficulty with this type of calculation is that vertical motions will not cease with the end of convergence. A doubled layer of crust will produce dramatic isostatic uplifts and rapid erosion, leading to the eventual destruction of the crustal bulge. Thus the time range over which this modelling remains valid depends directly on the rate of erosion.

The temperature field at the end of 30 m.y. with no erosion corrections is shown in Figure 4A. Dashed lines show the former

outlines of the slab. The solidus line at the base of the plate has moved upward while the hot region in the base of the overriding lithosphere has dissipated. Thus the oceanic slab begins to lose its identity. An elevation of temperatures is seen in the slab at the end of the crustal portion, but on the whole the region is still anomalously cold. The lower portion of the crust is heated above 600°C and severely metamorphosed, but nowhere in the crust is the solidus exceeded. Thus the extensive granite bodies and high grade metamorphic belts such as those contained in the Urals and the Piedmont province and Merrimack Synclinorium of the Appalachians are not explained by this model. They could be produced if the erosion rate were low (or the radioactivity higher).

In Figure 4B the same model is shown after a quiescent period of 100 m.y. Here the inherited cold anomaly has disappeared and there is a general upwarping of isotherms. Where the 800°C isotherm moves into the base of the subducted crust, general melting and formation of plutons could occur. The small positive heat flow anomaly of 0.2 HFU which is predicted would be augmented by the slow upward mass transport in response to erosion and the rapid mass transport of rising volatiles from the region of melt.

The essential problem with this mechanism for metamorphism and orogeny is the excessive time required to raise temperatures by radioactivity alone. Naylor (1971) has placed a 30 m.y. maximum duration on the Acadian orogeny (in eastern Vermont)

including the emplacement of granites, and if the orogeny resulted from continental convergence and the granites from radioactive heating then this is faster than predicted. Similarly, Oxburgh and Turcotte (1974) found that simple overthrusting and radioactive heating were insufficient to produce the East Alpine metamorphism. Thus we must reserve the hypothesis that the heat of orogeny is transported to the crust from below rather than created in it.

If the oceanic slab of Figure 2 were to become detached near the leading edge of the subducted crust (the 130 km point), it would continue to sink. The asthenosphere at over 1100°C would rise, at a rate comparable to plate velocities, to take its place. Losing heat mainly by adiabatic decompression, it could rise to only 50 km depth, diffuse heat to the crust in under 10 m.y., and cause a major thermal event.

Mechanics of Continental Convergence

Before it is possible to ascertain the maximum possible extent of continental subduction, it will be necessary to more accurately quantify the various forces involved. Body forces may be quite accurately estimated by a combination of thermal modelling, measurement of thermal expansions, and observation of surface vertical tectonics (Smith and Toksöz, 1972). Elastic and viscous bending stresses in the lithosphere have already been estimated by observations on geologically transient loading

by icecaps (Walcott, 1970a), glacial lakes (Walcott, 1970b), and oceanic subduction (Smith, 1974; Watts and Talwani, 1974). One of the most uncertain factors remaining is the level of frictional stress on the long fault surface where the greatest strains are concentrated. It is difficult to apply laboratory experiments to this problem because of the enormous complexities of continental surface rocks and the uncertainty as to how much soft sediment and water are entrained into the fault. One strength of thermal modelling is that it can set definite upper limits on the possible stresses at each depth in this complex zone.

The thickness of the fault zone is not critical to the thermal history as long as it is much less than the scale distance for heat conduction during the subduction phase. Then, the greatest part of the frictional heat produced will be transferred to the slab and overlying plate rather than expended in heating the shear zone itself. Thus the temperatures on the fault will depend only on the gross parameters of stress and plate velocity, dip angle, and initial geotherm, and not in any way upon the complex mechanics of the shear strain itself. Since all these factors except stress can be determined within fractional errors, what remains is a strong relation between shear stress and temperature.

The maximum possible shear stress at any depth along the fault will be that which causes the temperature to reach the solidus. As soon as partial melting of the rock sets in,

there is self-regulating effect which will maintain that temperature by reducing the effective viscosity or coefficient of friction. The interesting point in the case of continental subduction is that half of the rocks in the fault zone will have a grossly granitic composition and hence a very low-temperature solidus. The solidus of water-saturated granite, which is flat with pressure beyond 7 kb (Tuttle and Bowen, 1958) is not particularly relevant because significant amounts of water (2% by weight) would be consumed by the formation of partial melts. However, the solidus of Brown and Fyfe (1970) for dry granite containing muscovite may be more appropriate for the convergence zones. As shown in Figure 5, this solidus would never be reached along the fault at depths of less than 100 km without frictional heating. This is because the influx of cold material depresses the fault-zone geotherm well below the base geotherm.

To determine the shear stresses necessary for melting we used a combination of finite-difference and analytic techniques. First, we used the slab temperature program to solve for temperatures on the fault in the artificial case of no shear-strain heating. This includes the effects of slab geometry, non-linear geotherm, adiabatic compression, etc. Then, since the finite-difference grid is too course to accurately represent a thin heat source, we used asymptotic analytic formulas to calculate the values of $Q(Z)$ that would raise these fault temperatures to the solidus.

Figure 5 shows the temperatures for the artificial zero-stress case after 400 km of subduction. This distance is the approximate width of the continental-rise sediments on an Atlantic-type continental margin (Emery et al. 1970), and the assumption is that the transition from oceanic- to continental-subduction temperatures on the fault occurs gradually over the period in which sialic material begins to move into the shear zone.

In calculating the heat lost into the slab as a result of friction, we assume that conduction of frictional heat along the slab and through its base are negligible. Then the slab is modelled as a semi-infinite halfspace with a specified thermal history at the surface. This thermal history consists of a series of temperature increments ΔT_i above the zero-stress temperatures, and if the temperature varies linearly between integration points then the flux consumed is:

$$A_{slab}^{(Z_j)} = \frac{2KV\sin\theta}{\Delta Z\sqrt{\pi\kappa}} \sum_{i=1}^{j} (\Delta T_i - \Delta T_{i-1}) \left(\sqrt{\frac{z_j - z_i}{V\sin\theta}} - \sqrt{\frac{z_j - z_i - \Delta z}{V\sin\theta}}\right) \quad (3)$$

(Carslaw and Jaeger, 1959), where θ is the angle of slab dip, ΔZ is the depth interval between integration points Z_i, and κ is thermal diffusivity. Above the slab the frictional heat is assumed to be distributed in equilibrium conduction to the surface (at depths less than the scale distance), or to be working its way

into the overriding plate according to the model of a half-space whose surface temperature is changed by ΔT_i in the time required to subduct 400 km:

$$Q_{up}^{(z_j)} = \frac{\Delta T_i K}{2} \sqrt{\frac{\pi V}{\kappa (400 \text{ km})}} \qquad (4)$$

By adding (3) and (4) we find the flux that friction must produce to cause melting, and by (2) we obtain the shear stress. However, this stress is not allowed to exceed the product of hydrostatic pressure with a coefficient of friction of 0.6 (Byerly, 1966).

The results in Figure 5 indicate that the shear stress is a strong function of plate velocity and a weak function of the melting geotherm. As expected from (3), (4) and (5) the shear stresses at 1 cm/yr are greater than the stresses at 5 cm/yr by approximately a factor of the square root of the velocity ratio. For constant K, κ, θ, and z, to maintain melting we have:

$$\tau(z) \approx f(z,\theta)\ V^{-1/2} \qquad (5)$$

Stress decreases with velocity, or conversely that there may be a critical plate velocity below which continental subduction is prevented by friction. The importance of this effect depends critically on the density anomaly of the cold oceanic slab which provides the driving force.

This density anomaly resulted from the initial thermal contraction of the mantle material forming the oceanic plate when it cooled near a mid-ocean ridge. The amount of contraction can be estimated from the isostatic balance of plates. The elevation with respect to old sea floor of continents is 5 to 6 km and of mid-ocean ridges is 3 to 4 km. Noting that mid-ocean ridges give a reasonable sample of the asthenosphere with which we want to compare the slab, we find that the weight excess of a unit section of oceanic slab is about 8×10^8 dyne/cm^2 with respect to the asthenosphere and that the figure for the net mass deficiency of continental lithosphere is about -5×10^8 dyne/cm^2. Unless these estimates are in gross error, the comparable buoyancy of continental plates and negative buoyancy of oceanic plates with respect to the asthenosphere implies that hundreds of kilometers of continental crust could be subducted if the plate behaved as a unit.

However, the integrity of the plate is probably not preserved. Whatever the driving force is in oceanic subduction, the deviatoric stress field at shallow depths near the fault plate must be vertical tension and horizontal compression. The additional deviatoric stress produced by the buoyancy of subducted continental crust would be vertical tension below the crust and vertical compression above. This extra stress would be greatest and would interfere constructively with the driving stresses near the lower tip of the crust. Subsequent shearing would thus tend to occur within the subducting plate at the base of the subducted crust.

If the new fault dipped in the same direction as the old fault, it would outcrop in the downing plate away from the old convergence zone. In the case of an island arc-continent collision, a new fault conjugate to the old fault would permit the subduction zone to reverse polarity. In either case the slab might detach at the base of the subducted continental crust along the old fault and a conjugate fault. Hot material upwelling from below to replace the slab would provide a large heat source.

Another means of approaching this problem is to consider the horizontal convergence of the two plates to be dictated by distant driving forces which impose a displacement boundary condition. Then by focussing only on the local forces which act at shallow depths to oppose the subduction process, one can seek the geometry of underthrusting which will minimize these forces. This must be the geometry of the fault which dominates the subduction process, because it is the one that allows the greatest displacement or displacement rate.

The major forces opposing subduction arise from three effects: friction between one lithospheric plate and the other on the active fault, viscoelastic resistance to the bending of the downgoing plate, and the bouyancy of continental crust. In the case of oceanic subduction, the third force is absent and a balance must exist between the other two. That is, subduction does not occur through one plate turning straight down because this would imply tremendous strain and viscoelastic

resistance in that plate. Subduction also does not occur at extremely shallow angles because then the frictional stress would act over a tremendous fault area. At some intermediate angle of dip the total resistance is minimized, and subduction proceeds stably over long intervals.

When continental convergence begins there are two changes which affect this balance. The first is the change from the bending of oceanic to continental lithosphere, and this takes place immediately. Continental shield lithosphere may have a thickness of about 140 km (Toksöz et al., 1967) or about twice as thick as old oceanic plates (Forsyth, 1973). Thus it is considerably more resistant to bending and shearing. The same bending moment will produce only one-eighth of the previous elastic bending, and the same shear will produce only one-half the previous viscous strain rate. This effect will force an increase in the radius of curvature of the lithospheric bend, so that downwarping begins in front of the old trench position and thrusting proceeds at a shallower dip. This new regime could develop soon after convergence if a new, more shallow-dipping fault were to form in the leading edge of the plate, as discussed above.

The second change in the force balance develops gradually, as continental crust on top of the subducting plate is carried down below its normal isostatic level. Its buoyancy then acts to oppose further convergence and downward motion, and the

magnitude of this buoyancy grows linearly with time. Thus it becomes increasingly advantageous to form new and shallower thrust faults which require less vertical displacement of the subducted crust for the same amount of horizontal convergence. As these faults form the subducted crust may become detached from the underlying plate and be itself underthrust as convergence continues.

We have shown that in the case of continental plates converging at a high velocity, continental subduction at shallow dips is a strong possibility. The resisting forces of gravity, friction, and bending could be balanced by the known driving mechanism of sinking of dense oceanic lithosphere. There is the interesting suggestion that convergence of continents will cause both the position and dip of the active inter-plate thrust plane to change. Much further work will be required before the exact mechanisms can be predicted in proper sequential order, but the stress, density and temperature constraints derived here will be essential in any attempt to predict this behavior. As an intermediate step, we will begin consideration of individual mountain ranges where continental subduction may be occurring, and test the geologic and geophysical data available against the predictions of models such as these.

Tectonics of the Zagros

The evidence of marine paleomagnetism strongly suggests that the Zagros region of Iran is the youngest continental convergence zone on the Earth. The relative motion of Arabia and central Iran can be calculated by vector addition of the motion of North America away from Europe to the motion of Africa with respect to North America (Pitman and Talwani, 1972) plus a final addition of the opening motion at the Red Sea. This we interpret from the results of Phillips (1970) to have occurred at 2 cm/yr for the last 1.5 m.y., giving a final sum of 4.7 cm/yr convergence about a pole near 37°W, 25°N for the Zagros. Comparison of this figure with reasonable estimates of the total crustal shortening in the range implies a Pleistocene age for the collision of Arabia and Iran.

The geology in the Zagros region is described by Stöcklin (1968) and Haynes and McQuillan (1974). Haynes and McQuillan present extensive evidence to show that the Zagros Crush Zone which marks the northeast limit of deformation is the site of a Tertiary oceanic subduction zone, at which this portion of the Tethys Ocean was consumed. The presence of andesitic volcanism from the Eocene to the Recent along a line some 100 to 200 km Northeast of the Crush Zone (Figure 6) indicates clearly the polarity of the zone, with the oceanic slab dipping beneath central Iran. Thus, the main folded belt of the Zagros represents the former continental shelf of Arabia, with its thickening wedge of 3 to 5 km of post-Jurassic sediments and evaporites.

Many geologic interpretations of this range have ascribed the 220 km-wide band of folding and faulting as the result of decollement on the layers of salt as the basement of the range is thrust under Iran at the Crush Zone. Chapple (1975) has shown that this is mechanically feasible if the salt layers are continuous. While this interpretation suggested by Dewey and J. Bird (1970), meshes nicely with our simple theoretical models, it fails to explain the distribution of seismicity, the regional gravity anomaly, or the present vertical tectonics. These factors can only be explained if there are two major planes of underthrusting rather than one.

The pattern of seismicity as relocated by Nowroozi (1971) shown in Figure 6 is concentrated in front of the Crush Zone rather than behind it, where events would occur if Arabia were being subducted from this line toward the Northeast. These earthquakes cannot be attributed to plate bending because Nowroozi (1972) and Akasheh (1973) have found them to have nodal-plane solutions indicating shallow thrusting. Also, the pattern of Bouguer gravity anomalies reported by Wilcox et al. (1972) (Figure 7) shows that the Zagros gravity low begins from as far Southwest as the edge of the Persian Gulf. As Figures 2 and 3 illustrate, it is impossible to produce any such anomaly with only a slab dipping from the Crush Zone. Finally, there is the existence of the Mesopotamian Trough including the Persian Gulf to be explained. This linear foredeep, which

thickens towards the Northeast and is actively subsiding, forms an elevation couple with the Zagros Range that indicates a reverse fault on the NE margin of the Trough.

Therefore, our preferred model of Zagros tectonics involves two major thrust planes surrounding an internally-deformed median block. A predominantly oceanic slab of lithosphere with oceanic crust and sedimentary deposits has been subducted at the trench location now represented by the Crush Zone (Figure 8). The oceanic slab is the former floor of the Tethys Ocean, and the sediments are those of the former Arabian continental rise. The presence of active volcanoes behind this line in Iran indicates that motion of this oceanic slab is continuing or only recently halted.

As the sediments of the main range are of continental shelf origin, they overlie a normal continental crust of perhaps 33 km thickness. This crustal block makes the Zagros continental lithosphere buoyant as well as rigid and it would therefore resist subduction along the steeply-dipping plane of oceanic subduction. Instead, this block appears to have absorbed about 50 km of continental convergence by internal deformation along numerous minor thrust faults. This shortening, which would result in crustal thickening, is not expressed at the surface by thrusts because of the independent mobility of the sediments above the lubricating salt layers. Instead, the competent carbonate layers form draped folds over each major basement fault.

Primarily to accomodate the greater flexural rigidity of the Arabian shield lithosphere, the locus of tectonic deformation has moved further Southwest in the Pleistocene. A major low-angle thrust dipping NE has formed along the former hinge line of the Arabian continental shelf, and this is responsible for the formation of the Mesopotamian Trough. The inferred fault would surface beneath a deep layer of Recent alluvium, but its location may be traced along the boundary of the stable area on the Tectonic Map of Iran (Stöcklin and Nabavi, 1973) which coincides with the SW limit of seismicity and the edge of the Persian Gulf (Fig. 6).

In order to model this orogenic zone, information is needed on the dips of both slabs. This was obtained from a compilation of earthquake locations by Nowroozi (1971) shown in Figure 9. Relatively few events are associated with the oceanic slab, which may be inactive or detached, but they indicate a dip near 30°. The majority of seismicity forms a diffuse band dipping about 15° from the Persian Gulf margin where the latest thrusting is occurring. The apparent length of this band does not indicate the amount of continental subduction, however, because any new major thrust is expected to be seismic along its whole surface.

For lack of specific information, we must assume that the lithosphere in this model is of typical oceanic type. The oceanic slab is taken to be 70 km thick; model parameters are

given in Table 1. It could reasonably be thicker if it is as old as Permian (Dewey et al. 1973). The continental part of the plate is thickened to 140 km (Knopoff and Fouda 1975) and has a low radioactivity, required to match the average heat flow value of 0.88 HFU reported by Coster (1947).

The andesite volcanism (Figure 6) behind the Crust Zone is caused either by frictional heating or by secondary back-arc type convection (Andrews and Sleep, 1974). As we are unable to model the latter, we have set the frictional stress on the subducting oceanic plate at 4 kb (the maximum shear strength of olivine from Kohlstedt et al. 1975) from 40-90 km depth during the initial period when it was moving at 2.7 cm/yr. This creates a high-temperature zone in the Iranian plate beneath the volcanic line (Figure 8).

In the second stage of the model the oceanic plate probably carries traces of continental rise sediments into the subduction zone. From this point we have controlled the stresses so that the melting point of granite is not exceeded. Melting occurs below 40 km depth, and this provides an explanation of the synorogenic granites reported by Wells (1969) in the Crush Zone, although considerable erosion or magma upwelling must be assumed to reconcile the occurrence and the source.

About one million years ago this slab stopped or slowed considerably and deformation moved to the southwest. At this

point we introduce a new continental slab dipping from the Persian Gulf. Although the total convergence velocity increased to 4.7 cm/yr before this time, the new slab is assumed to subduct at only 2.6 cm/yr because of simultaneous crustal shortening to the NE. Melting has not had time to develop on this new fault, so the stress limits of the previous section do not apply. Instead we set frictional stress on the upper parts of the fault equal to hydrostatic pressure multiplied by a coefficient of friction of 0.4 in order to match the heat flow at the surface. Deeper parts of the fault are again limited to 4 kb, although these stresses cannot be resolved from surface heat flow.

This heat flow was computed from oil-well temperature profiles in 3-5 km deep wells supplied by the National Iranian Oil Company. Only smooth monotonic profiles were used. Heat flow was determined by least-squares matching of these points to theoretical temperature profiles calculated using the conductivity values and derivatives of Asmari Limestone reported by Clark (1966). The results show a gradual increase of heat flow from 0.90 to 1.15 HFU as the fault is approached from the northeast (Figure 10).

In a case like this where high temperatures have not yet developed, the fault surface separating the plates would be a natural site for earthquakes, and it is possible that the seismic waves from these events will be useful in defining the position of the slabs. We have traced rays in three dimensions from a hypothetical earthquake located at a depth of 20 km on the fault

in our first theoretical model. Using the temperature field of Figure 2, mantle P-wave velocity anomalies were calculated using derivatives appropriate for peridotite. In the crustal portion, surface velocities were translated downward. These anomalies are superimposed on a modified Jeffreys-Bullen velocity structure with a 30 km crust and a low velocity zone. Rays were traced from the event at a variety of azimuths and angles of incidence (Julian, 1970, Sleep, 1973). Travel-time residuals were calculated relative to a set of rays traced through an unperturbed model These residuals are plotted in Figure 11A using the azimuth and angle of incidence of each ray at 150 km depth, below the anomalous structures. In the annulus of useful rays, all waves arrive late because of the additional subducted crust. The maximum delay of 1.0 to 1.3 sec occurs for waves travelling in the downdip direction through the slab. This delay is reduced for large angles of incidence in the downdip direction by the presence of the fast oceanic slab ahead of the continental lithosphere.

In the absence of very accurately located earthquakes in the Zagros, we chose to look at the travel time anomalies with the inverse procedure using a station located in the Zagros region and earthquakes distributed so as to give good azimuthal and incidence coverage. The WWNSS station at Shiraz was used for this purpose. A plot of observed travel-time residuals at Shiraz derived from the I.S.C. Bulletins covering the period of

1968-69 are shown in Figure 11B. This does not show any clear variation of travel-time residuals across the strike of the range, so it is purely negative evidence that continental material has not yet been subducted beneath Shiraz on a large scale.

The most important evidence controlling our model is the distribution of Bouguer gravity anomalies, because these principally reflect the presence of excess sialic crust below the 33 km reference thickness. Data compiled by the U.S. Air Force for the Zagros between 46° and 56°E is shown in Figure 10 in the form of one-degree averages projected parallel to the Crust Zone. Some of the scatter is due to the reduction of the anomaly by edge effects near the ends of the range, so our two-dimensional model will be fitted to the maximum anomaly amplitudes in the central (Shiraz) cross-section.

This profile is contaminated by the regional -130 mg anomaly of the Central Iranian plateau, which probably predates the collision. To remove this effect, we assume that the plateau is compensated by a thick 40 km crust which extends up to the NE dipping plane of oceanic subduction, and calculate the edge effects accordingly. We also illustrate a probable overestimate of the gravitational effect of the Mesopotamian Trough (assuming a 600 m downwarp). The remainder of the anomaly must be due to crustal thickening in the Zagros.

However, the gradients of this anomaly are too low to be matched to a dipping-slab model like those of Figures 2 and 3. The best fitting dip of the Moho is actually only 3°, so that a normal 33 km crust beneath the Persian Gulf passes Northeastward into a maximum 49 km thickness where the edge of Arabia is underthrust (Figure 8). We interpret this as a result of a shortening of the Zagros basement by about 75 km over the last 1.6 m.y.

This strain is most intense on the NE margin where the crustal thickening and surface deformation are greatest. According to the fault-plane solutions the present mechanism is shallow underthrusting, so the Moho is moving NE more rapidly than down. A slip of 27 km (26 km NE and 7 km down) on the new boundary thrust would be consistent with the seismic and gravity data in the SW half of the Zagros.

This model has been derived under the assumption of plate tectonics, which provides the necessary limitations on the number of variable parameters. Of course, if continental lithosphere does not have the strength to deform in large coherent units, then any number of non-unique explanations can be attached to the available geologic, gravity, and seismicity data. We are supported in our assumption by the similarity of the Zagros structures over the great length of the range which have evolved to a common pattern despite probable initial variations in coastline shape and crustal thickness. The smooth downwarp of the Arabian

lithosphere over 150 to 400 km as it approaches the Mesopotamian Trough is additional evidence of lithospheric strength and the applicability of plate tectonic concepts.

This model implies two important conclusions about the continental-convergence process. First, that subduction may not occur at the old trench site as in our simple models and those of Dewey and Bird. Instead the crust begins to deform and thicken. Second, that the viscoelastic resistance to the bending of the thick lithosphere of continental shields may be sufficient to force the formation of a new fault at a shallower angle. As subduction begins along this new fault it will isolate the continental shelf block from further subduction and result in its preservation at the core of a future mountain range. Thus the Zagros Mountains may hold the key to the final reconciliation of the classical and plate-tectonic definitions of the geosyncline.

Conclusions

Theoretical models calculated in this paper strongly depend on input parameters which cannot be specified uniquely. For a reasonable set of parameters, it can be stated that during the subduction process there is insufficient time for radioactive heating or heat conduction through the bottom of the lithosphere to significantly affect crustal temperatures. These processes become important after subduction has stopped. Calculations show

that after 30 m.y. of quiescence a continental slab of 150 km length and 2.5 x 10^{-6} erg/gm-sec average radioactive heat production will be raised to high-grade metamorphic temperatures. After an additional 70 m.y. melting would develop in the base of the slab, leading to plutonism. The rate of this regional-metamorphic evolution is directly controlled by crustal radioactivity and surface erosion rates, so that there is wide variability possible in the timing and severity of the resulting orogeny. However, the rapidity of observed metamorphic events suggests an influx of heat from the mantle. Frictional heating could be an important mechanism in thermal regime of the shallow part of the subduction zone.

The highest temperature reached through frictional heating is controlled by the profile of shear stress versus depth and the square root of the plate convergence velocity. At a velocity of 1 cm/yr and a shear stress of 1 kb frictional heating is too weak to cause any major change in the low-temperature anomaly introduced by the slab. However, at 6 cm/yr with similar stresses a high-temperature zone is formed on top of the subducting crust, and temperatures may reach the solidus of granite. This will result in minor igneous activity, but is primarily important because it sets a limit on the frictional stress at each depth.

At 5 cm/yr, these stress limits have been found to fall below 1 kilobar at depths greater than 25 km. Stick-slip behavior passes into melting or creep strain below about 15 km depth.

Thus the seismicity of continental convergence zones is necessarily shallow except for events within the slab. At lower velocities the stresses required to produce melting are unreasonable.

The other important forces in continental convergence result from crustal buoyancy and resistance to the bending of the lithosphere. Both tend to force the angle of subduction to become more shallow with time. While the effect of buoyancy builds up gradually with the amount of crust subducted, the greater thickness of continental shield lithosphere changes the mechanism of plate bending as soon as the continents meet. Subduction on the old oceanic plane is strongly resisted, and the formation of shallower thrust faults is required.

This process is shown to be active in the Zagros Mts., where there is a very young continental convergence zone. There mountains are developing on a horizontal triangular prism of detached crust between the old oceanic subduction plane to the NE and a new shallower fault plane to the SW. Continental underthrusting is continuing at a different site from the continental suture line. The crust of the Zagros range, which is the old Arabian continental shelf, is being thickened by underthrusting in the first stage of the orogenic process.

ACKNOWLEDGEMENTS

We thank John Minear for his work in the original development of the temperature program. Seth Stein developed and assisted with programs used in tracing seismic rays. The National Iranian Oil Company courteously provided temperature data from eighteen of their oilfields. The Aeronautical Chart and Information Center of the U.S. Air Force provided a compilation of available gravity data.

This research was supported by the Advanced Research Projects Agency and monitored by the Air Force Office of Scientific Research under contract F44620-71-C-0049 and NATO Science Grant #568 with Massachusetts Institute of Technology and by Grant DEF 74-22338 from the National Science Foundation to Northwestern University.

REFERENCES

Akascheh, B., Mechanism of the earthquake of April 10, 1972 in Qir (Iran), Zeitschrift fur Geophysik, 39, 1055-1061, 1973.

Andrews, D.J., and N.H. Sleep, Numerical modelling of tectonic flow behind island arcs, Geophys. J. Roy. Astron. Soc., 38, 237-251, 1974.

Brown, G.C., and W.S. Fyfe, The production of granitic melts during ultrametamorphism, Contr. Mineral. Petrol., 28, 310-318, 1970.

Byerly, J.D., The frictional characteristics of Westerly granite, Ph.D. Thesis, Massachusetts Institute of Technology, Cambridge, Mass., 1966.

Carslaw, H.S., and J.C. Jaeger, Conduction of Heat in Solids, Clarendon Press, Oxford, pp. 62-75, 1959.

Chapple, W.M., Mechanics of thin-skinned fold and thrust belts, Trans. Am. Geophys. Union, 56, 457, 1975.

Clark, S.P., and A.E. Ringwood, Density distribution and constitution of the mantle, Rev. Geophys., 2, 35-88, 1964.

Clark, S.P., Jr., Thermal conductivity in Handbook of Physical Constants, Geol. Soc. Amer. Mem., 97, 459-482, 1966.

Coster, H.P., Terrestrial heat flow in Persia, Monthly Notices, Geophysical Supplement 5, R. astr. Soc., 131-145, 1947.

Dana, J.D., On some results of the earth's contraction including a discussion of the origin of mountains and the nature of the earth's interior, Amer. J. Sci., 5, No. 5, 423-443, 474-475; No. 6, 6-14, 104-115, 161-172, 304, 381-382, 1873.

Dewey, J.F., and J.M. Bird, Mountain belts and the new global tectonics, J. Geophys. Res., 75, 2625-2647, 1970.

Dewey, J.F., W.C. Pitman, III, W.B.F. Ryan, and J. Bonnin, Plate tectonics and the evolution of the Alpine system, Geol. Soc. Amer. Bull., 84, 3137-3180, 1973.

Emery, K.O., E. Uchupi, J.D. Phillips, C.O. Bowin, E.T. Bunce, and S.T. Knott, Continental rise off eastern North America, Amer. Assoc. Petrol. Geol. Bull., 54, 44-108, 1970.

Fitch, T.J., Earthquake mechanism in the Himalayan, Burmese, Andaman regions and continental tectonics in Central Asia, J. Geophys. Res., 75, 2699-2708, 1970.

Forsyth, D.W., Anisotropy and structural evolution of the oceanic upper mantle, Ph.D. Thesis, Massachusetts Institute of Technology and Woods Hole Oceanographic Institution, Cambridge, Mass., 1973.

Hall, James, On the formation of mountains, Canadian J., 5, 542-544, 1860.

Haynes, S.J., and H. McQuillan, Evolution of the Zagros suture zone, southern Iran, Geol. Soc. Amer. Bull., 85, 739-744, 1974.

Julian, B., Ray tracing in arbitrarily heterogeneous media, Technical Note 1970-45, Lincoln Laboratory, Massachusetts Institute of Technology, Lexington, Mass., 1970.

Knopoff, L. and A.A. Fouda, Upper-mantle structure under the Arabian Peninsula, Tectonophysics, 26, 121-134, 1975.

Kohlstedt, D.L., C. Goetze, and W.B. Durham, Experimental deformation of single crystal olivine with application to flow in the mantle, preprint, 1975.

LePichon, X.L., Sea-floor spreading and continental drift, J. Geophys. Res., 73, 3661-3697, 1968.

MacDonald, G., Calculations on the thermal history of the earth, J. Geophys. Res., 64, 1967-2000, 1959.

Minear, J.W., and M.N. Toksöz, Thermal regime of a downgoing slab and new global tectonics, J. Geophys. Res., 75, 1397-1419, 1970a.

Minear, J.W. and M.N. Toksöz, Thermal regime of a downgoing slab, Tectonophysics, 10, 367-390, 1970b.

Minear, J.W., and M.N. Toksöz, Reply, J. Geophys. Res., 76, 610-612, 1971.

Naylor, R.S., Acadian orogeny: an abrupt and brief event, Science, 172, 558-559, 1971.

Nowroozi, A.A., Seismo-tectonics of the Persian Plateau, Eastern Turkey, Caucasus, and Hindu-kush regions, Bull. Seismo. Soc. Amer., 61, 317-341, 1971.

Nowroozi, A.A., Focal mechanism of earthquakes in Persia, Turkey, West Pakistan, and Afghanistan and plate tectonics of the Middle East, Bull. Seismo. Soc. Amer., 62, 823-850, 1972.

Oxburgh, E.R., and D.L. Turcotte, Thermal gradients and regional metamorphism in overthrust terrains with special reference to the Eastern Alps, Schweiz. Min. Petr. Mitt., 54, 641-662, 1974.

Phillips, J.D., Magnetic anomalies in the Red Sea, Phil. Trans. Roy. Soc. Lon., 267, 205-217, 1970.

Pitman, W.C., and M. Talwani, Sea-floor spreading in the North Atlantic, Geol. Soc. Amer. Bull., 83, 619-646, 1972.

Quereshy, M.N., S. Venkatachalam, and C. Subrahmanyam, Vertical tectonics in the Middle Himalayas: an appraisal from recent gravity data, Geol. Soc. Amer. Bull., 85, 921-926, 1974.

Skinner, B.J., Thermal expansion, in Handbook of Physical Constants, Geol. Soc. Amer. Mem., 97, 75-96, 1966.

Sleep, N.H., Teleseismic P-wave transmission through slabs, Bull. Seismol. Soc. Amer., 63, 1349-1373, 1973.

Sleep, N.H., Stress and flow beneath island arcs, Geophys. J. Roy. astr. Soc., 43, in press, 1975.

Smith, A.T., and M.N. Toksöz, Stress distribution beneath island arcs, Geophys. J. Roy. astr. Soc., 29, 289-318, 1972.

Smith, A.T., Time-dependent strain accumulation and release at island arcs, EOS Trans. AGU, 55, 427, 1974.

Stöcklin, J., Review of Iranian tectonics, Bull. Amer. Assoc. Petrol. Geol., 52, 1229-1258, 1968.

Stöcklin, J., and M.H. Navabi, Tectonic map of Iran, Geological Survey of Iran, Tehran, 1973.

Toksöz, M.N., M.A. Chinnery, and D.L. Anderson, Inhomogeneities in the earth's mantle, Geophys. J. Roy. astr. Soc., 13, 31-59, 1967.

Toksöz, M.N., J.W. Minear, and B. Julian, Temperature field and geophysical effects of a downgoing slab, J. Geophys. Res., 76, 1113-1138, 1971.

Toksöz, M.N., N.H. Sleep, and A.T. Smith, Evolution of the downgoing lithosphere and the mechanisms of deep focus earthquakes, Geophys. J. Roy. astr. Soc., 35, 285-310, 1973.

Tuttle, O.F., and N.L. Bowen, Origin of granite in the light of experimental studies in the system $NaAlSi_3O_8$ - $KAlSi_3O_8$-SiO_2-H_2O, Geol. Soc. Amer. Mem. 74, 1958.

Turcotte, D.L., and E.R. Oxburgh, A fluid theory for the deep structure of dip-slip fault zones, Phys. Earth Planet. Int., 1, 381-386, 1969.

Walcott, R.I., Isostatic response to crustal loading in Canada, Can. J. Earth Sci., 1, 716-727, 1970a.

Walcott, R.I., Flexural rigidity, thickness, and viscosity of the lithosphere, J. Geophys. Res., 75, 3941-3954, 1970b.

Watts, A.B., and M. Talwani, Gravity anomalies seaward of deep-sea trenches and their tectonic implications, Geophys. J. Roy. astr. Soc., 36, 57-90, 1974.

Wells, A.J., The Zagros crush zone and its tectonic implications, Geol. Mag., 106, 385-394, 1969.

Wilcox, L.E., W.J. Rothermel, J.T. Voss, A geophysical geoid of Eurasia, Trans. Am. Geophys. Union, 53, 343, 1972.

Table 1

THERMAL MODEL INPUT PARAMETERS

Figure #	Velocity, cm/year	Dip, degrees	Time since collision, m.y.	Opacity,[1] cm^{-1}	Crustal[2] Radioactive H erg/g-sec	Fault Shear Stress, kb
2	1	30	8.0	50	U 3.9×10^{-6} L 1.1×10^{-6}	1.0
3	6	15	2.8	50	U 3.9×10^{-6} L 1.1×10^{-6}	1.0-1.5
4A	Stationary	15	32.8	50	U 3.9×10^{-6} L 1.1×10^{-6}	0.
4B	Stationary	15	102.8	50	U 3.9×10^{-6} L 1.1×10^{-6}	0.
8	2.7/2.6	30/15	1.	130	U 2.6×10^{-6} L 7.5×10^{-7}	0.4 x P and ≤ 4

(1) McDonald (1959)

(2) U indicates upper and L the lower half of the crust.
First four models have values from Clark and Ringwood (1964).

Figure Captions

Figure 1. Three stages in the evolution of a hypothetical continental convergence zone: A) Subduction of the intervening oceanic plate. An Atlantic-type margin approaches a Pacific-type trench with andesitic volcanism produced by underthrusting. B) Subduction of continental rise sediments and then crust of the continental shelf, perhaps with granite magma produced by frictional heat. C) Formation of a new thrust within continental crust and subduction beneath the continental shelf with further granite formation.

Figure 2. Temperature, heat flow, and Bouguer gravity sections after subduction of continental crust for 8 m.y. at 30° dip and 1 cm/yr. Mafic portion of the lithosphere below the Moho is shaded. Frictional stress on the fault is 1 kb.

Figure 3. Temperature, heat flow, and Bouguer gravity sections after subduction of continental crust for 2.9 m.y at 15° dip and 6 cm/yr. Frictional stress decreases from 1.5 kb at 10 km depth to 1 kb at 80 km.

Figure 4. Evolution of a convergence zone without motion: A) Temperature and heat flow section evolved from Figure 3 after 30 m.y. Dashed lines show former outlines of the slab. B) Temperature and heat flow section evolved from 4A after 70 m.y. additional time. Hatched area is partially melted and a source of granite magma.

Figure 5. Two different solidus curves (center), for granite saturated with water and dry granite with muscovite. Temperatures on fault surface (bottom) with subduction at 30° dip and 5 or 1 cm/yr and no friction. Stresses at each depth (top) necessary to raise these temperatures to either solidus. Near surface, stress is limited by pressure and the coefficient of friction.

Figure 6. Outline map of the Zagros after Stöcklin and Nabavi (1973): 1. Zagros Crush Zone and NE limit of deformation; 2. SW limit of deformation; 3. Recent volcanoes; 4. Earthquake epicenters 1950-1965 after Nowroozi (1971); 5. Tertiary volcanic rocks, mainly andesite; 6. Persian Gulf and various seas (inset).

Figure 7. Gouguer gravity anomaly in the Zagros region after U.S.A.F. "Bouguer gravity anomaly map of Asia" (Wilcox et al., 1972). Contour interval 50 milligalls.

Figure 8. Preferred model of present Zagros temperatures (top) and tectonics (bottom). Computation of thermal model described in text. Diagram shows major Recent thrust, minor thrusts under surface folding, subducted continental rise sediments (dashed), and thickening of the lithosphere toward the Arabian shield.

Figure 9. Projection of earthquakes relocated by Nowroozi (1971) onto plane of Figure 8 with same distance scale. Principal stresses by nodal-plane solutions of Nowroozi (1972) and

Akascheh (1973). Dashed lines show inferred planes of oceanic (left) and continental (right) subduction.

Figure 10. Heat flow curve from model of Figure 8 compared with one heat flow determination (large dot) and heat flow estimates from oil-well temperatures (small dots). At bottom, total Bouguer gravity anomaly of the model is subdivided into constituent parts and compared with one-degree averages projected onto the cross-section (dots).

Figure 11A. Anomalous delay in seconds of P waves from an event at 20 km depth on the fault in Figure 2. Delays are plotted according to ray azimuth and incidence angle at a depth of 150 km.

11B. Travel-time residuals of less than 3 sec magnitude recorded at Shiraz (Figure 8) during 1/68-4/69 according to the Bulletin of the I.S.C. Average residual value of -0.5 sec has been removed. Dashed line shows the strike of the range.

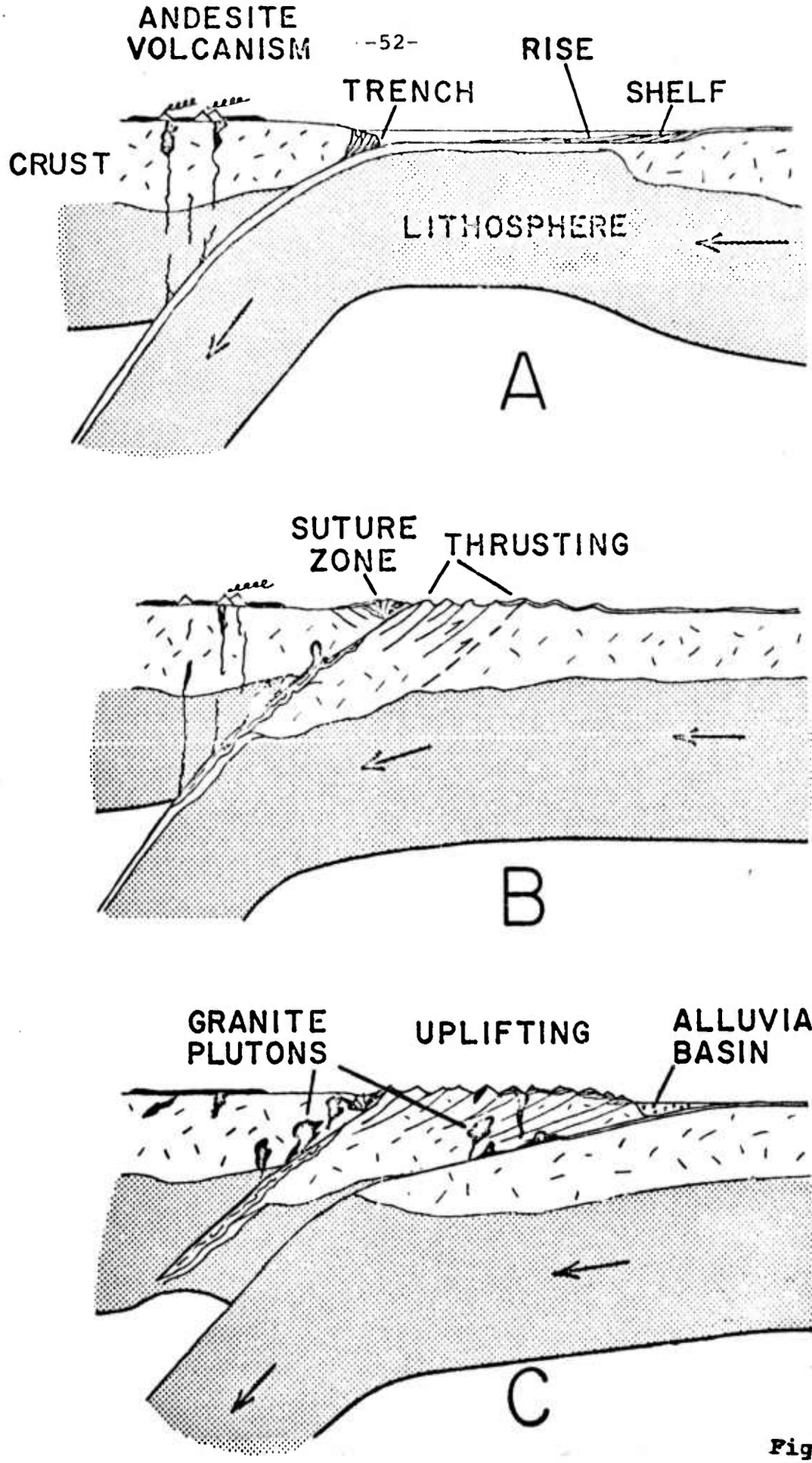
ANDESITE VOLCANISM
TRENCH
RISE
SHELF
CRUST
LITHOSPHERE
A
SUTURE ZONE
THRUSTING
B
GRANITE PLUTONS
UPLIFTING
ALLUVIAL BASIN
C

Fig. 1

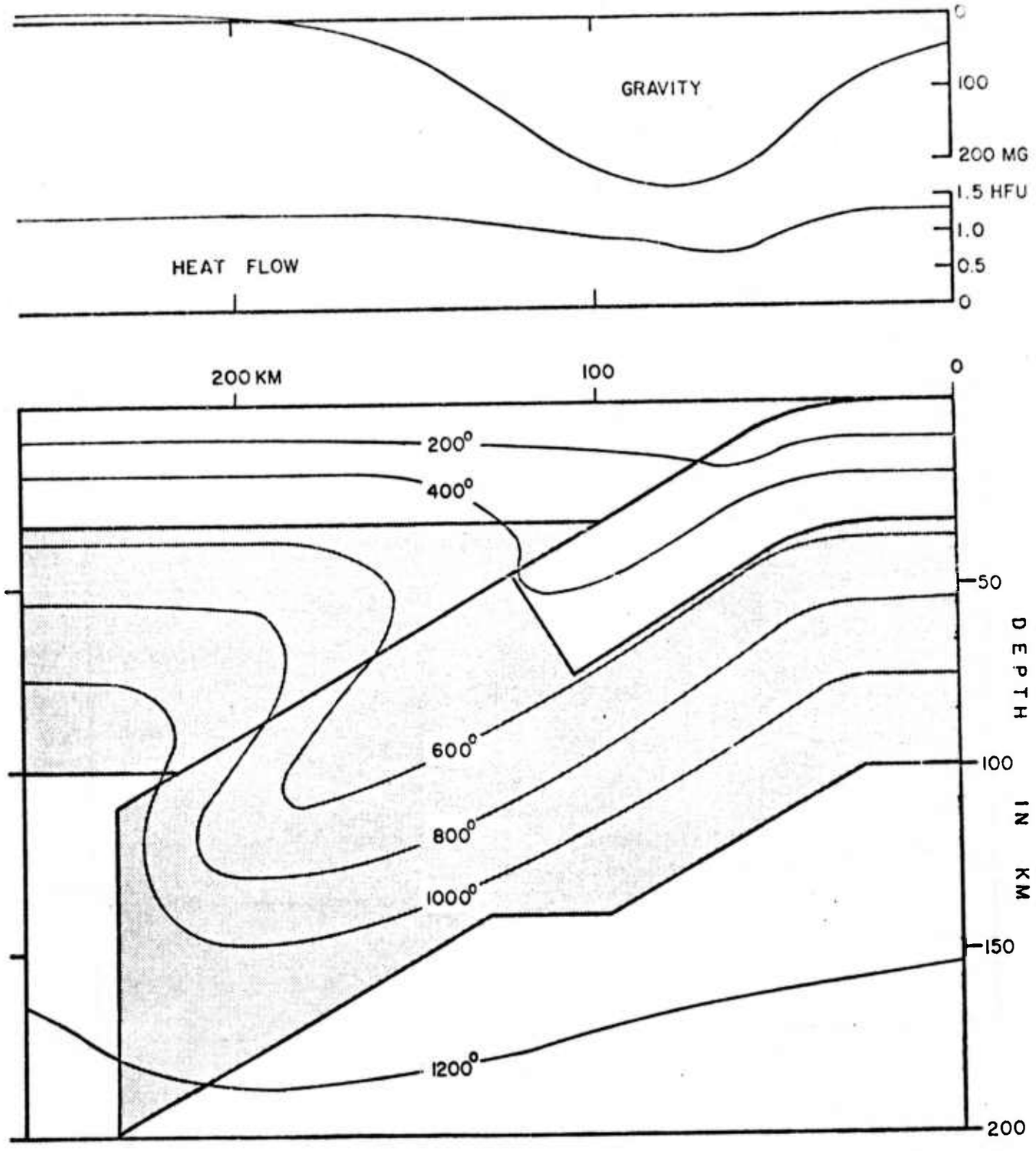
GRAVITY
0
100
200 MG
HEAT FLOW
1.5 HFU
1.0
0.5
0
200 KM
100
0
200°
400°
600°
800°
1000°
1200°
50
100
150
200
DEPTH IN KM

Fig. 2

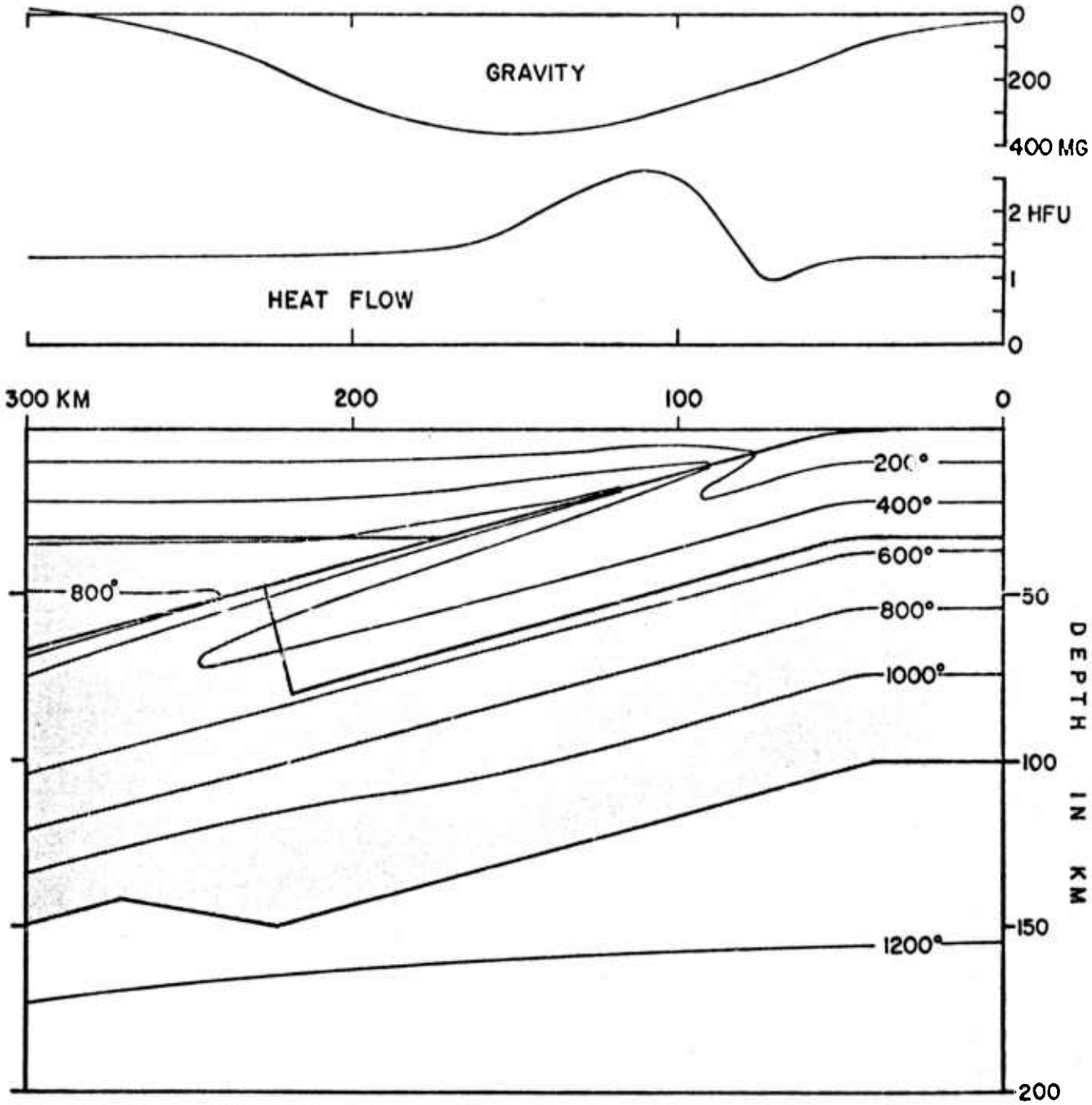
GRAVITY
0
200
400 MG
2 HFU
1
0
HEAT FLOW
300 KM
200
100
0
200°
400°
600°
800°
1000°
1200°
800°
50
100
150
200
DEPTH IN KM

Fig. 3

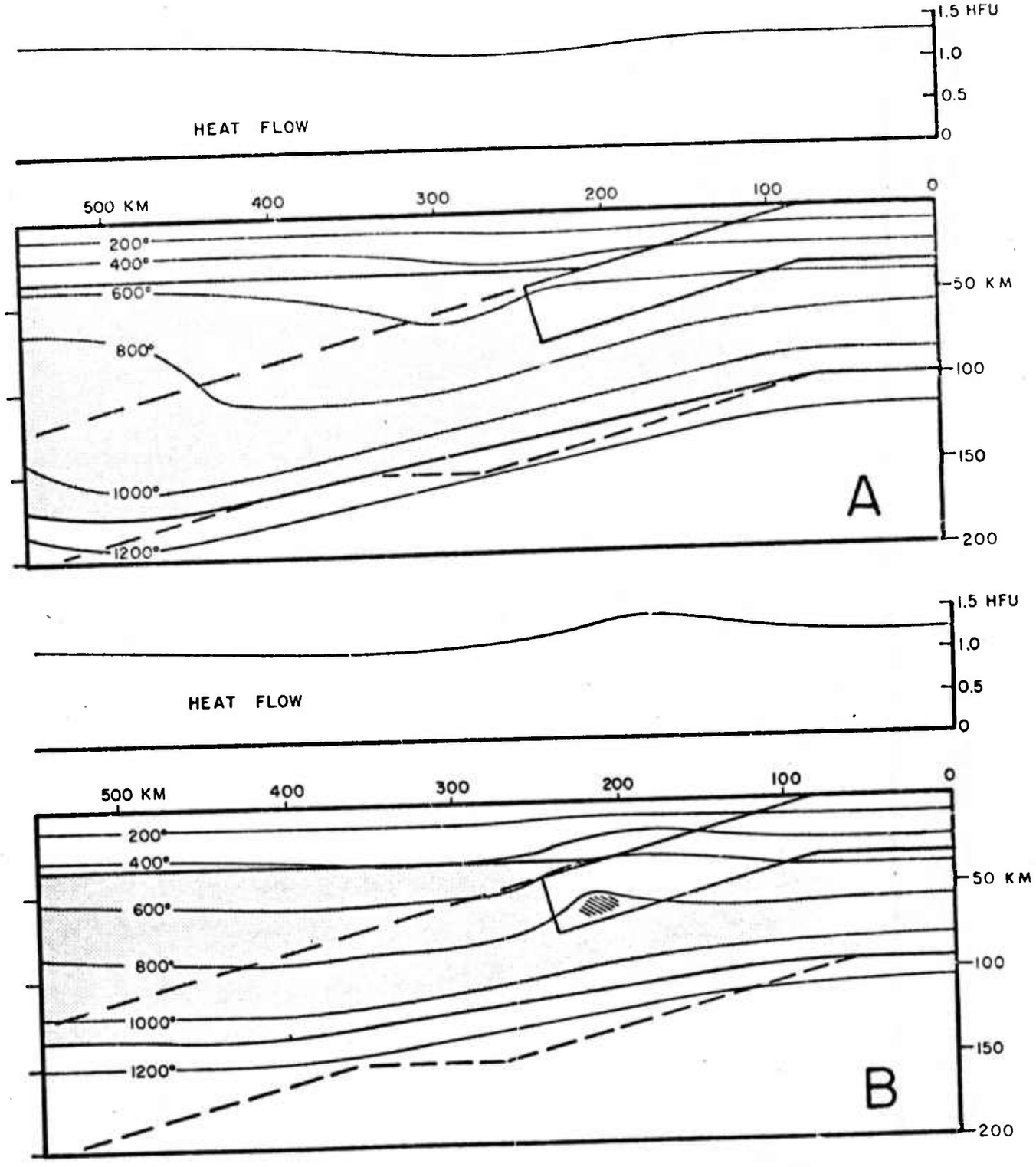
1.5 HFU
1.0
0.5
0
HEAT FLOW
500 KM
400
300
200
100
0
200°
400°
600°
800°
1000°
1200°
50 KM
100
150
200
A
1.5 HFU
1.0
0.5
0
HEAT FLOW
500 KM
400
300
200
100
0
200°
400°
600°
800°
1000°
1200°
50 KM
100
150
200
B

Fig. 4

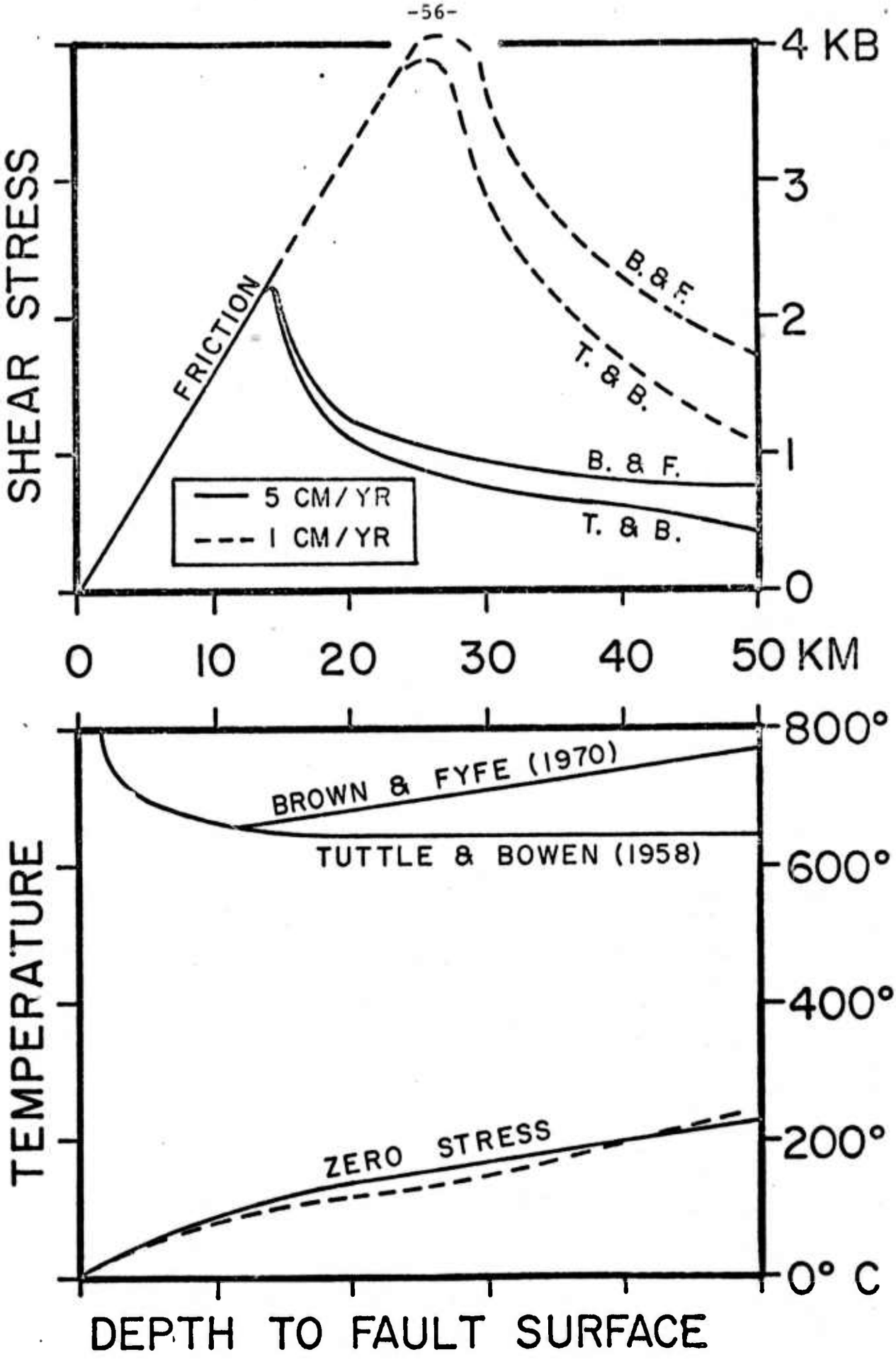
SHEAR STRESS
4 KB
3
2
1
0
FRICTION
B. & F.
T. & B.
B. & F.
T. & B.
5 CM/YR
1 CM/YR
0
10
20
30
40
50 KM
TEMPERATURE
800°
600°
400°
200°
0° C
BROWN & FYFE (1970)
TUTTLE & BOWEN (1958)
ZERO STRESS
DEPTH TO FAULT SURFACE

Fig. 5

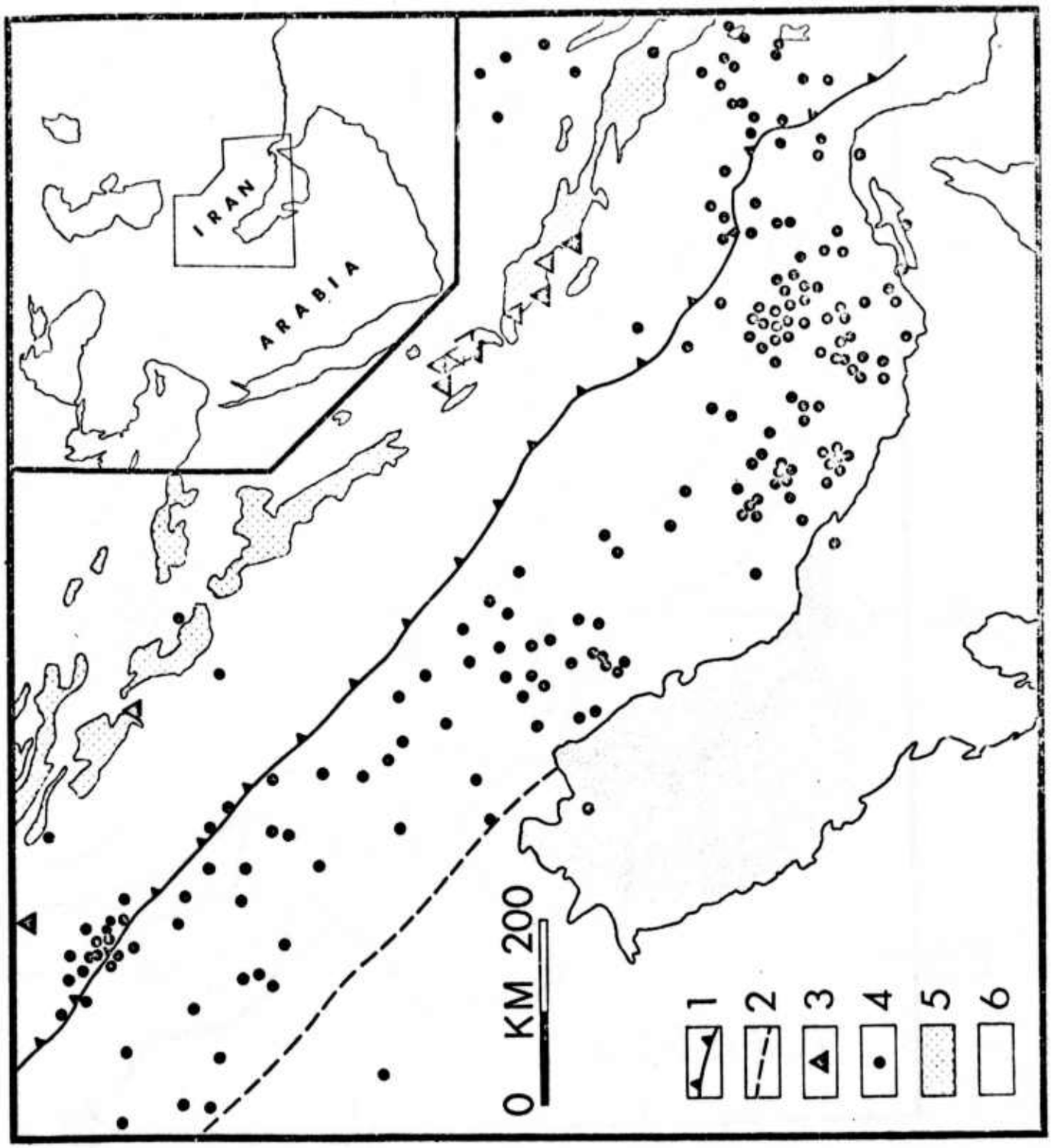

Fig. 6

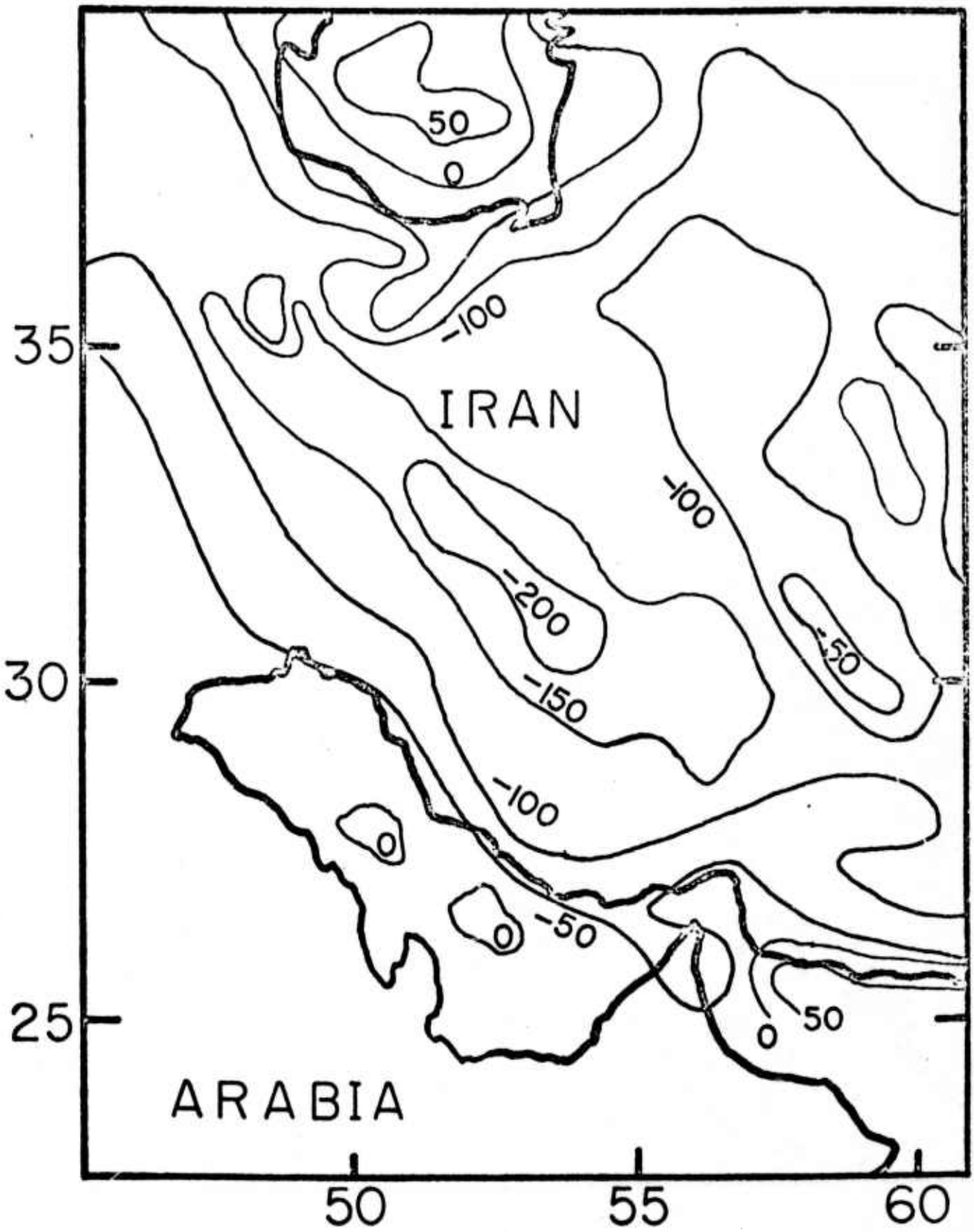

Fig. 7

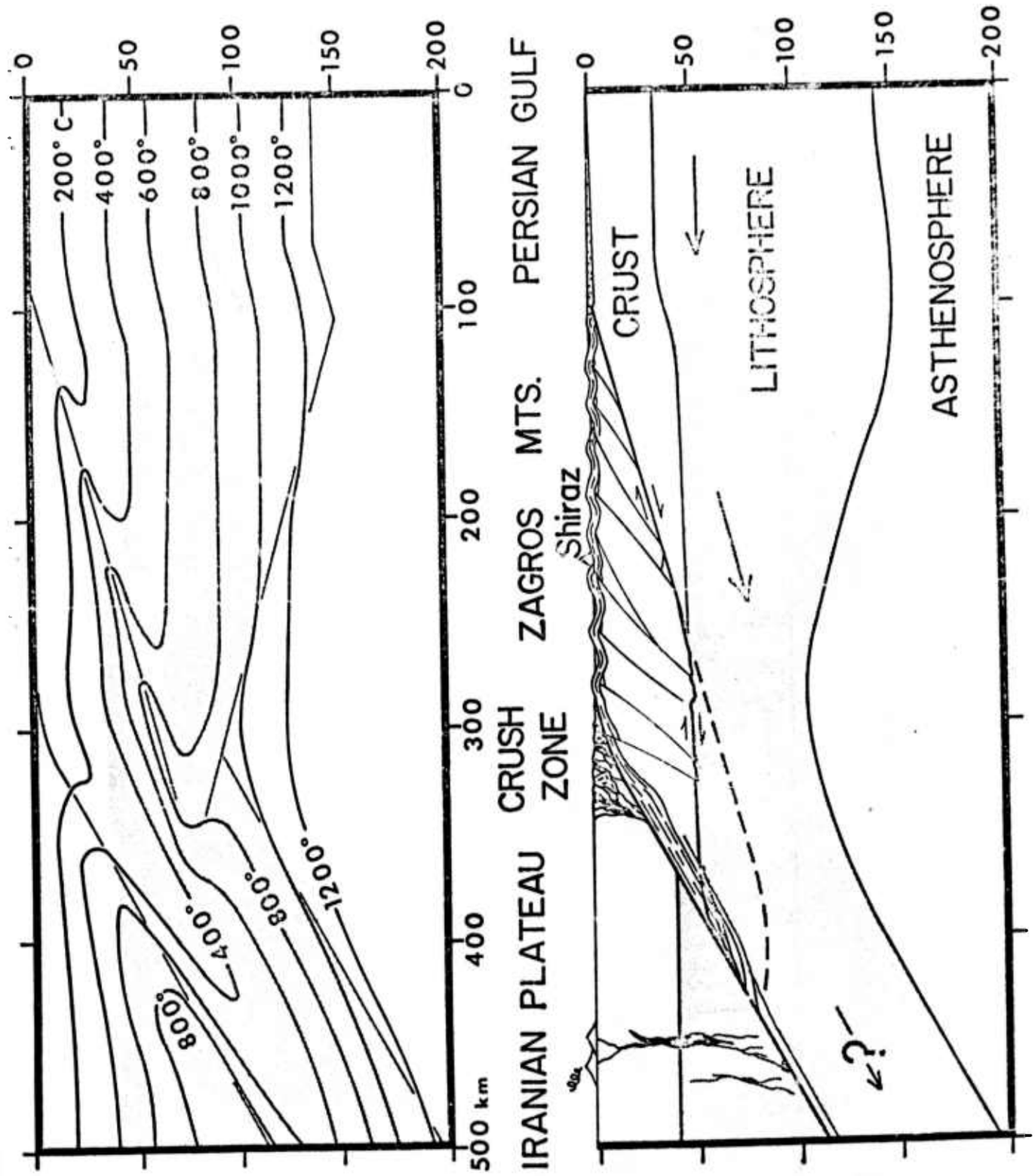
0
50
100
150
200
200° C
400°
600°
800°
1000°
1200°
0
100
200
300
400
500 km
IRANIAN PLATEAU
CRUSH ZONE
ZAGROS MTS.
Shiraz
PERSIAN GULF
CRUST
LITHOSPHERE
ASTHENOSPHERE
?

Fig. 8

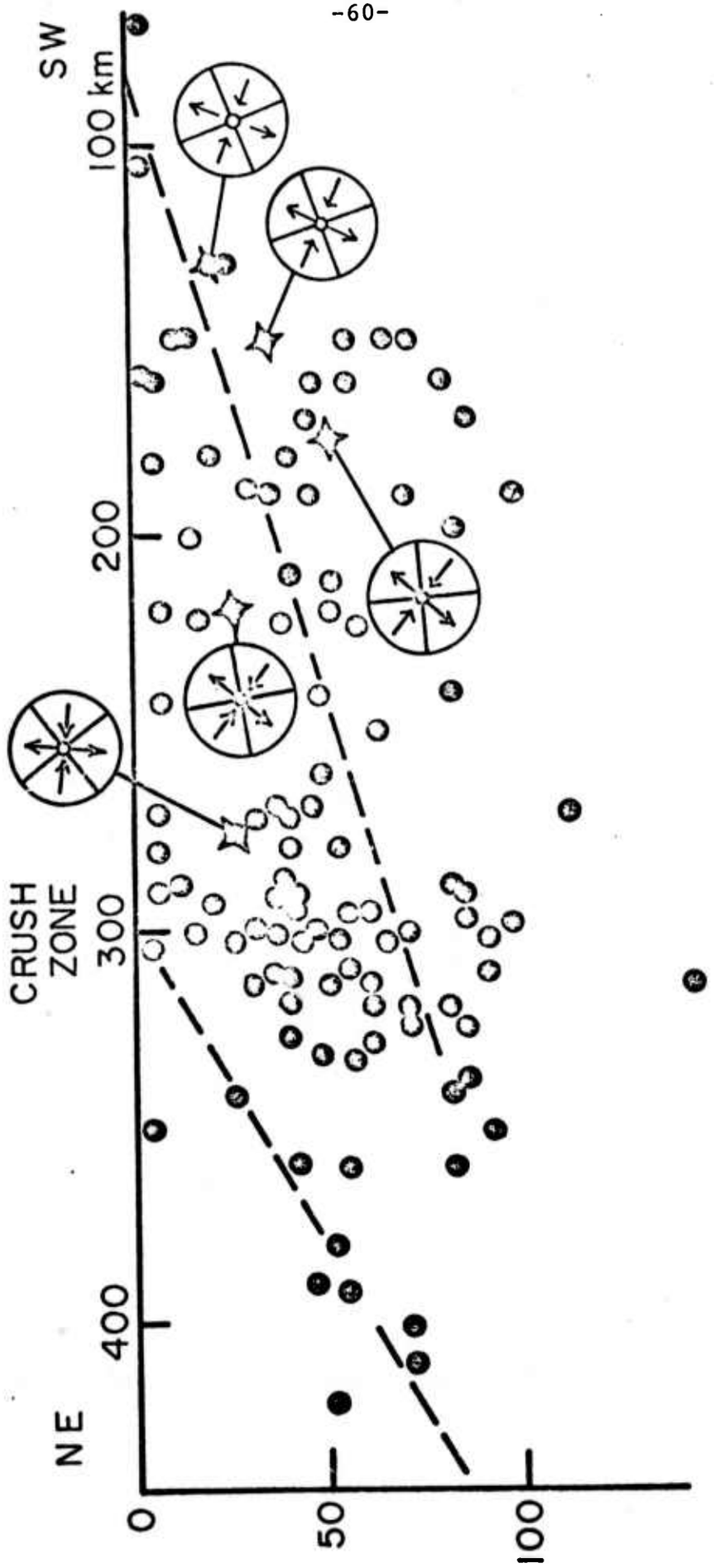

Fig. 9

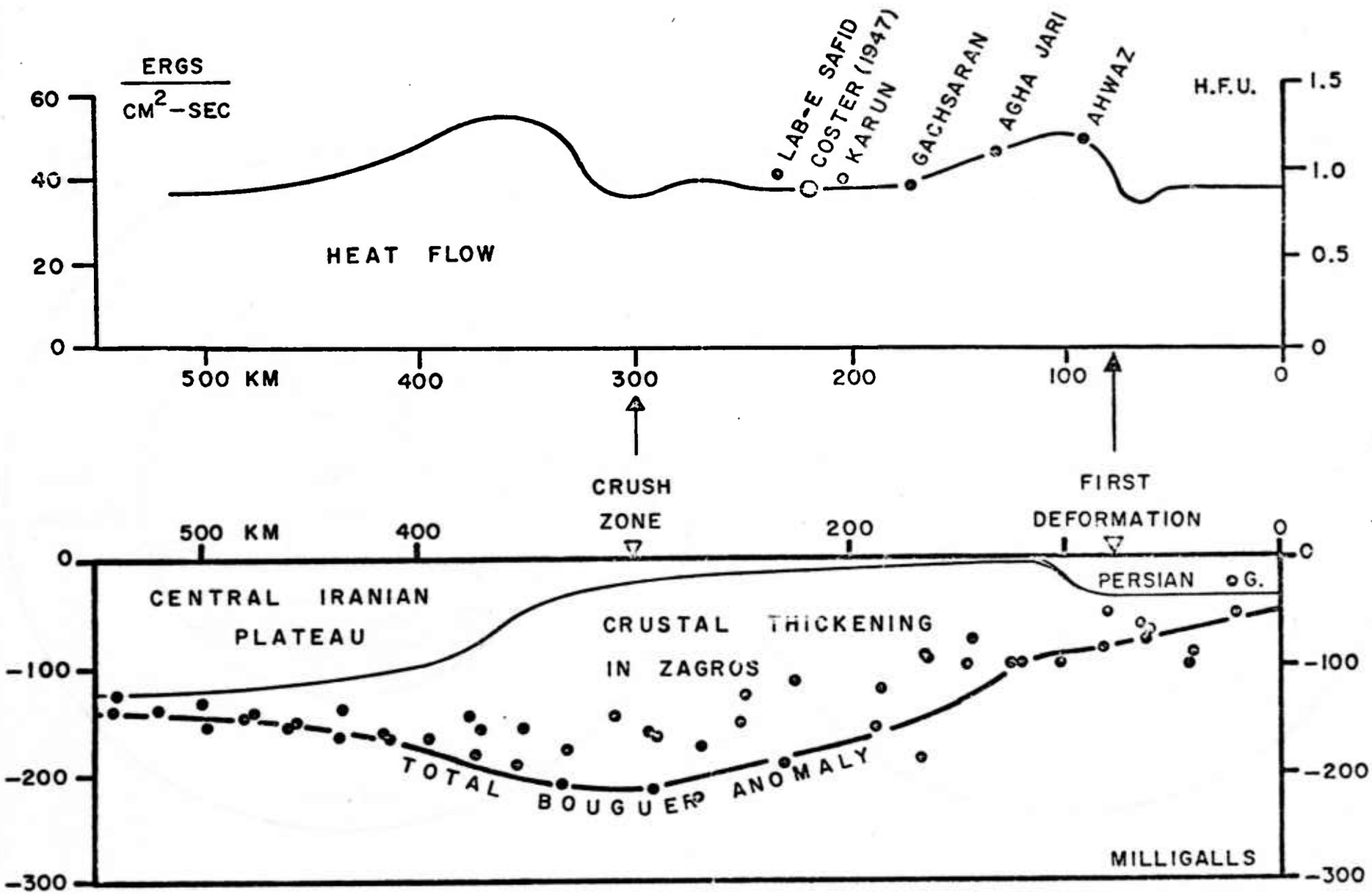
ERGS
CM²-SEC
60
40
20
0
HEAT FLOW
LAB-E SAFID
COSTER (1947)
KARUN
GACHSARAN
AGHA JARI
AHWAZ
H.F.U.
1.5
1.0
0.5
0
500 KM
400
300
200
100
0
CRUSH ZONE
FIRST DEFORMATION
CENTRAL IRANIAN PLATEAU
CRUSTAL THICKENING IN ZAGROS
PERSIAN G.
TOTAL BOUGUER ANOMALY
MILLIGALLS
-100
-200
-300

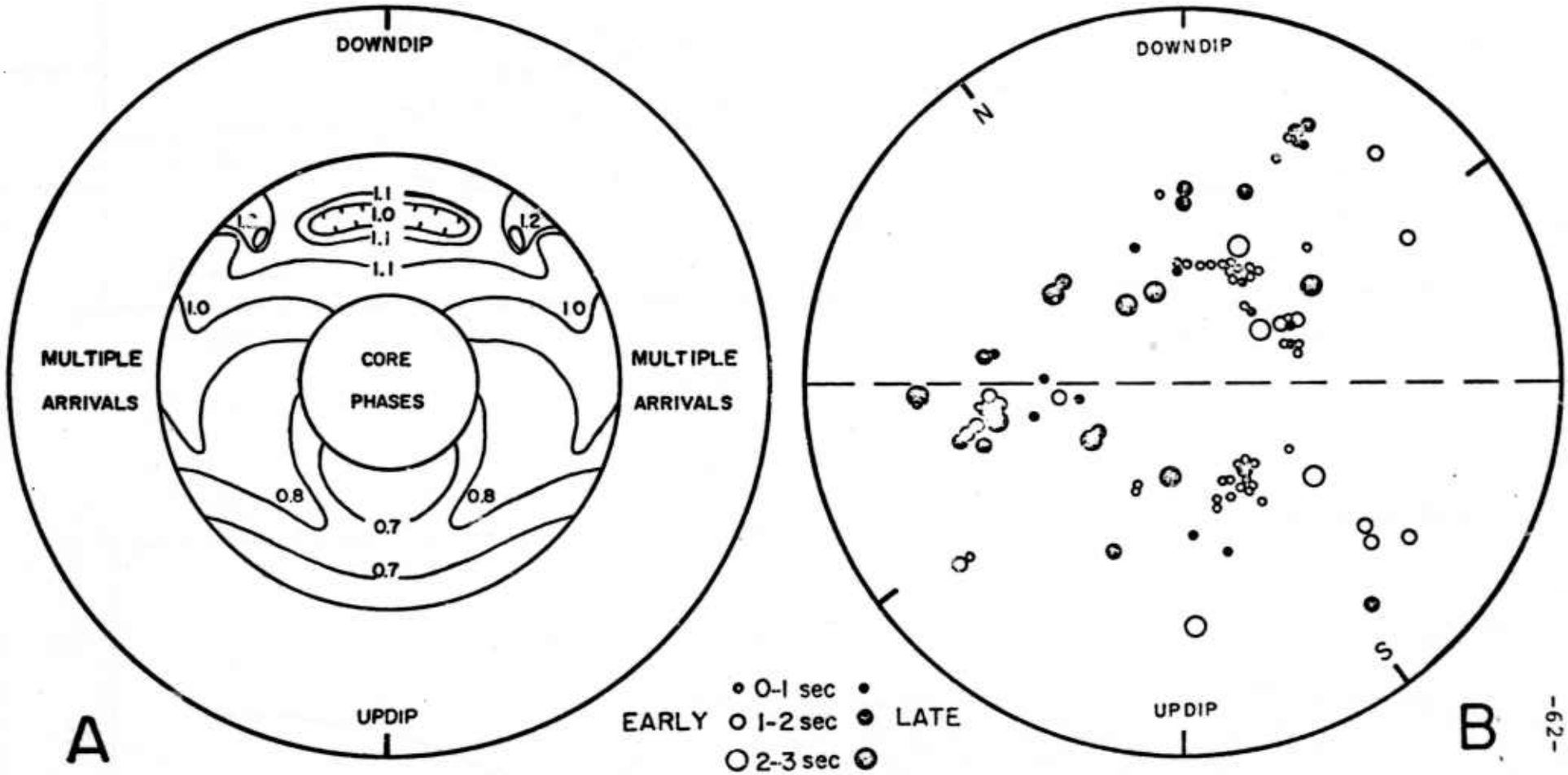
DOWNDIP
1.1
1.0
1.1
1.2
1.1
1.0
1.0
MULTIPLE
ARRIVALS
CORE
PHASES
MULTIPLE
ARRIVALS
0.8
0.8
0.7
0.7
UPDIP
A
EARLY
0-1 sec
1-2 sec
2-3 sec
LATE
DOWNDIP
N
S
UPDIP
B

Fig. 11

3.4 North American-Eurasian Plate Boundary in Northeast Asia

by M.E. Chapman and S.C. Solomon

ABSTRACT

The intracontinental portion of the boundary between the North American and Eurasian plates can be identified on the basis of seismicity, recent tectonics and earthquake focal mechanisms. The simplest plate geometry that can explain these data involves a North American-Eurasian boundary that extends from the Nansen ridge through a broad zone of deformation in northeast Asia to the Sea of Okhotsk and thence southward through Sakhalin and Hokkaido to a triple junction in the Kuril-Japan trench. Such a configuration can account quantitatively for the slip vectors derived from earthquake mechanisms in Sakhalin and Hokkaido. On the basis of new slip vector data, the North American-Eurasian angular velocity vector is revised only slightly from previous determinations. The intracontinental plate boundary is diffuse and may be controlled by ancient plate sutures. Deformation within about 10° of the rotation pole, which lies very near the boundary, cannot be modeled by rigid plate tectonics. These characteristics of intracontinental plate boundaries are related to the greater thickness and heterogeneity of continental lithosphere and to the influence of continents on the plate tectonic driving forces.

INTRODUCTION

The theory of plate tectonics is based on the idea that the earth's surface may be subdivided into a small number of rigid plates (Morgan, 1968; Le Pichon, 1968). In oceanic areas, the boundaries between major plates are readily defined by the distribution of earthquakes and characteristic bathymetric features and are typically no more than a few kilometers in width. Where plate boundaries bisect continental masses, however, the place where one plate ends and another begins is generally much more difficult to locate with confidence. The problem of identifying a plate boundary within a continent is heightened when the relative velocity of the two plates is small.

In this paper, we examine in detail several aspects of one such intracontinental plate boundary: the boundary in northeast Asia between the Eurasian and the North American plates. There are several reasons for such a study. If the concept of distinct plates is valid, then each plate must be encircled by some closed curve on the earth's surface. Complete specification of the boundary of each plate is formally necessary to conduct certain tests of driving force models for plate tectonics (Solomon and Sleep, 1974; Forsyth and Uyeda, 1975; Solomon et al., 1975). More interesting are the underlying causes for the diffuse, rather ill-defined nature of intracontinental plate boundaries, including the possibilities that continental lithosphere is thicker, more difficult to push or pull across the earth's surface, and more heterogeneous than oceanic lithosphere.

We begin with a review of historical seismicity and recent tectonic activity in northeast Asia. An evaluation of several possible plate configurations to explain these data is then made. The simplest explanation compatible with seismic and tectonic evidence is that the present North American-Eurasian

plate boundary extends from the Nansen ridge in the Arctic ocean through a broad, tectonically active belt in northeast U.S.S.R. (Demenitskaya and Karasik, 1969; Grachev et al., 1970; Churkin, 1972) to the Sea of Okhotsk, and thence southward through Sakhalin and Hokkaido to a triple junction at the Japan-Kurile trench. Earthquake source mechanisms are consistent with this view except in the immediate vicinity of the relative rotation pole for the two plates. Finally, some thoughts are offered on the factors affecting the location and nature of intracontinental plate boundaries.

SEISMICITY

The boundaries between plates are seismically active. Seismicity is the primary basis for identifying the North American-Eurasian plate boundary in the Atlantic and Arctic Oceans as the mid-Atlantic and Nansen ridge systems, respectively. The correctness of such an identification is apparent by inspection from a global seismicity map based on only a few years of data, such as that in Figure 1. How the plate boundary continues from the Arctic ocean onto the Eurasian continent is by no means clear from the figure, however.

As an aid in better defining this plate boundary in northeast Asia, we have plotted in Figure 2 the epicenters of all instrumentally located shallow seismic events in the region for the period 1909-1973. The original epicenters were obtained from a number of earthquake data sources (Linden, 1961; Savarensky et al., 1962; Hodgson et al., 1965; Sykes, 1965; Solov'yev, 1965; Int. Seismol. Cent., 1966-1973; Nat. Ocean. Atmos. Admin., 1970-1973; Int. Geod. Geophys. Union, 1918-1963; Academy of Sciences USSR, 1963-1970). Where possible, the events prior to 1952 were relocated using modern travel time tables (Herrin, 1968) to obtain more accurate locations. Observed P-wave and S-wave arrival times are from the bulletin of the Int. Geod. Geophys. Union (1918-1951); the P-wave and S-wave

travel time uncertainties were assumed to be 1.5 and 3.0 seconds, respectively. The relocated events are listed in Table 1.

Several conclusions may be drawn from these seismicity maps. In oceanic regions, the plate boundary defined by the seismic belt is very narrow, possibly as little as 10 km in width (Figure 1). However, at the Eurasian continental margin, the seismic belt widens to 300 km (Figure 2). A broad seismic zone extends from the Laptev sea across northeast U.S.S.R. to the northern Sea of Okhotsk. The zone is 600 km wide at its maximum width, and includes both large and small earthquakes throughout its entire extent.

This broad seismically active band appears to terminate abruptly at the Sea of Okhotsk. The apparent aseismicity of the Sea of Okhotsk may be an artifact of a sparse instrumental network or may possibly be real. Until 1968 there were few seismometers in the region; the nearest stations were Magadan (59° 33'N, 150° 48'E), Okha (53° 33'N, 142° 56'E), and Yakutsk (62° 01'N, 129° 43'E). A major earthquake in the region, with body wave magnitude 5 1/4, occurred on May 10, 1947 at 57.9°N, 141.9°E. Prior to 1968 there were no small events recorded in this area. However, after five new seismic stations were installed in Yakutia in 1968, small events were detected in the Sea of Okhotsk close to the stations (Academy of Sciences USSR, 1968). Because of this increase in reported events and the one major event, it is likely that the Sea of Okhotsk region is seismically active, even though earthquakes with magnitudes greater than 4 are rare.

Another feature of Figure 2 is a zone of small magnitude earthquakes from 120° to approximately 135°E longitude at about 56°N latitude. This zone is an extension of the Lake Baikal seismic belt (Gutenberg and Richter, 1949). It is

not clear from the seismicity whether this zone continues eastward to the seismically active portions of the Sea of Okhotsk.

There are many shallow events on Sakhalin, an area known for its relatively high seismicity (Solov'yev, 1965). The north-trending seismic belt on Sakhalin is about 300 km wide, and appears to continue through Hokkaido to the Japan-Kurile trench.

There are numerous earthquakes located in the Kuril and Aleutian trenches, and many small, shallow events extend inland on Kamchatka. Also on Kamchatka there appears to be a short seismic belt extending northwards from the Komandorski islands. This belt is probably related to underthrusting of the Pacific plate (Cormier, 1975).

RECENT TECTONICS

A brief review of field geological and geophysical evidence for recent tectonic activity in the Sea of Okhotsk region is a necessary preliminary to the discussion of possible plate boundaries in the area and to the interpretation of earthquake focal mechanisms.

The principal Cenozoic tectonic features of central and southern Kamchatka are illustrated in Figure 3 (Alverson et al., 1967). Most faults in Kamchatka are parallel to the Kuril trench, and where presently active are likely related to subduction of the Pacific plate rather than the plate boundary in question. The only major fault system that trends in an east-west direction is the Kronoki-Krutogorova fault zone (Suprenko and Dekin, 1968; Suprenko et al., 1973). In the Kronoki peninsula the faults in this zone are right lateral, with

a maximum horizontal offset of 20-25 km. In the western portion of the Kronoki-Krutogorova fault zone the sense of motion is left-lateral, opposite to the sense of motion in eastern Kamchatka. These western faults have offsets similar in amplitude to those of the faults in the Kronoki peninsula. The fault zone may form the southern boundary of a rift system, active in Plio-Pleistocene times, in the central Kamchatka basin (Suprenko et al., 1973).

Sakhalin is dominated structurally by compressive features such as faults and folds that trend north-south along the longitudinal axis of the island. One of the primary faults is the central Sakhalin fault, a thrust fault with a meridional trend and a westerly dip of approximately 70°. The strike of drag folds and second order faults indicates some right-lateral movement along the main fault. This fault is dated as being active in the Late Miocene and Pliocene, and is still active today (Zanyukov, 1971). Quaternary displacements have been measured and the epicenters of crustal earthquakes are located in the fault zone.

In the Schmidt peninsula (northern tip of Sakhalin) there are also north to northwest trending thrust faults which exhibit some right-lateral motion. The sense of horizontal displacement is indicated by the inclination of slickensides, displaced features and drag folds. There is up to 14 km of right-lateral offset. The main tectonic activity was in Plio-Pleistocene time. However, the presence of tectonic scarps, rockfalls and slides, and the reworking of stream drainage patterns indicate that the movements are continuing today (Rozhdestvenskiy, 1973).

That compressive forces have acted upon Sakhalin is also indicated by folding. The axes of anticlines and synclines trend north-south in Sakhalin

parallel to the strike of the thrust faults (Pushcharovskiy, 1965; Gal'tsev-Bezyuk, 1968). During the latest episode of folding, denoted the Sakhalin Orogeny, Pliocene deposits were folded. This episode of folding has continued until the present. Geodetic measurements indicate that vertical crustal movements of 3 to 9 mm/year are occuring in southern Sakhalin (Zakharov and Yakushko, 1972).

SOME POSSIBLE PLATE CONFIGURATIONS

There are a number of ways northeast Asia may be subdivided into plates consistent with the seismicity and recent tectonic activity discussed above. All of these plate descriptions are to some extent inadequate for they fail to account fully for intraplate deformation and the finite width of intracontinental plate boundaries. Nonetheless, we prefer one such description that is at the same time simple, in approximate agreement with the evidence outlined in preceding sections, and useful for making quantitative predictions.

The primary test of a proposed plate model is whether the sense of motion at plate boundaries predicted by the relative angular velocity vector of the adjacent plates is consistent with seismic and tectonic evidence. To make this test we need reasonably accurate estimates of the Eurasian-North American rotation pole and rate. A number of determinations of these quantities have been made by a variety of techniques; these are summarized in Table 2. Probably any of the three most recently published solutions are suitable for the purposes of this section. In a later section we derive a new Eurasian-North American angular velocity vector based on our preferred plate boundary description and new earthquake fault plane solutions.

In addition to the Eurasian, North American, and Pacific plates, several smaller plates have from time to time been proposed.

The possible existence of a China plate has been discussed by several authors (Morgan, 1968, 1972; Molnar et al., 1973; Das and Filson, 1974). The primary evidence used to support a separate China plate is the Baikal rift. Das and Filson (1974) postulate a (west) China plate rotating clockwise with respect to Eurasia about a pole near the southern tip of Lake Baikal. This would account for active extension in the Baikal rift, and some of the other earthquake source mechanisms in Asia. Morgan (1972) gives a counterclockwise China-Eurasian rotation rate of 2.4×10^{-7} deg/year about 50°N, 127°E. Molnar et al. (1973) discount the utility of the China plate concept for describing Asian tectonics. The rift zone has "spread" no more than a few tens of kilometers since the beginning of the Pliocene (Florensov, 1969). This corresponds to an average half-spreading rate of one to two orders of magnitude smaller than extension at a typical mid-ocean ridge. Molnar and Tapponier (1975) speculate that the Baikal rift may be related to the collision of India and Eurasia.

Two additional plates have been postulated in the region. Minster et al. (1974) proposed a Bering plate, comprising western Alaska, the Bering sea and northeast Asia, to explain a systematic misfit of slip vectors from Aleutian and Kuril trench earthquakes to the Pacific-North American rotation pole. Though intraplate deformation in Alaska is no doubt occuring, the misfit of slip vectors can also be explained by propagation effects due to seismic velocity heterogenetities associated with subduction of the Pacific plate (E.R. Engdahl, personal communication, 1974). We do not consider a Bering plate further below.

Den and Hotta (1973) proposed the existence of an Okhotsk plate during the Mesozoic and early Cenozoic on the basis of structural trends and orogenic belts in and around the Sea of Okhotsk, though their discussion does not require a distinct Okhotsk plate at present.

Several alternative plate descriptions for northeast Asia are considered in Figure 4. The alternatives shown do not exhaust all possibilities but include most of those commonly proposed or assumed. A shared feature of all plate models is that the boundary between the Eurasian and North American plates continues from the Nansen ridge onto the Siberian continental shelf in the Laptev sea and along the active seismic belt in Yakutia (Figure 2). Demenitskaya and Karasik (1969), Grachev et al. (1970), and Churkin (1972) have similarly drawn the plate boundary though this region, on the basis of seismicity, recent faulting and Quaternary volcanic activity. The descriptions of Figure 4 differ in how the Eurasian-North American plate boundary is continued to a triple junction with the Pacific or with another plate.

Description A in Figure 4 includes three plates (Eurasian, North American and Pacific) and a Eurasian-North American boundary through Kamchatka. Given the EUA-NA pole of rotation (Table 2), such a hypothetical boundary would be a convergence zone. The boundary should be a locus of thrust faulting. However, the only faults in Kamchatka which trend in a direction approximately parallel to such a proposed boundary, those in the Kronoki-Krutogorova fault zone, are strike-slip in character. Description A is thus unlikely.

Description B includes four plates: Eurasian, North American, China and Pacific. China and Eurasia would have a boundary striking north-south through Sakhalin. Adopting Morgan's (1972) pole of rotation for CHI-EUA gives almost

pure (right-lateral) strike slip movement on meridional faults through Sakhalin; a EUA-CHI pole near Lake Baikal also predicts (left-lateral) strike slip motion on such faults. Neither tectonic evidence nor earthquake source mechanisms (below) bear this out. Description B also encounters the same difficulty in Kamchatka as does case A. Description B is unlikely.

Description C includes three plates (Eurasian, North American, and Pacific) with the EUA-NA border trending north-south through Sakhalin and Hokkaido to a triple junction in the Japan trench. From the EUA-NA pole of rotation, thrust faults (striking roughly north-south) with a small amount of superposed right-lateral motion would be expected on Sakhalin and Hokkaido, in good agreement with the tectonic evidence discussed above and the earthquake mechanisms discussed below. We thus consider this description to be an acceptable plate tectonic interpretation of much of the seismic and geologic data, through it does not account for intraplate deformation in northeast U.S.S.R., China or Alaska.

Description D has four plates (Eurasian, North American, China, and Pacific) with a CHI-NA boundary through Sakhalin (cf. Morgan, 1968, 1972). Morgan's (1972) CHI-NA pole of rotation is at 54°N, 130°E and predicts (right-lateral) strike slip motion on meridional faults in Sakhalin, in disagreement with observations. While one may argue that the motion of the China plate has large uncertainties, this exercise and the syntheses of Molnar et al. (1973) and Molnar and Tapponier (1975) imply the concept of a rigid China plate is of dubious value.

Description E includes the existence of a separate Okhotsk plate (after Den and Hotta, 1973), along with the Eurasian, North American, and Pacific

plates. This interpretation of the seismicity and tectonic data cannot be excluded; indeed a cursory examination of the seismicity in Figure 2 lends support to the notion of a separate Okhotsk plate, though the limited seismicity in the Sea of Okhotsk precludes a definitive proof. Also because of the small rates and sparse data, no pole of rotation for OKH relative to any other plate can be computed so the hypothesis of an Okhotsk plate has no predictive value. Therefore we see no positive reason for the addition of another plate when the data can be explained with only a three plate configuration.

Of all the possibilities in Figure 4, then, configuration C is preferable. This description is one of the simplest, involving only three distinct plates. The description provides adequate explanation of the seismicity and tectonics of Sakhalin and Hokkaido. And as we show in a later section, this description has predictive value for describing the slip vectors of earthquakes on Sakhalin and Hokkaido.

EARTHQUAKE SOURCE MECHANISMS

As an aid in confirming the plate description discussed in the preceding section and in elucidating the tectonics of an intracontinental plate boundary, we have determined the earthquake source mechanisms for all earthquakes in northeast Asia of a sufficiently large magnitude for global coverage. We present solutions for events in the continental shelf in the Laptev sea, Yakutia, Sakhalin, the Tartar strait, and Hokkaido.

These source mechanisms were determined by utilizing P-wave first motions, S-wave polarizations, and Rayleigh wave amplitudes (Figure 5, Table 3). The technique for determining source geometry from the amplitude of the vertical component of Rayleigh waves is described by Forsyth (1973). We utilized Rayleigh wave amplitudes at a period of 67 seconds, and corrected for

attenuation with a value of Q equal to 125. The solution which was compatible with the P-wave data and had a minimum least square error in amplitude was adopted as the correct mechanism.

Event 1 occured on the continental shelf in the Laptev sea, southeast of the Nansen ridge. P-wave data determined one nodal plane, and surface wave amplitudes were used to define the other nodal plane. This event is clearly a normal faulting event, and indicates that sea-floor extension occurs on the shelf as a continuation of the Nansen ridge. This earthquake was also studied by Conant (1972), who obtained non-orthogonal nodal planes from P-wave first motions (see also Figure 5), an artifact of the heterogeneous seismic velocity structure beneath the spreading center (Solomon and Julian, 1974). Sykes (1967) obtained a similar solution from an earlier, nearby event.

Events 2 and 3 occured in Yakutia. Filson and Frasier (1972) obtained a similar solution for event 2. The location of aftershocks (Belyy et al., 1971) from event 2 indicates that the fault plane for that earthquake strikes northwest. The inferred solution is almost pure left-lateral strike slip motion. Event 3, studied also by Oristaglio (unpublished manuscript, Senior essay, Yale University, New Haven, Connecticut, 1974), is similar in mechanism to event 2 but has slightly different nodal-plane strikes and is less well constrained by the data. Because of the similarity in these solutions and their proximity, it might be assumed that the northwest striking plane is the fault plane for event 3 also. Lazareva and Misharina (1965) also list strike-slip fault plane solutions for two Yakutia earthquakes in this seismic belt (72°N, 127°E and 66°N, 137°E), but we are unable to assess the quality of these solutions.

Event 4, located in central Sakhalin, appears to be almost pure thrust,

but there are not enough data to tightly constrain the solution. Events 5-9 occured in the Tartar strait off the southwest coast of Sakhalin. Events 6-9 are part of an aftershock sequence following event 5. For this reason, we required these mechanism solutions to be generally similar while still satisfying the data. We thus obtain five mechanisms which are all predominantly thrust events. The fault plane was chosen in order to satisfy several criteria: the plane exhibit some right-lateral motion to agree with the field geologic data on the faults in Sakhalin, the plane should have a strike similar to the local faults, and the fault should be in agreement with the shape of the isoseismal contours (Solov'yev et al., 1973). All five earthquakes occured at about 20 km depth. Thus their fault plane solutions should probably agree with the strike and slip of the surface faults, but not necessarily the dip, since thrust faults are commonly shallower in dip at depth. This sequence of earthquakes has the first two mechanisms similar (5 and 6) and the last three (7 to 9) all similar but with a slightly different fault plane from the first group. All had a nearly identical auxiliary plane, however. It is of interest that McKenzie (1970) found an aftershock sequence in the Mediterranean region which similarly had a constant slip vector, but a differing fault plane, for each individual event.

Event 10 occured in Hokkaido at a depth of 25 km beneath the Hidaka mountains. We consider it to be unrelated to underthrusting of the Pacific plate because of its shallow depth and even shallower aftershock sequence, and because of the orientation of the fault plane. From the aftershock distribution (Moriya, 1972) the shallowly dipping plane was determined to be the fault plane. It thus was a thrust-fault event with a component of left-lateral strike slip motion.

A NEW EURASIAN-NORTH AMERICAN POLE

A logical question is whether these earthquake mechanism solutions are compatible with the earlier discussion of plate boundaries and with the EUA-NA pole of rotation. Event 1 implies that such a pole must be located south of 76.5°N, in order to have extension on that region of the shelf. If events 2 and 3 are both interpreted as left-lateral faulting occuring on a single plate boundary, the two slip vectors uniquely define a rotation pole at 65°N, 148°E. Such a pole, however, would be in systematic disagreement with fracture zone trends and earthquake slip vector data in the Atlantic and Arctic oceans. The pole would be well outside the 95% confidence ellipse of Minster et al. (1974). Consequently these two events cannot be indicative of rigid motion of the Eurasian and North American plates. Rather they are the product of complicated deformation in a boundary between two plates near the relative rotation pole for the same plates. We comment further on this point in the following section.

If the plate tectonic description of northeast Asia is as discussed above (case C, Figure 5), then sufficiently far from the EUA-NA pole, the slip vectors of earthquakes on the boundary should be predictable. Using the EUA-NA angular velocity vector of Minster et al. (1974), the slip vectors for earthquakes on Sakhalin and Hokkaido should have azimuths of about 75° to 80°. These values are very close to those observed (Figure 5, Table 3), lending substantial credence to the above identification of the North American-Eurasian plate boundary.

A logical next step is to recalculate the EUA-NA rotation pole using the new data. Combining the slip vectors for events 4, 5 and 7 through 10 (the slip vector for event 6 is poorly constrained) with essentially the data set

(Table 4) for EUA-NA rotation of Minster et al. (1974), we obtain a EUA-NA pole at 61.8°N, 130.0°E, with a rate of 2.48 X 10^{-7} deg/yr (Figure 7). Such a location is approximately 7° south of the Minster et al.(1974) pole but is within their 95% confidence ellipse. Therefore it is not a statistically significant improvement over the Minster et al. (1974) pole, rather it is a pole of rotation which explains a larger data set. This pole of rotation describes the relative motion of the Eurasian and North American plates in the Atlantic, the Arctic, and in Sakhalin and Hokkaido. It does not describe the motion within about 10° of the rotation pole (e.g., events 2 and 3).

ON THE NATURE OF INTRACONTINENTAL PLATE BOUNDARIES

The intracontinental portion of the boundary between the Eurasian and North American plates has several characteristics which distinguish it from the more common submarine plate boundaries. We comment on these characteristics in this section, with occasional generalizations to other intracontinental plate edges.

The plate boundary in Yakutia is very wide and diffuse. At its widest, the boundary (if indeed such a term is still appropriate) is 600 km wide. The diffuse nature of the boundary is more likely a property of continental lithosphere than due to the slow relative plate velocity. The width of the seismic zone increases markedly between the Nansen ridge (oceanic lithosphere) and its extension onto the continental shelf in the Laptev sea (Figures 1 and 2). Other intracontinental plate boundaries of different types and with different relative plate velocities share this very extended character; western North America (Atwater, 1970) is a good example. That continental lithosphere is generally thicker than oceanic lithosphere may be part of the answer for the diffuse definition of the intracontinental edges of plates. More important, probably, is that continental lithosphere

is very heterogeneous, a complex cementation of blocks and belts of different make-up, texture and age. Compared to the relatively fresh and relatively homogeneous oceanic plates, continents have generally undergone a long history of stress- and fracture-producing tectonic activity and are crisscrossed with weak zones highly susceptible to deformation when stressed.

The relative rotation pole is near the plate boundary. It is sometimes difficult to separate cause and effect in a physical phenomena, but we speculate that the location of the Eurasian-North American rotation pole very near the intracontinental boundary between these two plates is not coincidence. Rather it is likely related to a greater asthenospheric resistance to moving continental than oceanic lithosphere in general (Solomon et al., 1975; Forsyth and Uyeda, 1975) and to a difficulty in subducting one continental block beneath another (McKenzie, 1969), particularly without first closing an intervening ocean. The situation is not quite that simple, since the plates are responding to a number of different types of forces (Solomon and Sleep, 1974). Nonetheless there are at least two other possible examples of where a relative rotation pole is located near the intracontinental portion of a plate boundary: the Pacific-Indian pole is not far from New Zealand and the African-Eurasian pole is not far from the straits of Gibraltar.

The displacements during large earthquakes are not predictable near the relative rotation pole. This characteristic is related to the previous two. Because the rotation pole is near the plate boundary, the stress system in the boundary zone changes rapidly with small changes in distance. Structural heterogeneities modulate the stress field and the material response to stress. Aggravating the complexity of the stress and stress release fields is that the

instantaneous rotation pole is not fixed, but migrates with respect to the two plates (Pitman and Talwani, 1972).

The modern boundary is closely related to ancient plate boundaries. The broad seismic belt in Yakutia (Figure 2) marking the location of the current Eurasian-North American plate boundary lies within the Cherskiy-Verkhoyansk foldbelts, which Churkin (1972) has interpreted as a fossil suture marking the early Cretaceous collision of two continental blocks. The current plate boundary through Sakhalin and Hokkaido (Figure 6) follows closely a Mesozoic plate boundary marking the locus of eastward subduction of one plate beneath another (Sugimura and Uyeda, 1973; Den and Hotta, 1973). This is a familiar story in the plate tectonic evolution of the earth's surface: fossil plate boundaries are apparently relatively weak portions of continental blocks and are the preferred sites for creation of new plate edges.

CONCLUSIONS

Though plate boundaries within continents can rarely be defined with precision, the boundary between the Eurasian and North American plates between the Arctic and Pacific oceans can be identified on the basis of seismicity, recent tectonics and earthquake source mechanisms. The simplest plate configuration that adequately accounts for these data continues the Eurasian-North American boundary from the Nansen ridge through a broad seismically active zone in northeast U.S.S.R. to the Sea of Okhotsk and thence southward through Sakhalin and Hokkaido. With this configuration, the slip vectors derived from earthquake mechanisms in Sakhalin and Hokkaido are predicted from the EUA-NA relative rotation pole. A new pole, only slightly different from other recent solutions, is computed on the basis of the additional slip vector data.

The intracontinental plate boundary is spread over a width of as much as 600 km, and tends to follow ancient plate margins. Deformation in the vicinity of the rotation pole, which lies near the boundary, is poorly described by rigid-plate tectonics. These features can be explained by the thickness and heterogeneity of continental lithosphere and by the influence of continents on the forces moving the plates.

Acknowledgements

We are grateful to Donald Forsyth for numerous discussions and computer programs, and to Chris Scholz and John Kelleher for critical review of this manuscript. This research was supported partially by the Earth Sciences Section, National Science Foundation, NSF grant DES74-21894 and partially by the Advanced Research Projects Agency and monitored by the Air Force Office of Scientific Research under contracts F44620-71-C-0049 and F44620-75-C-0064.

REFERENCES

Academy of Sciences USSR, Earthquakes in the USSR: 1963-1970, (In Russian), Nauka Press, Moscow, 1966-1973.

Alverson, D.C., D.P. Cox, and A.J. Woloshin, Atlas of Asia and Eastern Europe, U.S. Geological Survey, Washington, D.C., 1967.

Atwater, T., Implications of plate tectonics for the Cenozoic tectonic evolution of western North America, Bull. Geol. Soc. Amer., 81, 3513, 1970.

Belyy, V.R., A.P. Valpeter, and V.M. Merzlyakov, Strong earthquake is the northeastern USSR, (In Russian), Priroda, No. 12, 64, 1971.

Chapman, E.D., Structure and tectonics of the Arctic region, M.S. thesis, Massachusetts Institute of Technology, Cambridge, 1973.

Chase, C.G., The N plate problem of plate tectonics, Geophys. J. Roy. Astron. Soc., 28, 117, 1972.

Churkin, M., Jr., Western boundary of the North American continental plate in Asia, Geol. Soc. Amer. Bull., 83, 1027, 1972.

Conant, D.A., Six new focal mechanism solutions for the Arctic and a center of rotation for plate movements, M.A. thesis, Columbia University, New York, 1972.

Cormier, V., Tectonics near the junction of the Aleutian and Kurile-Kamchatka arcs and the mechanism for middle Tertiary magmatism in the Kamchatka basin, Geol. Soc. Amer. Bull., 86, 443, 1975.

Das, S., and J. Filson, A plate model of Asian tectonics (abstract), Trans. Am. Geophys. Union, 55, 301, 1974.

Demenitskaya, R. M., and A. M. Karasik, The active rift system of the Arctic Ocean, Tectonophysics, 8, 345, 1969.

Den, N., and H. Hotta, Seismic refraction and reflection evidence supporting plate tectonics in Hokkaido, Pap. Meterol. Geophys., 24, 31, 1973.

Filson, J., and C.W. Frasier, The source of a Siberian earthquake (abstract), Trans. Am. Geophys. Union, 53, 1041, 1972.

Fleming, H.S., N.Z. Cherkis, and J.R. Heirtzler, The Gibbs fracture zone: a double fracture zone at 52°30'N in the Atlantic ocean, Mar. Geophys. Res., 1, 37, 1970.

Florensov, N.A., Rifts of the Baikal mountain region, Tectonophysics, 8, 443, 1969.

Forsyth, D.W., Anisotropy and the structural evolution of the oceanic upper mantle, Ph.D. tnesis, Massachusetts Institute of Technology, Cambridge, 1973.

Forsyth, D.W., and S. Uyeda, On the relative importance of driving forces of plate motion, Geophys. J. Roy. Astron. Soc., in press, 1975.

Gal'tsev-Bezyuk, S.D., Types of orogeny and orogenic phases on Sakhalin in the Cenozoic, Geotectonics, English transl., 1, 14, 1968.

Grachev, A.F., R.M. Demenitskaya, and A.M. Karasik, The mid-Arctic ridge and its continental continuation, (in Russian), Geomorphology, No. 1, 42, 1970.

Gutenberg, B., and C.F. Richter, Seismicity of the earth and associated phenomena, Princeton University Press, Princeton, New Jersey, 1949.

Herrin, D., Seismological tables for P phases, Bull. Seismol. Soc. Amer., 58, 1196, 1968.

Hodgson, J.H., M. Bath, H., Jenson, A. Kvale, N.A. Linden, L.M. Murphy, N.V. Shebalin, E. Tryggvason, and E. Vesanen, Seismicity of the Arctic, in Annals of the International Geophysical Year, edited by V. Beloussov, 30, 33, Pergamon Press, New York, 1965.

Horsfield, W.T., and P.I. Maton, Transform faulting along the De Geer line, Nature, 226, 256, 1970.

Int. Geod. and Geophys. Union, International Seismological Summary (1918-1963), Int. Seismol. Cent., Edinburgh, Scotland, 1923-1969.

Int. Seismol. Cent., Regional Catalogue of Earthquakes, 1-7, Int. Seismol. Cent., Edinburgh, Scotland, 1966-1973.

Johnson, G.L., North Atlantic fracture zones near 53°, Earth Planet. Sci. Lett., 2, 445, 1967.

Johnson, G.L., and O.B. Eckhoff, Bathymetry of the north Greenland Sea, Deep-Sea Res., 13, 1161, 1966.

Johnson, G.L., J.R. Southall, P.W. Young, and P.R. Vogt, Origin and structure of the Iceland plateau and Kolbeinsey ridge, J. Geophys. Res., 77, 5688, 1972.

Karasik, A.M., Some features and problems of sea-floor spreading near the pole of opening, Int. Union of Geodesy and Geophysics, XV General Assembly, Abstract 1-5, 9, 1971.

Lazareva, A.P., and L.A. Misharina, Stresses in earthquake foci in the Arctic seismic belt, Izv. Earth Physics, English transl., No. 2, 84, 1965.

Le Pichon, X., Sea floor spreading and continental drift, J. Geophys. Res., 73, 3661, 1968.

Le Pichon, X., J. Francheteau, and J. Bonnin, Plate Tectonics, 300 pp, Elsevier Scientific Publishing Co., New York, 81, 1973.

Linden, N.A., Seismicity of the Arctic region, in Annals of the International Geophysical Year, 1, 375, Pergamon Press, New York, 1961.

Mc Kenzie, D. P., Speculations on the consequences and causes of plate motions, Geophys. J. Roy. Astron. Soc., 18, 1, 1969.

Mc Kenzie, D. P., Plate tectonics of the Mediterranean region, Nature, 226, 239, 1970.

Minster, J. B., T. H. Jordan, P. Molnar, and E. Haines, Numerical modeling of instantaneous plate tectonics, Geophys. J. R. Roy. Astron. Soc., 36, 541, 1974.

Molnar, P., T. J. Fitch, and F. T. Wu, Fault plane solutions of shallow earthquakes, Earth Planet. Sci. Lett., 19, 101, 1973.

Molnar, P., and P. Tapponnier, Tectonics of Asia: Consequences and implications of a continental collision, Science, 189, 419, 1975.

Morgan, W. J., Rises, trenches, great faults, and crustal blocks, J. Geophys. Res., 73, 1959, 1968.

Morgan, W. J., Plate motions and deep mantle convection, in Studies in Earth and Space Sciences, Geol. Soc. Amer. Mem., 132, 7, 1972.

Moriya, T., Aftershock activity of the Hidaka mountain earthquake of January 21, 1970, (In Japanese), Zisin, 24, 287, 1972.

National Oceanic and Atmospheric Administration, Seismicity of the Arctic Region, NEIC 3020, Boulder, 1970.

National Oceanic and Atmospheric Administration, Preliminary Determination of Epicenters, Monthly Listing, Boulder, 1970-1973.

Pitman, W. C., III, and M. Talwani, Sea-floor spreading in the North Atlantic, Geol. Soc. Amer. Bull., 83, 619, 1972.

Pushcharovskiy, Yu. M., The tectonics of Sakhalin, Int. Geol. Rev., 7, 2184, 1965.

Rassokho, A.I., L.I. Senchura, R.M. Demenitskaya, A.M. Karasik, Yu. G. Kicelev, and N.K. Timoshenko, The mid-Arctic range as a unit of the Arctic ocean mountain system, Dokl. Akad. Nauk SSSR, 172, 659, 1967.

Rozhdestvenskiy, V.S., Strike-slip faults in the Vostochnyy range of Shmidt peninsula on Sakhalin, Int. Geol. Rev., 15, 1391, 1973.

Savarensky, E.F., S.L. Solov'yev, and D.A. Kharin, Atlas of Earthquakes in the USSR, Moscow, 1962.

Solomon, S.C., Shear wave attenuation and melting beneath the mid-Atlantic ridge, J. Geophys. Res., 78, 6044, 1973.

Solomon, S.C., and B.R. Julian, Seismic constraints on ocean-ridge mantle structure: anomalous fault-plane solutions from first motions, Geophys. J. Roy. Astron. Soc., 38, 265, 1974.

Solomon, S.C., and N.H. Sleep, Some simple physical models for absolute plate motions, J. Geophys. Res., 79, 2557, 1974.

Solomon, S.C., N.H. Sleep, and R.M. Richardson, On the forces driving plate tectonics: inferences from absolute plate velocities and intraplate stress, Geophys. J. Roy. Astron. Soc., in press, 1975.

Solov'yev, S.L., Seismicity of Sakhalin, Bull. Earth. Res. Inst. Univ. Tokyo, 43, 95, 1965.

Solov'yev, S.L., N.N Leonov, L.S. Oskorbin, L.F. Volkova, and E.A. Vorov'yeva, The Moneron earthquake of 5-6 September 1971, Dokl. Akad. Nauk. SSSR, English transl., 212, 3, 1973.

Sugimura, A., and S. Uyeda, Island Arcs, Elsevier Scientific Publishing Co., New York 1973.

Suprenko, O.I., T.A. Andiyeva, and P.N. Safronov, The sublatitudinal Kronoki-Krutogorova fault zone of Kamchatka, Dokl. Akad. Nauk. SSSR, English transl, 209, 92, 1973.

Suprenko, O.I., and G.P. Dekin, Sublatitudinal faults of eastern Kamchatka, Dokl. Akad. Nauk SSSR, English transl., 180, 112, 1968.

Sykes, L.R., The seismicity of the Arctic, Bull. Seismol. Soc. Amer., 55, 519, 1965.

Sykes, L.R., Mechanism of earthquakes and nature of faulting on the mid-oceanic ridges, J. Geophys. Res., 72, 2131, 1967.

Talwani, M., C.C. Windisch, and M.G. Langseth, Reykjanes ridge crest: a detailed geophysical study, J. Geophys. Res., 76, 473, 1971.

Zakharov, V.K., and G.G. Yakushko, Modern vertical crustal movements in southern Sakhalin as determined by repeated surveying, Dokl. Akad. Nauk SSSR, English transl., 207, 45, 1972.

Zanyukov, V.N., The central Sakhalin fault and its role in the tectonic evolution of the island, Dokl. Akad. Nauk. SSSR, English transl., 196, 85, 1971.

TABLE 1

RELOCATED EARTHQUAKES IN NORTHEAST USSR

Date	Origin Time (G.M.T.) h	m	s	Latitude	Longitude
Nov. 30, 1918	06	48	38.2	70.704°N	133.363°E
Mar. 13, 1924	10	41	58.7	62.772	150.062
Mar. 15, 1924	10	31	21.3	49.176	142.570
May 27, 1924	20	09	30.3	62.452	135.056
Feb. 18, 1925	11	36	3.7	66.614	145.648
Apr. 9, 1926	10	4	32.0	72.865	132.093
June 10, 1927	18	13	23.4	48.364	139.067
Nov. 14, 1927	00	12	7.4	70.233	128.733
Nov. 14, 1927	04	56	29.5	70.208	128.990
Nov. 15, 1927	21	48	45.7	70.275	129.069
Feb. 3, 1928	13	47	36.5	70.374	128.126
Feb. 21, 1928	19	49	6.0	67.573	-172.561
Feb. 24, 1928	14	10	25.4	67.536	-173.824
Feb. 26, 1928	01	19	12.8	67.195	-171.034
Aug. 16, 1928	07	36	44.6	69.842	123.130
Aug. 25, 1928	01	48	32.1	49.060	141.814
July 15, 1931	16	27	0.6	59.082	148.185
Oct. 10, 1931	16	37	8.4	59.504	148.027
July 10, 1932	00	43	26.3	52.642	142.052
Sept. 7, 1933	22	39	20.3	61.963	177.429
Oct. 25, 1935	17	38	14.6	51.854	142.887
Nov. 3, 1936	04	43	23.2	59.198	152.815
May 10, 1947	00	07	14.5	57.858	141.908
Apr. 14, 1951	13	33	2.1	61.117	136.306

Note: All depths were constrained to be 15 km.

TABLE 2. EURASIAN - NORTH AMERICAN RELATIVE ANGULAR VELOCITY VECTOR

Rotation Pole		Rotation	Technique	Reference
Latitude	Longitude	10^{-7} deg/yr		
78°N	102°E	2.8	4 fracture zone trends, 1 rate	Le Pichon (1968)
64°N	138°E		Rotation of Lomonosov ridge to Eurasia	Karasik (1971)
68°N	137°E	2.78	Rotation of magnetic anomaly 5	Pitman and Talwani (1972)
48°N	155°E	2.36	Global inversion	Chase (1972)
60°N	135°E	2.07	Global fit	Morgan (1972)
63°N	137°E		Fracture zone trends	Le Pichon et al. (1973)
69.3°N	128.0°E	2.7	Global inversion	Minster et al. (1974)
61.8°N	130.0°E	2.48	See Table 4	This study

TABLE 3

EPICENTER AND SOURCE MECHANISM DATA

Event	Date	Time (G.M.T.)	Latitude	Longitude	Plane A Strike/Dip		Plane B Strike/Dip	
1	4-7-69	20:26:30.5	76.55°N	130.86°E	120°	64°NE	332°	30°SW
2	5-18-71	22:44:43.8	64.0°N	146.1°E	43°	89°SE	313°	83°NE *
3	1-13-72	17:24:23.2	61.94°N	147.04°E	320°	66°SW	47°	84°SE
4	10-2-64	00:58:39.2	51.95°N	142.92°E	328°	54°W	348°	38°E *
5	9-5-71	18:35:27.0	46.54°N	141.15°E	347°	58°W	0°	32°E *
6	9-6-71	13:37:10.1	46.76°N	141.39°E	10°	63°W	16°	27°E *
7	9-8-71a	11:48:25.9	46.44°N	141.09°E	340°	62°W	40°	46°E *
8	9-8-71b	16:59:54.8	46.28°N	141.03°E	337°	61°W	33°	45°E *
9	9-27-71	19:01:46.4	46.41°N	141.16°E	344°	64°W	38°	40°E *
10	1-20-70	17:33:03.1	42.48°N	143.04°E	339°	71°W	300°	24°NE *

*Fault Plane

TABLE 4

DATA FOR COMPUTATION OF POLE OF ROTATION

	Latitude	Longitude	Observed	Uncertainty	Error	Reference
Rates,	85.0°	90.0°	1.0	0.4	-0.1	Rassokho et al., 1967
cm/yr	70.0	-18.0	1.6	0.3	-0.4	Johnson, 1967
	60.0	-29.0	2.4	0.2	0.1	Talwani et al., 1971
	45.0	-28.0	2.8	0.3	0.2	Pitman and Talwani, 1972
Azimuths,	80.2	-1.0	130.	10.	2.0	Horsfield and Maton, 1970
degrees:	79.8	2.9	137.	10.	6.3	Conant, 1972
	79.8	2.4	134.	10.	3.7	Chapman, 1973
	79.6	2.5	128.	10.	-2.2	Johnson and Eckhoff, 1966
	71.0	-8.0	115.	5.	-2.0	Johnson et al., 1972
	70.9	-7.0	116.	10.	-1.6	Conant, 1972
	66.7	-18.2	115.	10.	5.9	Conant, 1972
	66.3	-19.8	107.	10.	-1.0	Sykes, 1967
	52.9	-34.2	95.	10.	-3.1	Solomon, 1973
	52.5	-35.0	96.	4.	-1.7	Johnson, 1967
	52.5	-33.5	95.	4.	-3.5	Fleming et al., 1970
	51.9	142.9	58.	10.	-2.0	This study (4)
	46.5	141.1	77.	10.	5.5	This study (5)

46.4	141.1	70.0	10.	-1.7	This study (7)
46.3	141.0	67.0	10.	-5.0	This study (8)
46.4	141.2	74.0	10.	2.4	This study (9)
42.5	143.0	69.0	10.	-3.7	This study (10)

Computed EUA-NA Pole of Rotation

61.8°N 130.0°E .248°/my

Standard Deviation 5.38°

FIGURE CAPTIONS

Figure 1. Seismicity of the Arctic, 1962-1969, after Nat. Ocean. Atmos. Adm. (1970).

Figure 2. Shallow seismicity of northeast Asia, 1909-1973, azimuthal equal-area projection about 69.3°N, 128°E. The size of a symbol is proportional to (body-wave) magnitude M. Triangles indicate a seismograph station. Only events between latitudes 41° and 75°N and between longitudes 120° and 170°E are included. For clarity, no events are plotted in the Aleutian and Kuril trenches with $M < 5.5$ or on Sakhalin with $M < 4.0$.

Figure 3. Cenozoic tectonics of the Sea of Okhotsk region, simplified from Alverson et al. (1967).

Figure 4. Possible plate descriptions of the seismicity and tectonics in northeast Asia. The dashed lines indicate boundaries between plates. EUA = Eurasian, NA = North American, PAC = Pacific, CHI = China, OKH = Okhotsk.

Figure 5. Earthquake source mechanisms. Numbers refer to the event number in Table 2. Equal area projection of P-wave first motions and S-wave polarizations plotted on the lower focal hemisphere; closed circles are compression, open circles are dilatation. Triangles indicate short period data from the Bulletin of the Japanese Meterological Agency (event 4 only). All other data were read from long period WWSSN, Canadian network, and Lamont network seismograms. Rayleigh-wave amplitude radiation patterns are shown for events 1 and 6.

Figure 6. The Eurasian-North American plate boundary in northeast Asia. The newly computed EUA-NA pole of rotation is shown together with the 95% confidence ellipse. Locations of the pole of rotation from

other authors are also shown. Earthquake source mechanisms are from Figure 5; the compressional quadrants are shaded.

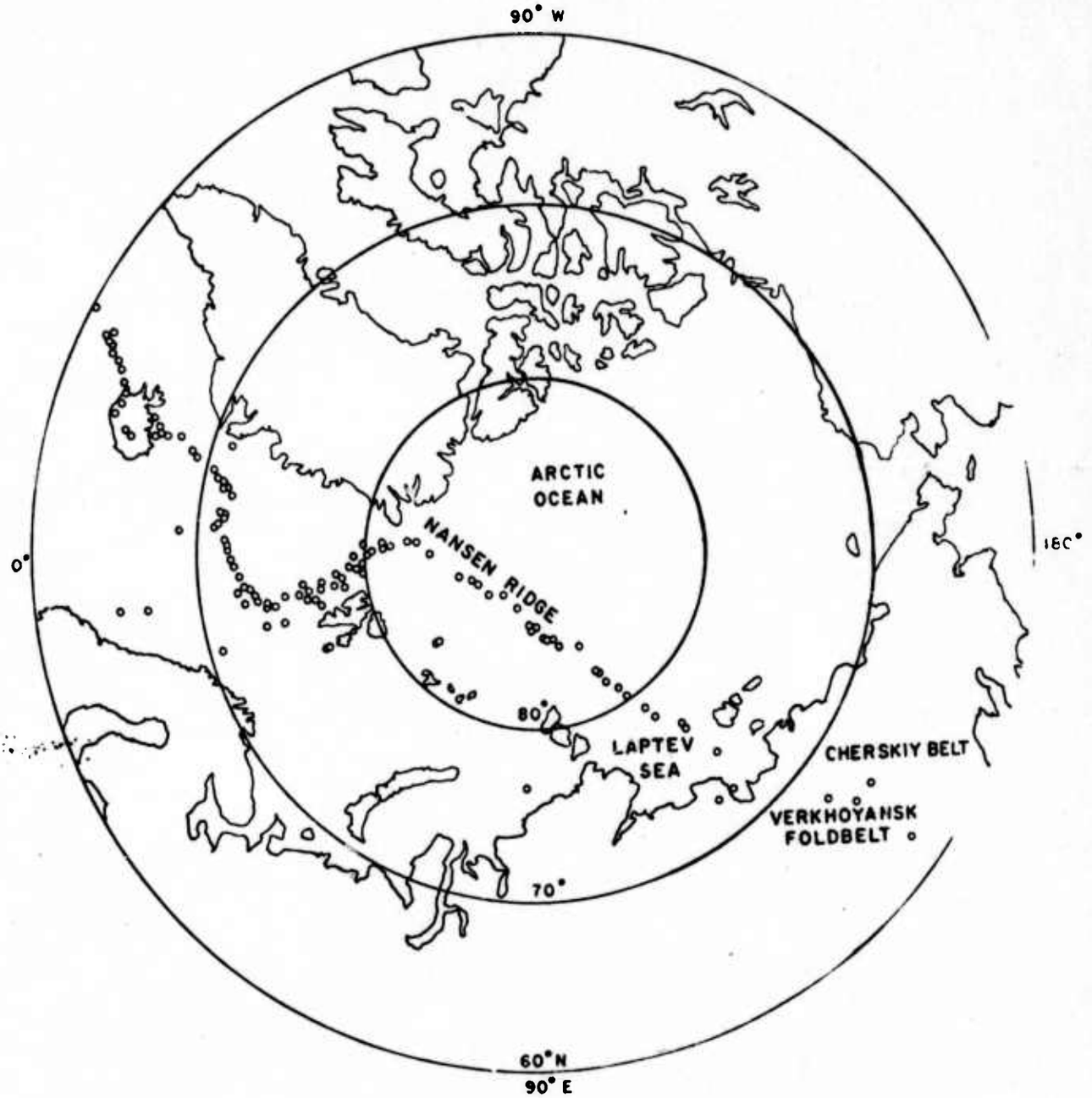
90° W
ARCTIC OCEAN
NANSEN RIDGE
0°
180°
80°
LAPTEV SEA
CHERSKIY BELT
VERKHOYANSK FOLDBELT
70°
60°N
90° E

Figure 1

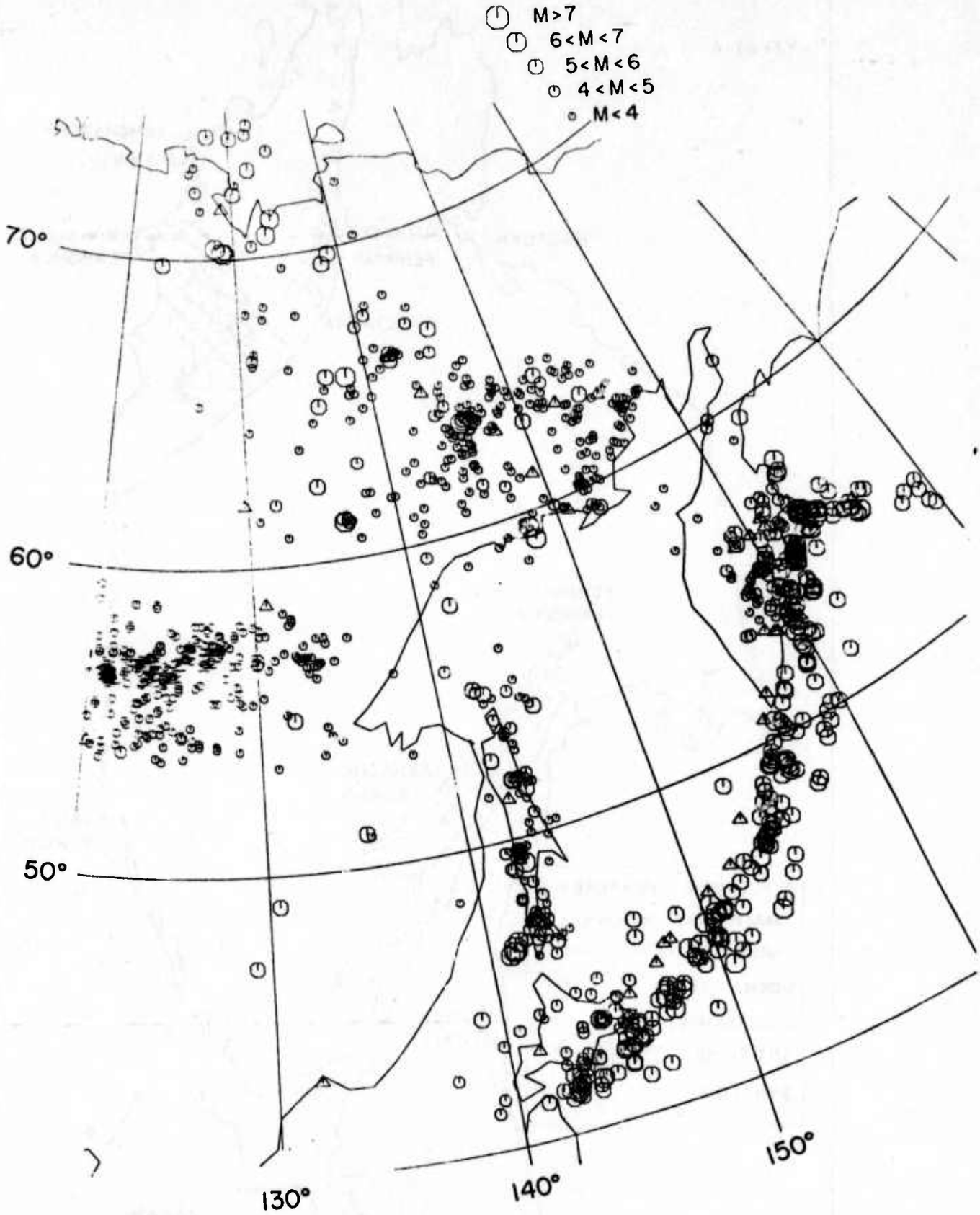

Figure 2

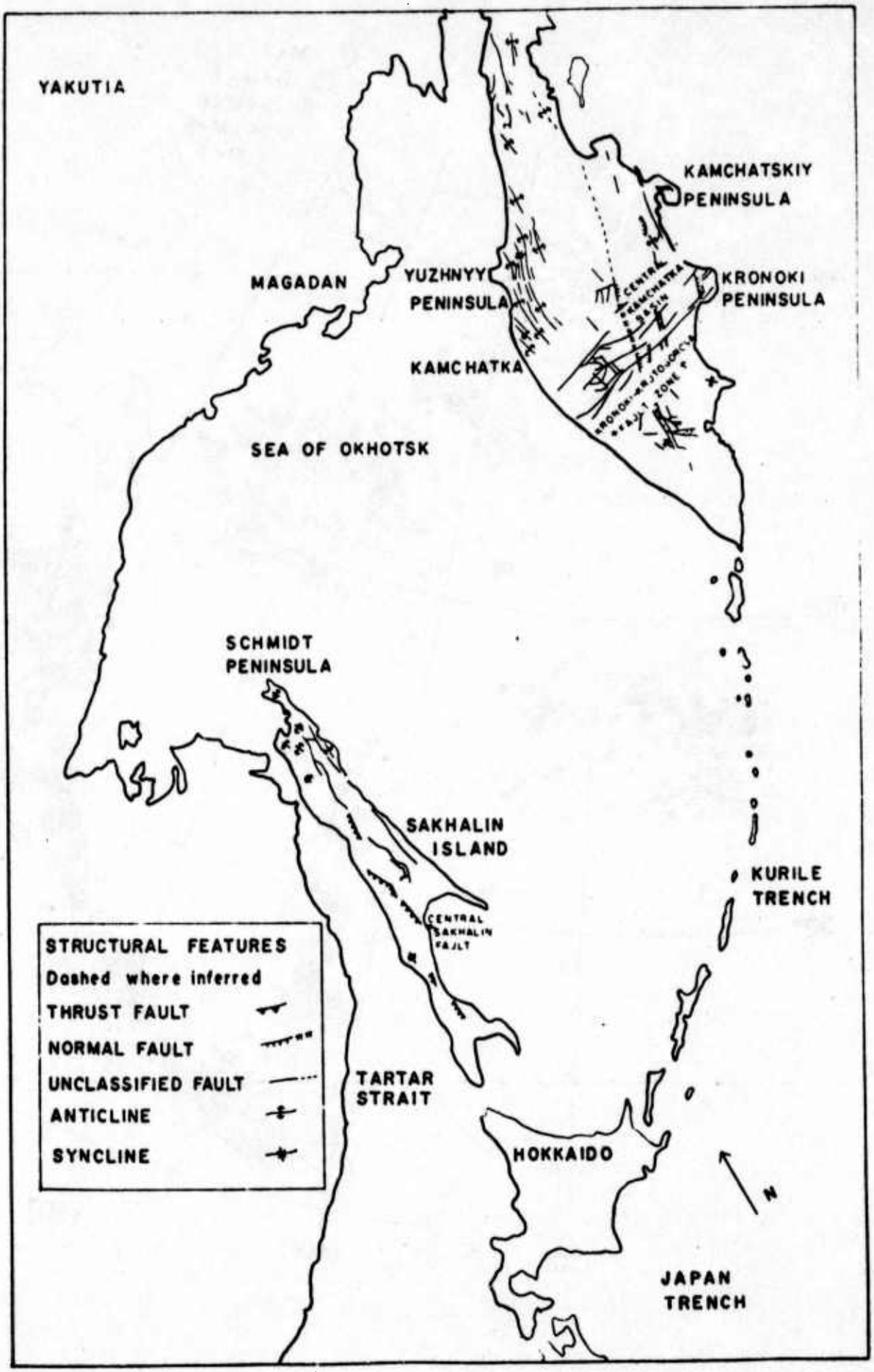
YAKUTIA
KAMCHATSKIY PENINSULA
MAGADAN
YUZHNYY PENINSULA
KRONOKI PENINSULA
CENTRAL KAMCHATKA BASIN
KAMCHATKA
KRONOKI-KURILSKOYE RIFT ZONE
SEA OF OKHOTSK
SCHMIDT PENINSULA
SAKHALIN ISLAND
KURILE TRENCH
CENTRAL SAKHALIN FAULT
STRUCTURAL FEATURES
Dashed where inferred
THRUST FAULT
NORMAL FAULT
UNCLASSIFIED FAULT
ANTICLINE
SYNCLINE
TARTAR STRAIT
HOKKAIDO
N
JAPAN TRENCH

Figure 3

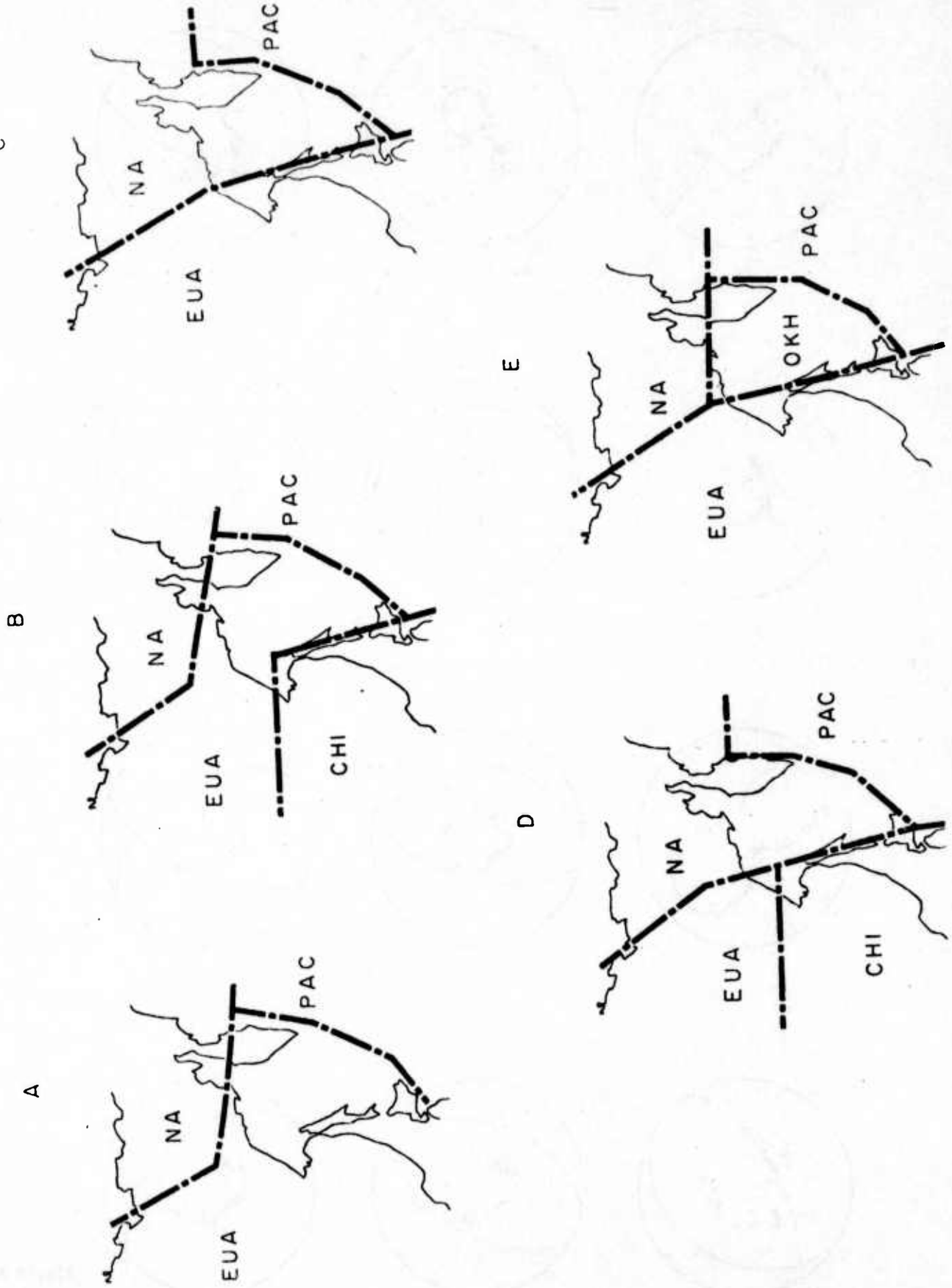
A
NA
PAC
EUA
B
NA
PAC
EUA
CHI
C
NA
PAC
EUA
D
NA
PAC
EUA
CHI
E
NA
OKH
PAC
EUA

Figure 4

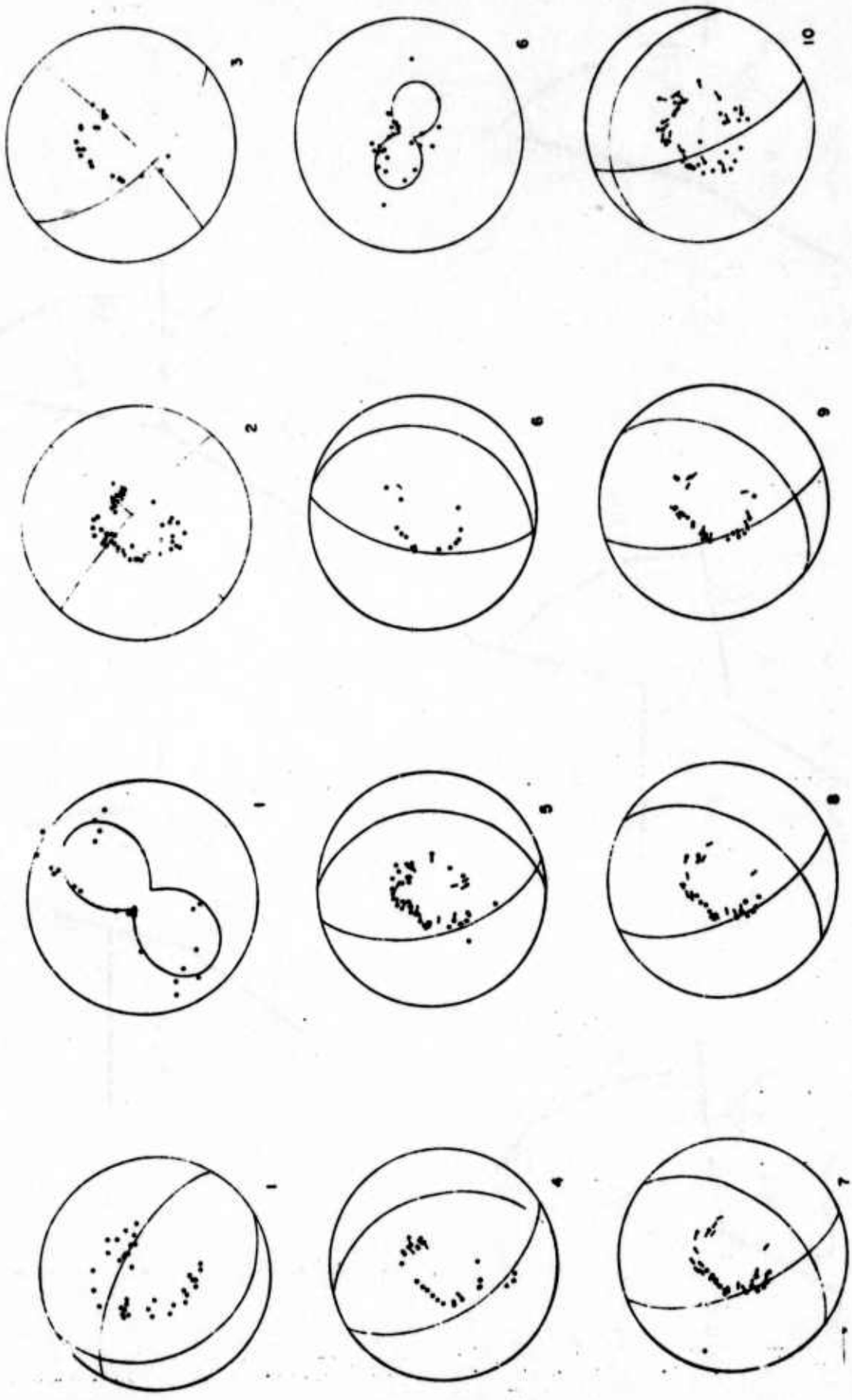

Figure 5

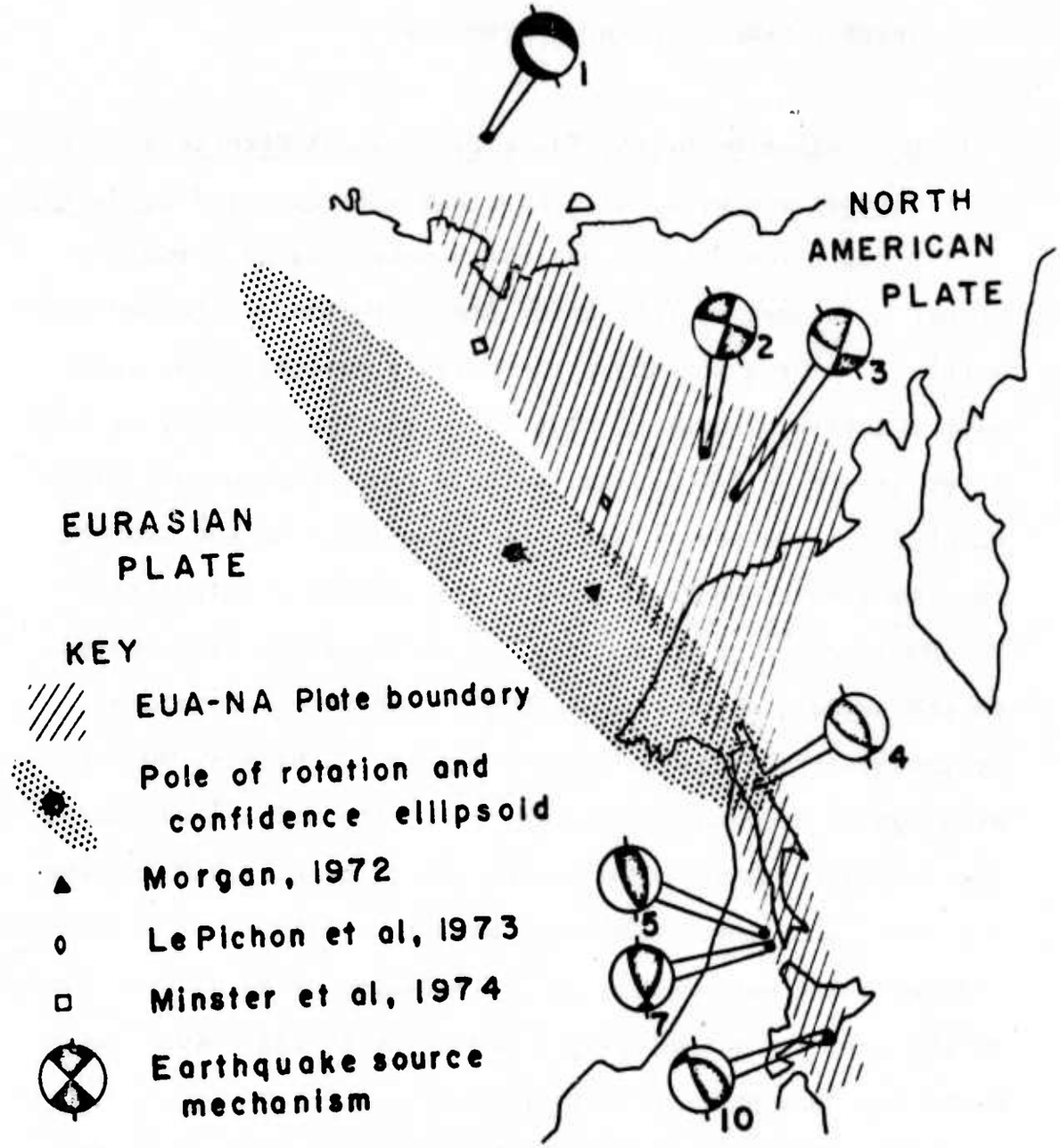
NORTH
AMERICAN
PLATE
EURASIAN
PLATE
KEY
EUA-NA Plate boundory
Pole of rotation and
confidence ellipsoid
Morgan, 1972
LePichon et al, 1973
Minster et al, 1974
Earthquake source
mechanism
1
2
3
4
5
7
10

Figure 6

4. THREE DIMENSIONAL EARTH STRUCTURE

4.1 Determination of the Three Dimensional Structure of the Lithosphere by K. Aki, A. Christoffersson and E. Husebye

A new three-dimensional earth modelling is formulated in order to meet an increasing demand for more detailed and accurate information about the earth's interior. We start with a layered medium of classic seismology, but divide each layer into many blocks and assign a parameter to each block which describes the velocity perturbation from the average for the layer. Our data is the teleseismic P travel time residuals observed at an array of seismographs distributed on the surface above the earth's volume we are modelling. By isolating various sources of errors and biases, we arrive at a system of equations to determine the model parameters. The solution was obtained by the use of generalized inverse and stochastic inverse methods with the analysis of resolution and errors in estimates. Our method also gives a lower limit of the true r.m.s. velocity fluctuation in the actual earth under the assumption of ray-theory.

Using NORSAR P-wave residuals, we have determined the three-dimensional seismic structure of the lithosphere under the array to the depth of 126 km. The true r.m.s. velocity fluctuation was found to be at least 3.4%. This is in agreement with estimates obtained from statistical analysis of

P time fluctuation based on the Chernov theory. The three-dimensional velocity anomalies are presented both by the generalized inverse and by the stochastic inverse solutions. We preferred the dual presentation, because it gives the reader greater freedom in judging the results than a single "optimal" solution. Both methods gave essentially the same results. The discrepancies, when they existed, were always explainable in terms of differences in the smoothing procedure which is explicitly given in the resolution matrix.

We found clear evidence of pipe-like structures under NORSAR, dipping northward and away from the surface contour of the Oslo graben. These pipe-like structures were interpreted as vestiges of magma ascent by penetrative convections associated with the Permian volcanism of the Oslo graben. The inclination of the pipe-like structures is interpreted as a result of plastic deformation of the lithosphere due to the shear exerted by the asthenosphere convection current driving the plate motion.

4.2 Preliminary Results on the 3-Dimensional Seismic Structure of the Lithosphere under the USGS Central California Seismic Array by E. Husebye, A. Christoffersson, K. Aki and C. Powell

ABSTRACT

About 1500 readings of teleseismic P-time residuals obtained from the U.S. Gological Survey seismic network in central California were used to determine a three-dimensional velocity anomaly by the method of Aki, Christoffersson and Husebye (1975). We found that the California network is less adequate than the LASA and NORSAR arrays because it has a greater proportion of peripheral region in which the resolution is very poor for the stochastic inverse and the random error effect is severe for the generalized inverse. Nevertheless, the resultant velocity anomalies show a remarkable correlation with the fault zone to the depth of 75 km. The anomaly pattern changes drastically as the depth exceeds 75 km, suggesting that the asthenosphere is reached at this depth.

4.3 Three-Dimensional Seismic Structure of the Lithosphere under Montana LASA by K. Aki, A. Christoffersson and E. Husebye

ABSTRACT

Using P-wave residuals for teleseismic events observed at the Montana LASA, we have determined the three-dimensional seismic structure of the lithosphere under the array to a depth of 140 km. The r.m.s. velocity fluctuation was found to be at least 3.2% which may be compared to estimates of ca 2% based on the Chernov random medium theory. The solutions are given by both the generalized inverse and stochastic inverse methods in order to demonstrate the relative merit of different inversion techniques.

The most conspicuous feature of the lithosphere under LASA is a low velocity anomaly in the central and NE part of the array siting area with the N60°E trend and persisting from the upper crust to depths greater than 100 km. We interpret this low velocity anomaly as a zone of weakness caused by faulting and shearing associated with the building of the Rocky Mountains.

Introduction

The seismic velocity structure beneath LASA has intrigued seismologists ever since this large aperture array was established in Montana in 1965. The interpretation of two dimensional seismological observations was novel to seismology and resulted in numerous papers dealing with the crust and upper mantle under LASA. For references, see Toksöz, Chinnery and Anderson (1967); Mack (1969); Greenfield and Sheppard (1969); Glover and Alexander (1969); Larner (1970); Engdahl and Felix (1971); Iyer and Healy (1972); Warren, Healy, Bohn and Marshall (1973); Aki (1973); and Capon (1974). Besides partly conflicting results these papers are facinating reading as they reflect an area of progress in seismology but at the same time serve to expose the enormity of the non-uniqueness problem inherent to inverting seismic observations. Experience with LASA has shown that conventional layered medium models used for interpreting seismic refraction and wide-angle reflection data cannot satisfactorily explain the observed P-wave travel time and amplitude anomalies.

Two fundamental problems are encountered in inversion of teleseismic P-wave travel time data; namely spatial resolution and flexibility in the basic model formulation. In the former case, we are concerned with the location of the structural inhomogeneities, e.g., whether the observed time residuals principally

originate in the lithosphere beneath the array (Iyer and Healy, 1972), in the mantle (Toksöz et al., 1967), in the lowermost part of the mantle or in the source region (Davies and Sheppard, 1972). In the case of model formulation, it should be pointed out that conventional layered models with uniform material properties cannot accomodate complex geological features. In fact, the antipode to conventional approaches is to assume that the seismic structure, say of the lithosphere, is so complex that it behaves as a medium with random inhomogeneities This type of model has successfully been introduced in the interpretation of LASA P-wave travel time and amplitude anomalies, by using the Chernov (1960) theory for wave propagation in random media (e g., see Aki 1973; Capon, 1974; and Berteussen, Christoffersson, Husebye and Dahle, 1975). The Chernov theory is based on a statistical description of the medium in terms of the mean square of fractional fluctuation of velocity, the correlation distance (the distance between two points in the medium at which velocity fluctuation becomes approximately uncorrelated), and the linear extent of the inhomogeneous region.

In this paper, we shall utilize our new earth modelling approach with velocity fluctuations similar to the Chernov medium but defined deterministically within the volume of

crust and upper mantle for estimating the three-dimensional seismic structures beneath LASA. First, we shall give a brief description of our earth modelling technique and then discuss our results in relation to available geophysical and geological information pertinent to the area.

Model Formulation

In this section a brief presentation is given of our earth modelling approach and the inversion technique of P-wave travel time residuals used for estimating velocity perturbations in crust and upper mantle (see Aki, Christoffersson and Husebye, 1975, hereafter referred to as Paper 1). The initial model, shown in Fig. 1, consists of homogeneous layers with constant thickness and fixed, average velocity and comprises a somewhat arbitrarily defined volume under the array containing the observed ray paths. The earth's structure outside the model (see Fig. 1) is denoted 'standard earth' and is assumed known. Each layer of the initial model is divided into many blocks, and within each layer the relative velocity perturbation m for a given block are defined as the average perturbation over all rays having most of the unperturbed path within the block.

Omitting all details which are given in Paper 1, the model for estimating velocity perturbation for the individual

blocks is given by:

$$\underline{T} = G\,\underline{m} + \underline{\varepsilon} \qquad (1)$$

where the elements of the $\underline{T}$ -vector are the travel time residuals minus their average over all sensors for each event. The G-matrix are calculated from the travel time each ray spends within each layer for the initial unperturbed model. The $\underline{m}$-vector contains the unknown block velocity perturbations and the ε-vector the higher order and error terms. The sum of the columns in G corresponding to a layer is identically zero, and therefore adding a constant to the velocity perturbations within a layer cannot affect $\underline{T}$. Thus the rank of G is less or equal to the number of blocks sampled by the observational data (or hit by the incoming rays) minus the number of layers in the model. This means that the velocity perturbations in one layer at best can be determined except for an additive constant and this makes the smoothing over consecutive layers not legitimate as discussed in Paper 1. We need independent data, say from refraction and reflection surveys, in order to determine the average velocity in each layer.

The method of least squares leads to solving the following equation:

$$G^T G\,\underline{m} = G^T \underline{T} \qquad (2)$$

Using the method of generalized inverse (Lancsoz, 1961), the solution is:

$$\underline{m}_g = (G^T G)^{-g} G^T \underline{T} \qquad (3)$$

The resolution matrix R (Bachus and Gilbert, 1968) is given by

$$R = VV^T \qquad (4)$$

where the V-matrix contains the eigenvectors corresponding to the non-zero eigenvalues of the $(G^T G)$-matrix. In case of the generalized inverse solution the elements of R corresponding to the best possible resolution, are:

$r_{ij} = 1 - \frac{1}{n}$ for $i = j$

$r_{ij} = -\frac{1}{n}$ for $i \neq j$ for blocks in the same layer

$r_{ij} = 0$ for $i \neq j$ for blocks in different layers

(n = number of blocks sampled in a layer)

If we assume that the covariance of the residual time or the $\underline{\varepsilon}$-vector in Equation (1) can be written as $\sigma^2 I$, the standard errors of the m_g-estimate would be:

$$[D^2(\underline{m}_g)]^{1/2} = (\sigma^2 V \Lambda_p^{-1} V^T)^{1/2} \qquad (5)$$

where the Λ_p-matrix contains the non-zero eigenvalues of the $(G^T G)$-matrix. It is shown in Paper 1 that

$$(\overline{\mu^2})^{1/2} = \left[\frac{1}{NB}\left(\underline{m}_g^T \underline{m}_g - \mathrm{tr}\, D^2(\underline{m}_g)\right)\right]^{1/2} \qquad (6)$$

represents an estimate of a lower limit for the true root mean square slowness perturbation $(\overline{\mu^2})^{1/2}$ in the volume of the earth sampled. NB is the total number of blocks sampled and tr represents the trace of a matrix.

An alternative to the generalized inverse approach is a special case of the stochastic inverse solution (Franklin, 1970), namely:

$$\underline{m}_{est} = (G^T G + \theta^2 I)^{-1} G^T \underline{T} \qquad (7)$$

This solution has smaller standard errors but poorer resolution than the generalized inverse as discussed in Paper 1. In particular, r_{ij} is no longer zero for blocks in different layers. This will introduce vertical smoothing between blocks in different layers which in turn introduce distortion in the solution as the smoothing kernels varies from block to block. Both solutions have been calculated for LASA and will be presented in the next section.

Finally, let us discuss possible shortcomings and biases in our earth-modelling approach and consequently in the estimated velocity perturbation solution. As ray-theory is used for computing the travel time through the initial model (see Fig. 1), it is implicit that the inhomogeneities are smooth within a wavelength. On the other hand, possible

inhomogeneities with scale length much shorter than the wavelength will behave as an equivalent homogeneous body with some average properties. Thus, it is meaningless to make the block size much smaller than a wavelength. Our block size of 20 km, however, is determined primarily by the station density. Ideally, we would like to divide the whole earth into blocks, but the finite amount of data available imposes limits to the number of blocks and volume of the earth to be included in our model. Because of this limitation, the effect of possible deeper inhomogeneities may be projected into our model thus biasing the final results. Besides using many events having a reasonable azimuth-distance coverage, two quantitative measures for checking such biases are discussed in Paper 1. First, extending our model from 4 to 5 layers does not significantly change the velocity perturbations in the 4 uppermost layers; secondly the model explains about 85% of the variance in the observed travel time residuals, and the remaining, unexplained variance is comparable to the variance of reading error.

Inversion of LASA P-wave Residuals

The LASA array in Montana consists of 21 subarrays and its configuration is shown in Figure 2. Travel time residuals of short period P-waves at the subarray centers (with respect to Herrin tables) for a large number of teleseismic events

have been tabulated by Chiburis and Ahner (1973). This data set, used as station corrections for beam steering during routine array processing, is based on carefully analyzed events and the measurement errors are considered to be less than 0.1 sec. Moreover, the above events have an adequate azimuthal and distance coverage (see figure 3) so these observations are well suited for our inversion experiment. The LASA data used comprises 178 events recorded at 17 subarrays giving a total of 3026 readings. The 4 F-ring seismometers were excluded from analysis due to their relatively large separation from the other stations. Examples of observed travel time residuals are listed in Table 1. The initial model parameters for the crust and upper mantle beneath LASA are given in Table 2, and is based on the results of Warren et al., (1973) and Toksöz et al. (1967). Each of the five layers of the initial model is divided into 9 x 9 square blocks with side length 20 km.

We shall present both the generalized and stochastic inverse solutions. This dual presentation of our results is preferred to a single optimal solution based on the trade-off between resolution and standard errors as discussed by Backus and Gilbert (1970). Moreover, as the amount of data available is limited, choice of block configuration may affect the cross-sampling of the individual blocks, and consequently the final solution. One way of avoiding this effect is to average the results for say different block

configurations. This block averaging procedure was adopted for the stochastic inverse solution, but not for the generalized inverse in order to maintain the best possible resolution.

The generalized inverse solution is given in Figures 4-8 and also tabulated together with estimated standard errors in Table 3. The velocity perturbations are expressed in percentage of average layer velocity (given in Table 2), and relatively high (H) and low (L) velocities are given negative and positive signs respectively. Shaded blocks represent significantly high and low velocity areas with the magnitude of velocity perturbations exceeding twice the corresponding standard errors. All but five of the sampled blocks are perfectly resolved in the generalized inverse solution except for the uncertainty of an additive constant for each layer as discussed in the preceeding section. For all blocks except the 5 encircled in Figures 4-8, the elements of the calculated resolution matrix are in accordance with Equation (3), demonstrating that the resolution is the best possible. The numerical values of the diagonal elements were 0.96-0.99 and the off-diagonal elements were ÷(0.01-0.04). Elements corresponding to combinations of blocks in different layers were zero. The part of the resolution matrix corresponding to the 5 blocks not perfectly resolved, is listed in Table 4: the overall fit of the generalized inverse solution to the observational data is excellent. The standard deviation of the residuals is 0.08 sec

which is comparable to the measurement error. The estimate of the lower limit of the root mean square of the true velocity perturbations is 3.2% under LASA as compared to 3.4% under NORSAR.

The stochastic inverse was calculated, with the damping factor $\theta^2 = 0.02$ (sec per %)^2, for two sets of block configurations, which were identical except for the shift in the NE-SW directions by a half block size. This value of θ^2 is 125 times greater than the smallest non-zero eigenvalue of 0.00016. Out of the total 271 non-zero eigenvalues, 104 are smaller than θ^2. This gives a rough idea about the resolution and standard errors in the stochastic inverse solution through Equation (49) and (50) in Paper 1. The final solution was obtained by the averaging over four partly overlapping blocks, i.e. two from the 'unshifted' solution and two from the 'shifted' solution. The averaged value is plotted at the center of gravity of the four blocks and subsequently interpolated anomaly contours at 1% intervals are drawn as shown in Figs. 9-13.

An example of the resolution matrix for the stochastic inverse is shown in Fig. 14. On the extreme left, there are five tic-tac-toe meshes corresponding to the five layers of our model. The center of each mesh corresponds to the block at a geographic location "A" shown in the map at the right hand of the same figure. These five meshes show elements of the row vector of the resolution matrix, for which the diagonal element

corresponds to the block in Layer 1 at geographic location "A". The figure shows that the diagonal element is 84%, and the element corresponding to the blocks in the same layer as the diagonal element show small negative values as also observed in the case of the generalized inverse solution. The elements for blocks immediately below the diagonal element block exhibit a small positive value of 5% indicating a slight vertical smoothing for block "A" of Layer 1. The elements not shown in the figure are all less than 1%. Figure 14 also shows elements of the resolution matrix for four other blocks with geographic locations indicated by alphabetic letters and depth indicated by layer number. Notice that the resolution is very good for the central blocks (except for Layer 5) but may be poor for spherical blocks as demonstrated in Table 5. In the latter case vertical smoothing effects are significant.

Interpretation of 3-dimensional seismic velocity anomalies under LASA

The seismic network of LASA is located in the transition zone between the Rocky Mountains and the Great Plains. Since the Rocky Mountains trend roughly N-S, one might expect a gradual change of the crust and upper mantle in the E-W direction. Our results, however, demcnstrate that changes are neither gradual nor trending in the E-W direction.

Before describing the velocity anomalies presented in the previous section, we shall summarize available geological and geophysical data pertinent to the area. The LASA siting area

is covered by undisturbed sediments of thickness about 3 km lying conformably on Precambrian basement rocks (Brown and Poort, 1965). The isopach lines for the depth to basement trend roughly NW-SE, increasing toward east. Glover and Alexander (1969) suggested the same trend for deeper structure using limited data on Rayleigh wave dispersion and spectral ratio for long period P waves, but they also recognized the NE-SW trend dominant in the travel time and amplitude anomalies of short period P waves. The spectral ratio method was used in analysis of LASA data also by Bakun (1971) whose results showed a local NE-SW trend near the array center and a regional NW-SE trend. Engdahl and Felix (1971) convincingly demonstrated that the main source of the travel time anomalies lie in the crust and upper mantle beneath the array by showing that practically identical anomaly patterns prevail for waves having greatly different paths through the deep interior of the earth but sharing nearly common ray paths near the array.

In an early attempt to explain the travel time residuals, Greenfield and Sheppard (1969) proposed a model, in which the crust thickens sharply from 58 to 70 km toward NW near the center of array. This two-dimensional model is trending N60°E, and the crust is thinning gradually both toward N30°W and S30°E and away from the center of array. A similar model was postulated by Larner (1970), who applied the wave-theoretical method of Aki and Larner (1970) for LASA structural analysis based on the short

period P-wave travel time and amplitude observations. Using additional travel time data from the extended U.S. Geological Survey array, Iyer and Healy (1972) presented a detailed map of the crustal thickness under LASA. Their result essentially agrees with Larner's i.e., the crust has a maximum thickness of 56 km under the array center but is thinning to about 40 km both to the north and to the south.

The E-NE trending crustal structure variation under LASA has gained support from numerous seismic refraction and wide angle reflection studies, summarized by Warren et al. (1973). Both the P_n time term and the P_MP time showed crustal thickening under the LASA center having a synclinal form and trending in the E-NE direction, although the crustal thickness estimated from the Pn data was not contourable because of large fluctuations. The P_MP results gave 2 to 4 km crustal thinning toward north and 4 to 6 km thinning toward south from the array center within the area under our reduced LASA aperture (F-ring omitted).

Other models, less conventional than the postulated Moho-undulations have also been tested using LASA data. For example, Mack (1969) explained the P wave-form at individual stations as a superposition of multiples caused by multi-pathing due to inhomogeneities under the array, although a complete physical structure which explains the whole data set simultaneously was not forwarded. On the other hand, using both amplitude and phase-delay fluctuation at various frequencies, Aki (1973) and Capon (1974) successfully characterized the lithosphere under the LASA as a Chernov (1960) random medium with correlation

distance 10 to 12 km and r.m.s. velocity fluctuations of 2 to 4%. Similar results were obtained by Berteussen et al. (1975) who also found that a Chernov random medium model could explain about 60% of the variance of the observed amplitude fluctuations. These results are in good harmony with our estimate of the lower limit of true velocity fluctuation of 3.2% obtained in the preceding section.

Let us now describe our result using the dual presentation of the generalized inverse and stochastic inverse. Both solutions for Layer 1, the upper crust, show a low-velocity anomaly (Figs. 4 and 9) to the north of the center subarray AO and trending roughly N60°E. It coincides well with the low gravity anomaly shown in Fig. 2. There is no known geologic feature corresponding to this anomaly. Since the sediments are nearly uniform in this area (Brown and Poort, 1965), the low velocity anomaly must be confined within the basement rock. On the other hand, the high velocity anomaly to the west may be associated with a surface feature, i.e. the Porcupine dome.

The anomalies of Layer 2, the lower crust, are shown in Figs. 5 and 10. A zone of low-velocity anomaly trending N60°E is again clearly shown in the stochastic inverse solution. The same trend direction is manifested in the generalized inverse solution by a zone of significantly high velocity blocks. We

notice that the magnitude of velocity perturbation for the generalized inverse solution is remarkably small except for peripheral blocks. It is interesting to recall that the lower crust under NORSAR was also smooth as compared to the upper crust or the uppermost mantle (Paper 1).

The N60°E trend of anomaly pattern in the crust persists to the upper mantle to the depth of 110 km as shown in the velocity anomalies of Layer 3 and 4 (Figs. 6, 7, 11, and 12). In all these solutions, the southeast part of the area shows high velocity. The boundary between the zone of significantly high and the zone of significantly low blocks in the generalized inverse solution (Figs. 6 and 7) agrees well with the E to NE striking zero contours of the stochastic inverse solution (Figs. 11 and 12). Differences between the two solutions are most pronounced in the NW corner of the area sampled where the generalized inverse solution continues to be low while the stochastic inverse solution exhibits a moderately high-velocity anomaly for both Layer 3 and 4. The anomaly contour pattern obtained for the stochastic inverse is very similar to the map of crustal thickness given by Iyer and Healy (1972).

The generalized inverse and stochastic inverse gave essentially the same results for Layer 5 except for the NW corner. In addition to the E to NE anomaly trend still persisting in the eastern part of the LASA siting area, we find a secondary trend to the

N to NW in the western area. This pattern may be recognized, though vaguely, in Iyer and Healy's "second order residual" projected to a depth of 125 km.

The most conspicuous feature of the estimated velocity anomalies under LASA is the N60°E trend which persists from the upper crust to a depth greater than 100 km. This result cannot be due to the vertical smoothing, because the inter-layer resolution was perfect for the generalized inverse, and very good for the stochastic inverse. In order to obtain a coherent vertical image of the anomalies presented, vertical cross-sections of the two solutions were constructed along a profile, indicated by a dashed line in Fig. 2, roughly perpendicular to the dominant trend direction N60°E and is depicted in Figs. 15 and 16. In both cases, we see high velocity to SE and low velocity to NW with the boundary steeply dipping toward SE. In the stochastic inverse, it looks as if a sheet of low velocity zone is sandwiched between two high-velocity regions. On the other hand, the low velocity zone of the generalized inverse solution is horizontally broader, and does not appear to be a continuous sheet across the Moho.

In any case, it is well established that the same trend in the velocity anomalies persists over nearly the entire thickness of the lithosphere with the lateral scale-length of

50 to 70 km. The maximum velocity contrast is about 4% for the stochastic inverse solution and about 10% for the generalized inverse. Considering the smoothing effect of the former, and larger random errors of the latter, the true velocity contrast probably lies between the above two values.

What is the cause of this giant anomaly trending N60°E? The change in Moho elevation proposed in earlier works can at best account for the anomalies in Layer 2 and 3. The Moho topography obtained in earlier works is likely to be over-estimated, because their model formulation projects the effect of inhomogeneities other than Moho topography into the final solution. This will introduce a strong bias because the upper-crust and the lower lithosphere seem to share the same anomaly pattern as the proposed Moho topography. The sharp change in crustal thickness (10 km within the horizontal distance of 50 km) proposed in earlier studies is indeed drastic. It is also very puzzling, because it is not reflected at all in the surface geology nor in the gravity anomalies. Whatever causes the anomaly, the trend of N60°E should give the clue. In Fig. 2 we notice that the trends of Weldon and Brockton faults are close to N60°E (Brown and Poort, 1965), and according to Stone (1965) represents a dextral wrench fault belonging to the system of wrench faults prevailing throughout the Rocky Mountains being caused by compression in the NEE-SWW direction. Brinkworth and

Kleinkopf (1972) show some correlation between the strike of wrench faults and the trend of Bouguer gravity anomaly as shown in Fig. 2. Since the NEE-SWW compression is consistent with the two major orogenies in the western U.S.; the Nevadan orogeny (Late Jurassic-Early Cretaceous) and the Laramide orogeny (Upper Cretaceous to Tertiary) we are tempted to associate the N60°E trending velocity anomaly with shearing caused by the orogenies. The shear may be concentrated in a zone of weakness which in turn causes a broad low velocity anomaly throughout the lithosphere.

Summary

We have used the novel inversion approach of Aki et al., 1975 in combination with LASA P wave residuals for teleseismic events to estimate the three-dimensional seismic velocity anomalies in the lithosphere to a depth of 140 km beneath the array. The fit to the observations is excellent as indicated by the final residuals being comparable to the measurement errors. Preference was given to a dual presentation of the generalized and stochastic inverse solution for the estimated velocity anomalies, because this facilitates the geological interpretation, and at the same time gives the reader greater freedom in judging the results than a single 'optimal' solution. The most conspicuous feature of the seismic structure under LASA is a low velocity anomaly

in the central and NE part of the array siting area with a N60°E trend and persisting from the upper crust to depths greater than 100 km. We are tempted to associate this low velocity zone with wrench faulting and shearing during the Nevadan and Laramide orogenies. The sharp change in crustal thickness proposed in earlier studies is likely to be significantly overestimated because the upper crust and the lower lithosphere appear to share the same anomaly pattern as the proposed Moho topography.

Our results also show that the velocity fluctuations are of the same order in the crust as in the upper mantle to a depth of 140 km. The root-mean-square of the true velocity fluctuations in the lithosphere under LASA is at least 3.2% and thus in agreement with similar estimates of ca 2% based on the Chernov random medium model.

ACKNOWLEDGEMENT

This work was supported by the Advanced Projects Research Agency monitored by the Air Force Office of Scientific Research through contracts F44620-75-C-0064 and F08606-74-C-0049; by the National Science Foundation under grant DES74-22025; and by the Royal Norwegian Council for Scientific and Industrial Research.

Portions of this research were carried out while one of us (A.C.) was visiting staff member at Lincoln Laboratory, M.I.T., and supported by the Advanced Research Projects Agency of the Department of Defense.

References

Aki, K. (1973). Scattering of P waves under the Montana LASA, J. Geophys. Res., 78, 1334-1346.

Aki, K., A. Christoffersson and E.S. Husebye (1975). Determination of the three-dimensional seismic structure of the lithosphere, J. Geophys. Res. in press.

Aki, K. and K.L. Larner (1970). Surface motion of a layered medium having an irregular interface due to incident SH waves, J. Geophys. Res., 75, 933-954.

Bachus, G. and F. Gilbert (1968). The resolving power of gross earth data, Geophys. J.R. astr. Soc., 16, 169-205.

Bachus, G. and F. Gilbert (1970). Uniqueness in the inversion of inaccurate gross earth data, Roy. Soc. London Philos. Trans., Sec. A., 266, 123-192.

Bakun, W.H. (1971). Crustal structure beneath LASA from long-period P-wave spectra. Seismic Discrimination - Semiannual Tech. Summary, 30 June 1971, Lincoln Lab., Mass. Inst. Tech., Cambridge, Mass.

Bertussen, K.A., A. Christoffersson, E.S. Husebye and A. Dahle (1975). Wave scattering theory in analysis of P wave anomalies at NORSAR and LASA, Geophys. J.R. astr. Soc., in press.

Brinkwort, G.L. and M.D. Kleinkopf (1972). Bouguer gravity, in 'Geologic Atlas of the Rocky Mountain Region', Rocky Mountain Association of Geologists, Denver, Colorado.

Brown, T.G. and J.M. Poort (1965). Subsurface studies and shallow-hole preparation, LASA area, eastern Montana, Tech. Rep. 65-21, Geotech Corp., Garland, Texas.

Capon, J. (1974). Characterization of crust and upper mantle structure under LASA as a random medium, Bull. Seism. Soc. Am., 64, 235-266.

Chernov, L. (1960) Wave propagation in a random medium, McGraw-Hill Book Co., New York.

Chiburis, E.F. and R.O. Ahner (1973). LASA regional travel-time corrections and associated nodes, SDAC Technical Report No. 73-6, AD 774 458, Teledyne Geotech, Alexandria, Virginia.

Davies, D. and R.M. Sheppard (1972). Lateral heterogeneity in the earth's mantle, Nature, 239, 318-323.

Engdahl, E.R and C.P. Felix (1971). Nature of travel-time anomalies at LASA, J. Geophys. Res., 76, 2706-2715.

Franklin, J.N. (1970). Well-posed stochastic extensions of ill-posed linear problems, J. Math. Anal. Appl., 31, 682-716.

Greenfield, R.J. and R.M. Sheppard (1969). The Moho depth variation under the LASA and their effect on $dT/d\Delta$ measurements, Bull. Seism. Soc. Am., 59, 409-420.

Iyer, H.M. and J.H. Healy (1972). Teleseismic residuals at the LASA-USGS extended array and their interpretation in terms of crust and upper mantle structure, J. Geophys. Res., 77. 1503-1527.

Lanczos, C. (1961) Linear differential operators, Chap. 3, Van Nostrand, New York.

Larner, K.L. (1970). Near-receiver scattering of teleseismic body waves in layered crust-mantle models having irregular interfaces, Ph.D. Thesis, Mass. Inst. of Technology, Cambridge, Mass.

Mack, H. (1969). Nature of short-period P wave signal variations at LASA, J. Geophys. Res., 74, 3161-3170.

Stone, D.S. (1965). Wrench faulting and Rocky Mountain tectonics, Mountain Geologist, 6, 67-79.

Toksöz, M.N., M.A. Chinnery and D.L. Anderson (1967). Inhomogeneities in the earth's mantle, Geophys. J.R. astr. Soc., 13, 31-59.

Warren, D.H., J.H. Healy, J. Bohn and P.A. Marshall (1973). Crustal structure under LASA from seismic refraction measurements, J. Geophys. Res., 78, 8721-8734.

Table 1. Example of Observed Travel Time Residuals (unit sec 100)
Notice that the F-ring subarrays are excluded from analysis.

Distance	Azimuth	Region	LASA SUBARRAYS																		
			A0	B1	B2	B3	B4	C1	C2	C3	C4	D1	D2	D3	D4	E1	E2	E3	E4	F1	F2	F3	F4
60	6	Novaya Zemlya	0	-7	-4	-3	2	-3	10	-5	-5	-5	-12	-18	-8	-7	-30	-7	-31	-40	-59	-54	-57
84	39	Greece	0	-2	-23	6	9	4	-31	-27	13	-15	-55	-6	4	-2	-43	-54	-28	-25	-66	-60	-46
38	68	Newfoundland	0	-3	-14	-3	13	2	-8	-29	23	-11	-28	-19	16	-9	-7	-41	-31	30	-48	-60	-21
60	102	Atlantic	0	3	-12	-1	18	28	-8	-22	32	28	-32	2	52	32	-10	-45	23	24	-44	-65	-19
39	148	Nicaragua	0	-2	5	3	8	8	3	5	14	3	-5	17	47	45	-7	-10	26	69	5	-26	35
86	179	S. Pacific	0	1	-15	-3	24	23	-14	-11	24	11	-22	-8	39	33	-48	-25	23	0	-37	-62	-25
74	211	Tacamoto Archip.	0	-3	-16	-3	34	37	-10	-11	27	12	-26	-15	59	51	-30	-46	51	81	-47	-25	15
93	248	Fiji	0	-3	-19	-2	5	-1	-26	-16	4	-4	-39	-15	-20	-27	-42	-32	-5	-6	-59	-16	-71
50	296	W. Marian Is.	0	-9	-2	-5	-9	-15	-11	-9	-13	-12	-30	-27	-17	0	-8	-49	-18	8	-41	-45	-31
88	328	N.E. China	0	-6	3	6	-11	-8	3	5	-9	7	-2	-16	-6	-3	10	-15	-21	12	9	7	-70

Table 2. Initial Model Parameters for Crust and Upper Mantle Beneath LASA.

Layer	Thickness (km)	P-Velocity (km/sec)	Lateral Block Size (km)
1	20	6.0	20
2	30	6.7	20
3	30	8.0	20
4	30	8.2	20
5	30	8.2	20

Table 3a. Layer 1 tabulation of estimated generalized inverse velocity perturbations in per cent of average layer velocity and the corresponding standard errors for the blocks sampled. Negative and positive signs indicate relatively high and low velocity anomalies respectively. The upper left block corresponds to the NW corner of the grid, while the center subarray block is squared. Initial model parameters for Layer 1 are listed in Table 2.

—	—	—	—	—	—	—	—	—
—	—	—	—	-5.4 (1.5)	-0.2 (0.9)	—	—	—
—	—	—	1.5 (0.8)	-0.7 (1.1)	5.1 (1.0)	—	—	—
—	-2.7 (1.5)	-13.8 (1.8)	1.8 (0.6)	2.2 (0.4)	2.8 (0.5)	1.6 (2.8)	—	—
—	-4.6 (1.1)	-8.8 (1.1)	2.0 (0.4)	1.4 (0.4)	1.5 (0.4)	—	—	—
—	—	—	-1.0 (0.4)	-0.2 (0.4)	0.2 (0.5)	—	7.5 (1.4)	7.0 (1.6)
—	—	—	—	—	—	—	—	—
—	—	—	1.0 (1.4)	1.6 (1.2)	—	—	—	—
—	—	—	—	—	—	—	—	—

Table 3b. Layer 2 tabulation of estimated generalized inverse velocity perturbations. The unresolved block is in brackets. Otherwise caption as for Table 3a.

—	—	—	—	2.8 (1.9)	-0.9 (2.0)	—	—	—
—	—	—	—	-0.8 (0.9)	1.6 (0.9)	0.1 (1.3)	—	—
—	—	—	0.1 (0.7)	0.4 (0.5)	-0.5 (0.5)	1.7 (1.1)	—	—
—	-1.9 (1.4)	0.3 (1.1)	-0.3 (0.4)	0.8 (0.3)	-0.3 (0.4)	-1.0 (0.6)	—	—
—	5.7 (1.5)	1.5 (0.6)	0.5 (0.4)	[0.4 (0.3)]	-0.9 (0.3)	-0.9 (0.4)	-3.4 (0.8)	1.0 (1.3)
—	—	0.8 (1.8)	0.3 (0.5)	-1.7 (0.3)	-1.5 (0.4)	-1.3 (0.5)	-0.6 (0.9)	-1.3 (1.1)
—	—	—	-1.3 (0.7)	-0.4 (0.6)	-2.1 (0.6)	7.1 (1.5)	0.8 (1.4)	-1.3 (1.4)
—	—	—	-2.4 (1.0)	0.1 (0.8)	—	—	—	—
—	—	—	-0.2 (1.8)	-1.0 (1.0)	—	—	—	—

Table 3c. Layer 3 tabulation of estimated generalized inverse velocity perturbations. Otherwise caption as for Tables 3a and 3b.

—	—	—	7.5 (1.5)	6.2 (1.2)	1.6 (1.3)	1.9 (1.6)	—	—
—	—	1.9 (1.1)	3.8 (0.9)	3.6 (0.9)	1.1 (1.0)	0.5 (1.1)	—	—
-0.5 (1.5)	1.3 (1.3)	2.5 (0.8)	2.4 (0.5)	1.9 (0.5)	2.2 (0.5)	1.6 (0.6)	3.9 (1.7)	—
2.1 (1.4)	-2.6 (1.0)	1.5 (0.6)	3.2 (0.5)	2.9 (0.4)	2.9 (0.4)	0.9 (0.5)	5.8 (1.0)	2.9 (1.8)
-5.4 (1.7)	-3.0 (1.2)	1.7 (0.6)	3.6 (0.5)	2.9 (0.4)	0.7 (0.4)	-0.6 (0.5)	2.3 (0.8)	1.0 (1.4)
—	-3.6 (2.2)	1.9 (0.7)	0.9 (0.6)	0.6 (0.5)	-1.1 (0.4)	-1.1 (0.5)	-4.7 (2.0)	0.8 (1.7)
—	—	-1.1 (1.1)	-0.6 (0.8)	-0.1 (0.5)	-0.5 (0.5)	-2.0 (0.7)	-7.5 (1.5)	-7.2 (2.9)
—	—	—	-0.2 (1.1)	-1.8 (1.0)	-2.1 (0.8)	0.0 (1.0)	-11.6 (2.2)	-4.9 (3.5)
—	—	-1.8 (0.8)	-7.9 (2.5)	-6.5 (1.3)	-4.7 (1.3)	—	—	—

Table 3d. Layer 4 tabulation of estimated generalized inverse velocity perturbations. Otherwise caption as for Table 3a and 3b.

—	2.1 (1.4)	1.7 (1.1)	-0.3 (1.0)	2.8 (1.1)	3.5 (1.2)	2.7 (1.2)	0.8 (1.8)	0.1 (1.2)
5.0 (1.8)	1.5 (1.0)	2.5 (0.8)	2.2 (0.7)	2.9 (0.8)	2.9 (0.8)	2.2 (0.8)	-0.6 (1.1)	-5.2 (2.3)
7.5 (1.4)	0.8 (0.8)	2.1 (0.6)	0.6 (0.5)	0.8 (0.5)	1.6 (0.6)	1.4 (0.6)	1.4 (0.8)	-3.6 (1.6)
6.3 (1.2)	1.3 (0.8)	1.8 (0.6)	1.7 (0.5)	2.3 (0.5)	0.5 (0.5)	0.7 (0.6)	1.4 (0.7)	-4.2 (1.2)
8.3 (2.4)	3.5 (1.4)	2.2 (0.7)	2.6 (0.5)	2.6 (0.6)	1.4 (0.6)	-1.4 (0.5)	-3.1 (0.7)	-5.2 (1.1)
13.3 (3.9)	0.7 (1.3)	1.6 (0.7)	0.0 (0.6)	-0.1 (0.6)	-1.0 (0.5)	-2.2 (0.6)	-3.4 (0.7)	-11.0 (1.4)
1.4 (4.3)	1.3 (2.6)	0.3 (0.9)	-2.0 (0.7)	-2.9 (0.6)	-3.5 (0.6)	-4.5 (0.6)	-4.0 (0.7)	-3.6 (2.9)
—	—	5.9 (1.9)	-1.9 (1.2)	-3.3 (0.8)	-4.2 (0.7)	-4.8 (0.7)	-5.9 (1.0)	-6.8 (2.7)
—	-1.8 (0.8)	2.9 (2.1)	-0.3 (1.8)	-2.4 (1.0)	-3.2 (0.9)	-6.4 (1.0)	-5.7 (1.8)	-4.6 (3.3)

Table 3e. Layer 5 tabulation for estimated generalized inverse velocity perturbations. Otherwise caption as for Tables 3a and 3b.

0.3 (1.2)	1.3 (0.9)	1.2 (0.9)	1.8 (0.8)	3.2 (0.9)	3.5 (0.9)	3.6 (1.0)	2.7 (1.1)	1.4 (1.5)
0.6 (0.9)	0.6 (0.8)	0.5 (0.7)	-0.3 (0.7)	4.5 (0.6)	5.2 (0.6)	4.3 (0.7)	2.2 (0.8)	2.1 (1.1)
2.1 (0.9)	0.4 (0.7)	-0.3 (0.6)	0.1 (0.6)	4.1 (0.5)	6.0 (0.6)	3.7 (0.6)	2.2 (0.7)	1.0 (0.9)
1.5 (1.1)	0.1 (0.7)	0.4 (0.6)	-1.0 (0.6)	4.0 (0.6)	3.1 (0.5)	0.1 (0.6)	1.0 (0.7)	0.2 (0.8)
2.9 (1.4)	0.8 (0.9)	0.6 (0.6)	-0.4 (0.6)	0.8 (0.7)	2.3 (0.7)	0.8 (0.6)	1.0 (0.6)	0.2 (0.8)
2.2 (1.5)	1.9 (0.9)	2.7 (0.7)	-1.3 (0.6)	-2.0 (0.8)	-0.8 (0.6)	-0.3 (0.7)	-1.8 (0.7)	-2.1 (0.8)
-1.5 (2.6)	1.8 (1.1)	0.4 (0.9)	0.5 (0.7)	-1.0 (0.7)	-3.1 (0.6)	-4.2 (0.6)	-6.1 (0.7)	-5.3 (0.8)
—	-1.9 (2.6)	-1.0 (1.8)	-2.1 (0.8)	-1.4 (0.7)	-3.1 (0.7)	-5.4 (0.7)	-6.5 (0.8)	-8.2 (1.0)
-1.8 (0.8)	—	3.5 (1.5)	-1.3 (1.2)	-0.9 (0.9)	-2.6 (0.8)	-3.9 (0.8)	-5.1 (0.9)	-7.4 (1.2)

Table 4. Part of the resolution matrix corresponding to the five unresolved blocks for the generalized inverse solution. The line marks the diagonal elements.

0.54	-	0.49	-	-
-	0.33	-	0.33	-
0.49	-	0.44	-	-
-	0.33	-	0.33	0.33
-	0.33	-	0.33	0.33

Table 5a. Layer 1 tabulation of diagonal elements for the resolution matrix for the stochastic inverse solution. The upper left block corresponds to the NW corner of the grid, while the center subarray block is squared. Initial model parameters for Layer 1 are listed in Table 2.

—	—	—	—	—	—	—	—	—
—	—	—	—	.31	.61	—	—	—
—	—	—	.52	.29	.47	—	—	—
—	.46	.20	.65	.84	.79	.05	—	—
—	.54	.39	.78	.88	.84	—	—	—
—	—	—	.79	.81	.78	—	.61	.31
—	—	—	—	—	—	—	—	—
—	—	—	.43	.55	—	—	—	—
—	—	—	—	—	—	—	—	—

Table 5b. Layer 2 tabulation of diagonal elements for the resolution matrix for the stochastic inverse solution. Caption as for Table 5a.

—	—	—	—	.11	.10	—	—	—
—	—	—	—	.60	.60	.09	—	—
—	—	—	.64	.76	.76	.28	—	—
—	.56	.60	.85	.89	.85	.64	—	—
—	.47	.76	.87	.90	.89	.79	.66	.39
—	—	.30	.76	.89	.87	.62	.64	.60
—	—	—	.67	.66	.68	.17	.39	.45
—	—	—	.55	.65	—	—	—	—
—	—	—	.21	.57	—	—	—	—

Table 5c. Layer 3 tabulation of diagonal elements of the resolution matrix for the stochastic inverse solution. Caption as for Table 5a.

—	—	—	.36	.46	.40	.30	—	—
—	—	.41	.39	.57	.43	.40	—	—
.39	.28	.69	.77	.79	.76	.67	.27	—
.44	.47	.76	.84	.82	.83	.76	.43	.22
.27	.40	.67	.82	.83	.81	.80	.59	.44
—	.31	.67	.69	.81	.84	.79	.09	.28
—	—	.49	.60	.77	.81	.64	.30	.43
—	—	—	.43	.35	.56	.37	.13	.29
—	—	.07	.20	.49	.45	—	—	—

Table 5d. Layer 4 tabulation of diagonal elements for the resolution matrix for the stochastic inverse solution. Caption as for Table 5a.

——	.29	.41	.51	.42	.43	.39	.23	.07
.30	.54	.67	.69	.59	.59	.56	.41	.14
.43	.68	.77	.79	.76	.74	.70	.59	.30
.44	.58	.77	.78	.75	.79	.76	.68	.45
.25	.21	.63	.74	.66	.64	.76	.60	.49
.06	.49	.66	.70	.67	.78	.78	.67	.34
.07	.18	.50	.66	.69	.80	.80	.63	.34
——	——	.32	.36	.57	.74	.71	.51	.41
——	.07	.22	.27	.49	.60	.49	.15	.28

Table 5e. Layer 5 tabulation of diagonal elements for the resolution matrix for the stochastic inverse solution. Caption as for Table 5a.

.51	.65	.63	.57	.55	.58	.55	.42	.33
.64	.74	.73	.68	.68	.71	.65	.59	.47
.67	.75	.76	.78	.74	.73	.68	.66	.60
.40	.61	.72	.67	.64	.71	.69	.66	.64
.43	.41	.63	.61	.44	.50	.63	.69	.55
.45	.48	.67	.64	.46	.72	.62	.70	.64
.17	.43	.51	.64	.61	.77	.78	.73	.62
——	.15	.21	.53	.67	.71	.79	.74	.59
.07	——	.38	.43	.55	.70	.72	.64	.43

Figure Captions

Figure 1. The initial layered model with constant thickness and average velocity v_{oi} is divided into many blocks. Our problem is to estimate the velocity perturbation $\underline{m}$ for each block using the P travel time data for many teleseismic events observed at the receivers above the model. The velocity perturbation $\underline{m}$ for a particular block in a particular layer represents an average over all the rays having most of the unperturbed path in the layer within the block.

Figure 2. Map of LASA subarray centers and Bouguer gravity anomalies. The dashed line marks the profile along which vertical cross-sections of velocity anomalies are shown in Figures 15 and 16.

Figure 3. Epicenter locations of the 178 events used in analysis.

Figure 4. Generalized inverse solution for Layer 1. The numbers show the fractional velocity perturbation in per cent of the average layer velocity given in Table 2. The shaded areas correspond to the magnitude of solution greater than twice the standard error which is listed in Table 3. The letters L and H refer to low and high velocity anomalies respectively. The central subarray is marked by a larger solid circle.

Figure 5. Generalized inverse solution for Layer 2. The unresolved block is encircled. See Figure 4 for explanation of symbols.

Figure 6. Generalized inverse solution for Layer 3. See Figures 4 and 5 for explanation of symbols.

Figure 7. Generalized inverse solution for Layer 4. See Figures 4 and 5 for explanation of symbols.

Figure 8. Generalized inverse solution for Layer 5. See Figures 4 and 5 for explanation of symbols.

Figure 9. Stochastic inverse solution for Layer 1. The numbers show the fractional velocity perturbation in per cent of the average velocity given in Table 2. The values represent the 4 point average over two block configurations, one centered at the central subarray (marked by a large solid circle) and the other shifted by a half-block length towards southwest. The letters L and H mark areas of low and high velocity anomalies respectively. The contours are drawn at 1% intervals.

Figure 10. Stochastic inverse solution for Layer 2. See Figure 9 for explanation of symbols.

Figure 11. Stochastic inverse solution for Layer 3. See Figure 9 for explanation of symbols.

Figure 12. Stochastic inverse solution for Layer 4. See Figure 9 for explanation of symbols.

Figure 13. Stochastic inverse solution for Layer 5. See Figure 9 for explanation of symbols.

Figure 14. Selected elements of the resolution matrix in % for the stochastic inverse solution. The diagonal elements are enclosed by thicker lines. For example, the five tic-tac-toes under A are the elements of row vector corresponding to the diagonal element in Layer 3 at geographic location "A" marked on the right. See text for detailed explanation.

Figure 15. Generalized inverse solution for the vertical cross-section along the profile indicated in Figure 2. The numbers were obtained by interpolation from those given in Figures 4 through 8. The letters H and L refer to high and low velocity anomalies respectively.

Figure 16. Stochastic inverse solution for the vertical cross-section along the profile indicated in Figure 2. The numbers are directly obtained from Figures 9 through 14. The letters H and L refer to high and low velocity anomalies respectively.

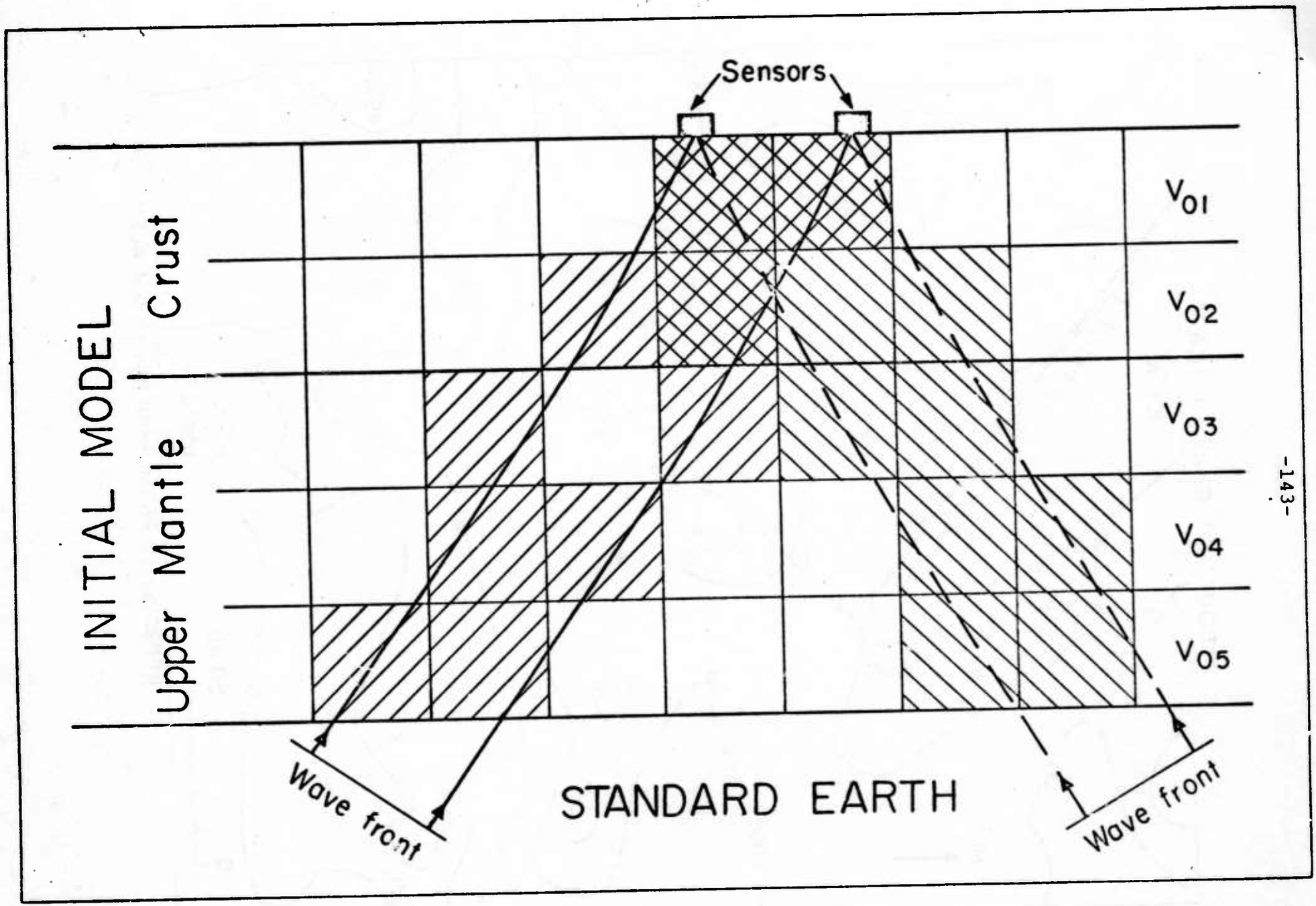
Sensors
INITIAL MODEL
Crust
Upper Mantle
V_{01}
V_{02}
V_{03}
V_{04}
V_{05}
Wave front
STANDARD EARTH
Wave front

FIG 1

BOUGUER GRAVITY (LASA)

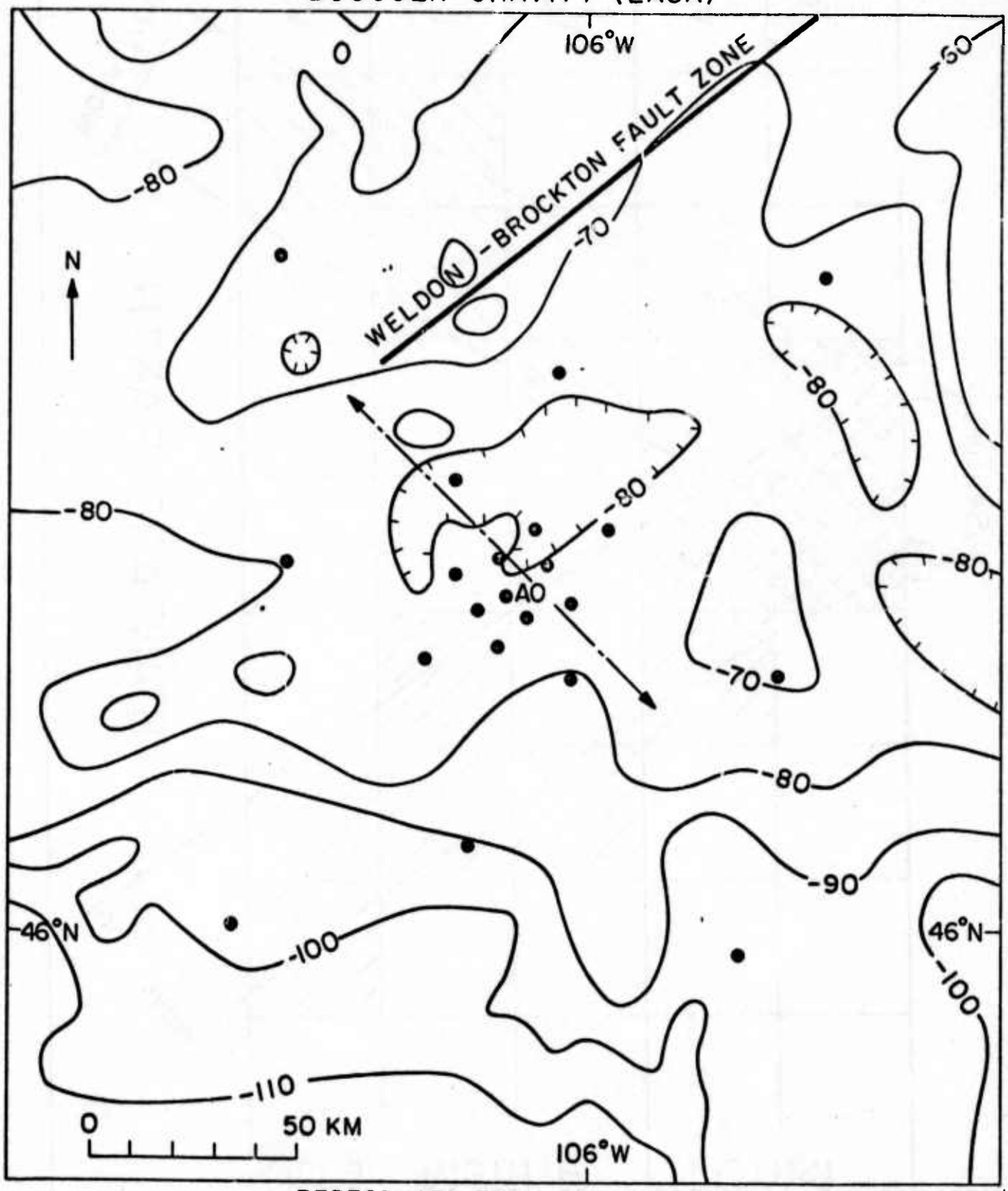

REPRODUCED FROM BRINKWORTH and KLEINKOPF (1972)

FIG 9

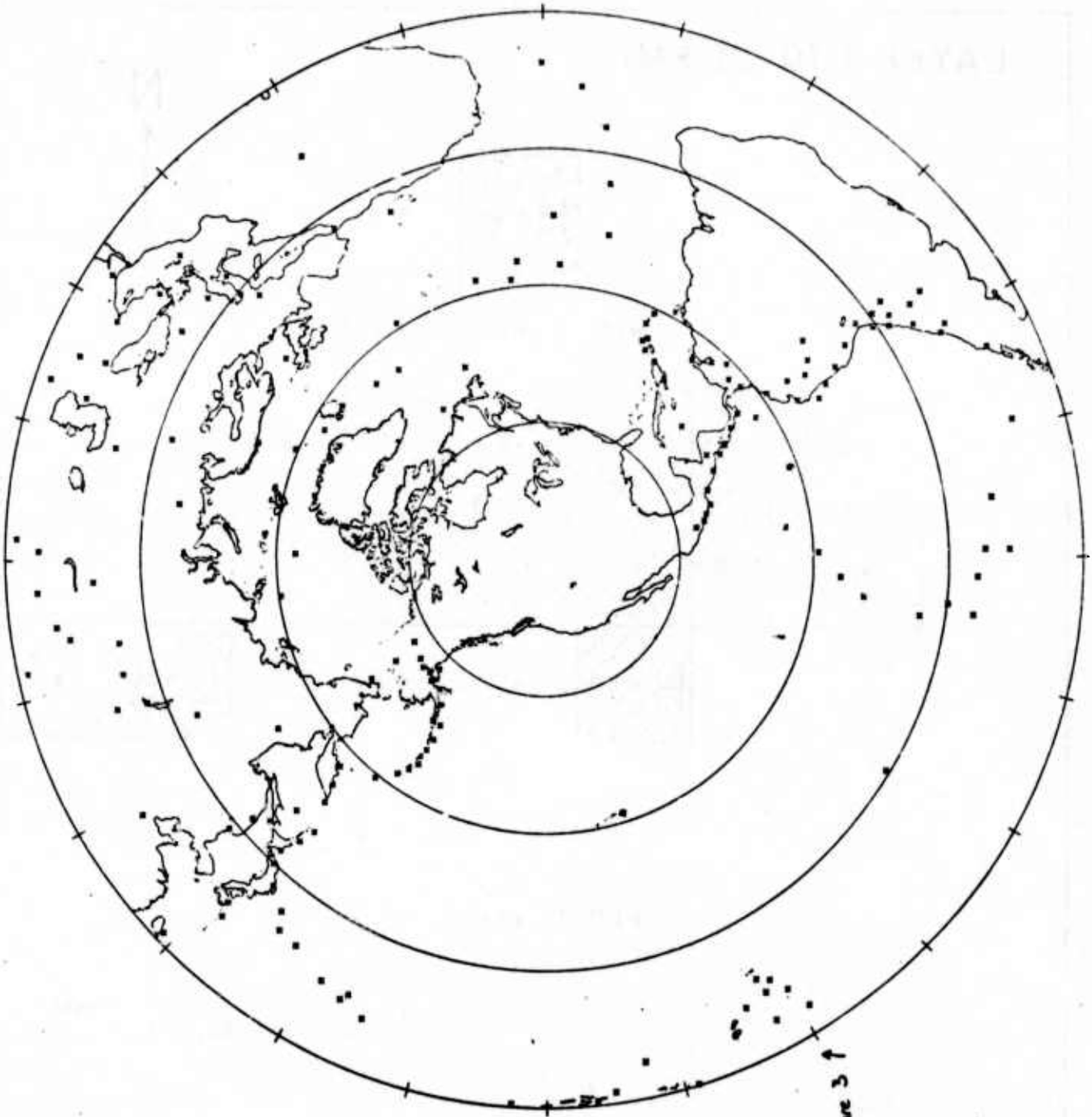

Figure 3

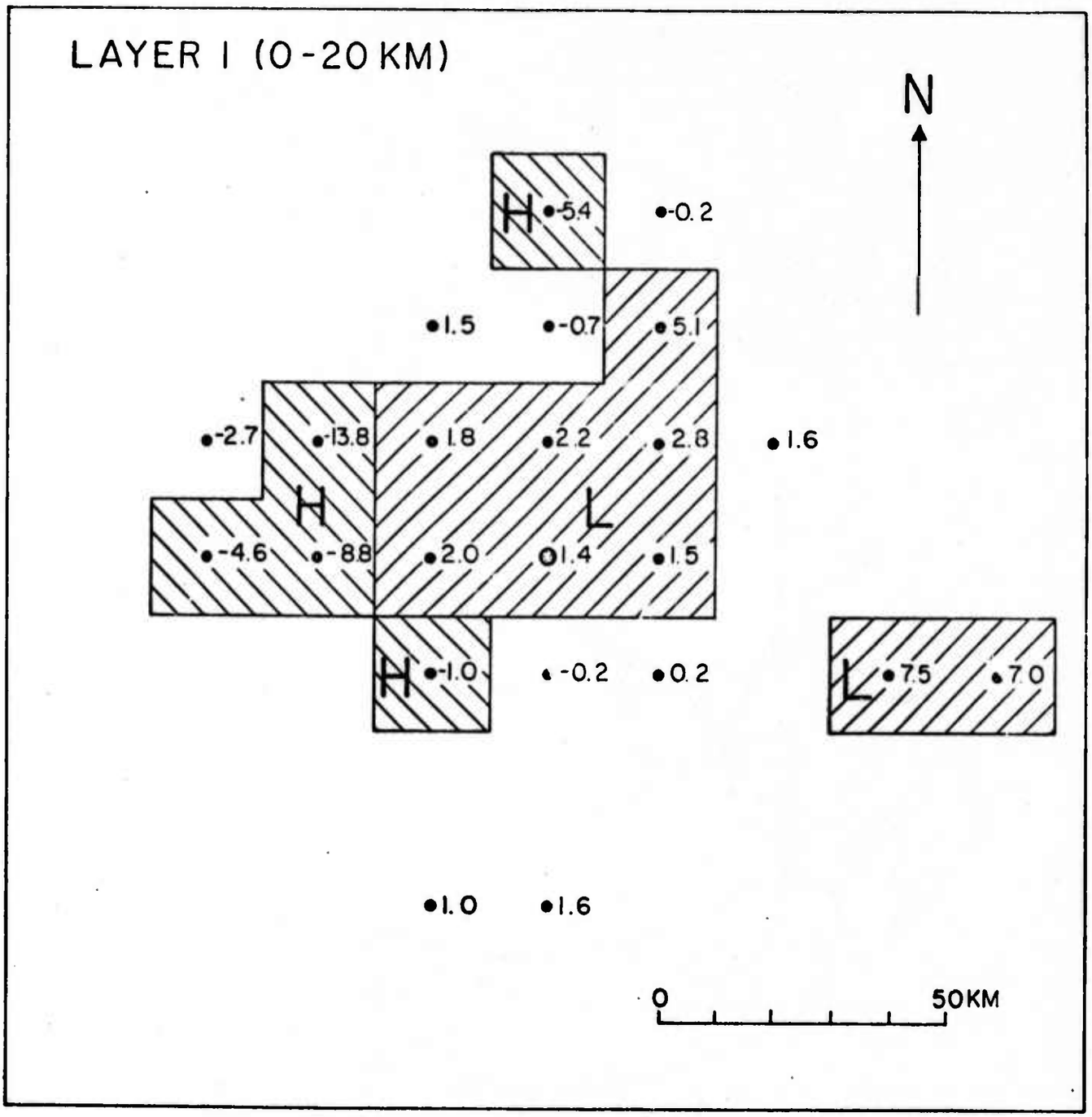
LAYER I (0-20 KM)
N
H
-5.4
-0.2
1.5
-0.7
5.1
-2.7
-13.8
1.8
2.2
2.8
1.6
H
L
-4.6
-8.8
2.0
1.4
1.5
H
-1.0
-0.2
0.2
L
7.5
7.0
1.0
1.6
0
50KM

FIG 4

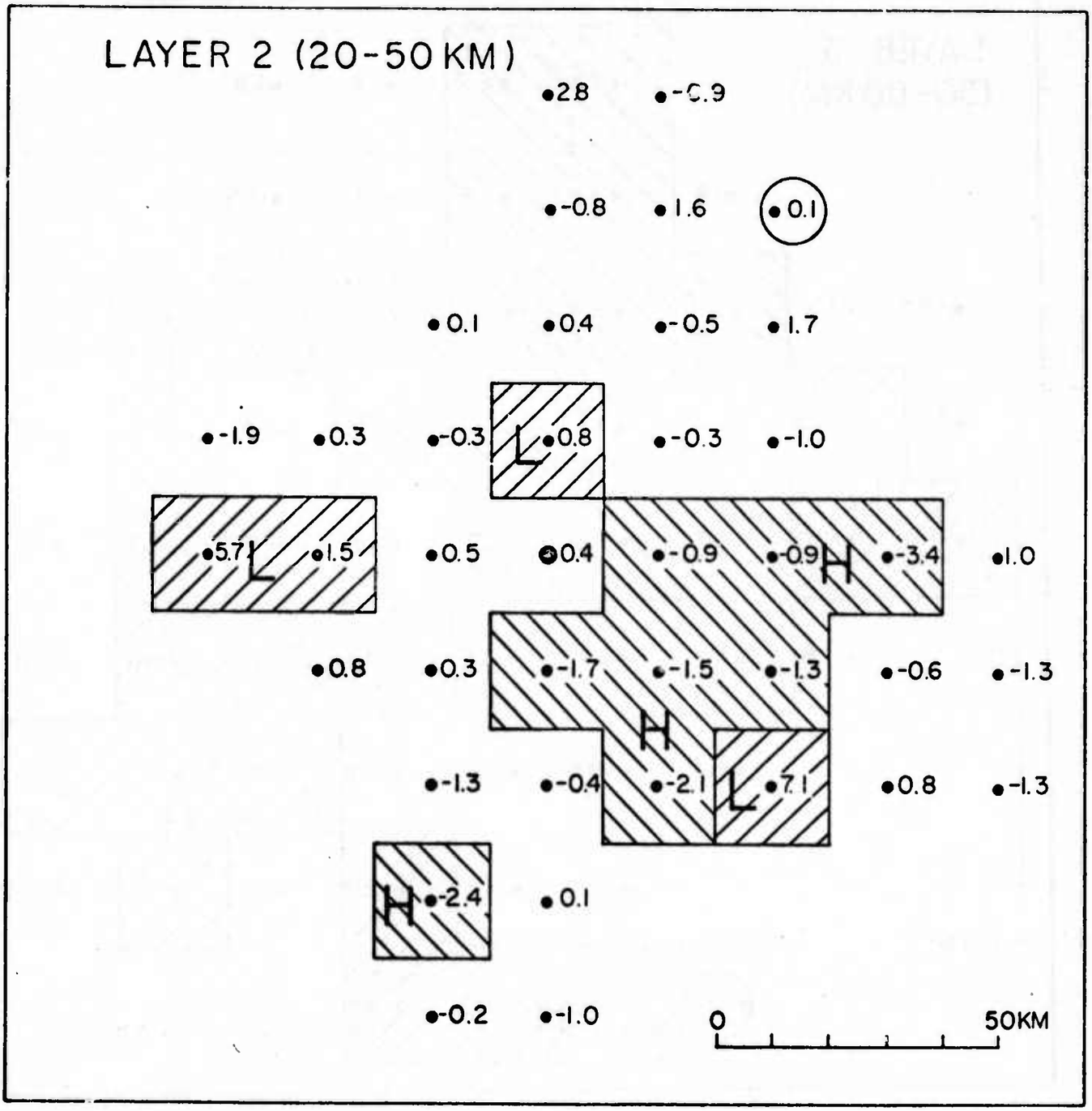
LAYER 2 (20-50 KM)
2.8
-0.9
-0.8
1.6
0.1
0.1
0.4
-0.5
1.7
-1.9
0.3
-0.3
L
0.8
-0.3
-1.0
5.7
L
1.5
0.5
0.4
-0.9
-0.9
H
-3.4
1.0
0.8
0.3
-1.7
-1.5
-1.3
-0.6
-1.3
H
-1.3
-0.4
-2.1
L
7.1
0.8
-1.3
H
-2.4
0.1
-0.2
-1.0
0
50KM

FIG 5

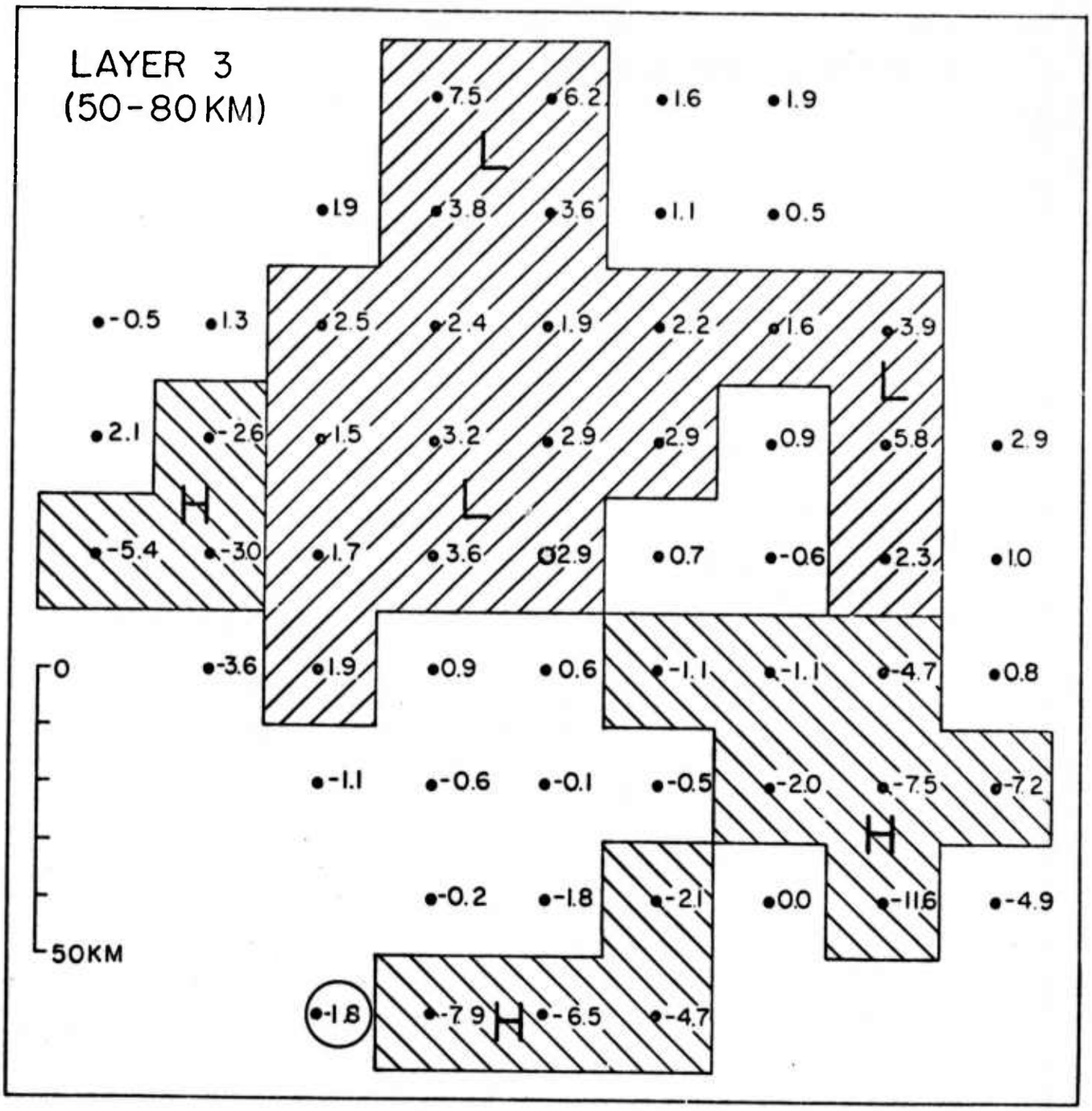
LAYER 3
(50-80 KM)
7.5
6.2
1.6
1.9
1.9
3.8
3.6
1.1
0.5
-0.5
1.3
2.5
2.4
1.9
2.2
1.6
3.9
2.1
-2.6
1.5
3.2
2.9
2.9
0.9
5.8
2.9
-5.4
-3.0
1.7
3.6
2.9
0.7
-0.6
2.3
1.0
0
-3.6
1.9
0.9
0.6
-1.1
-1.1
-4.7
0.8
-1.1
-0.6
-0.1
-0.5
-2.0
-7.5
-7.2
-0.2
-1.8
-2.1
0.0
-11.6
-4.9
50KM
-1.8
-7.9
-6.5
-4.7
L
H
L
L
H
H

FIG 6

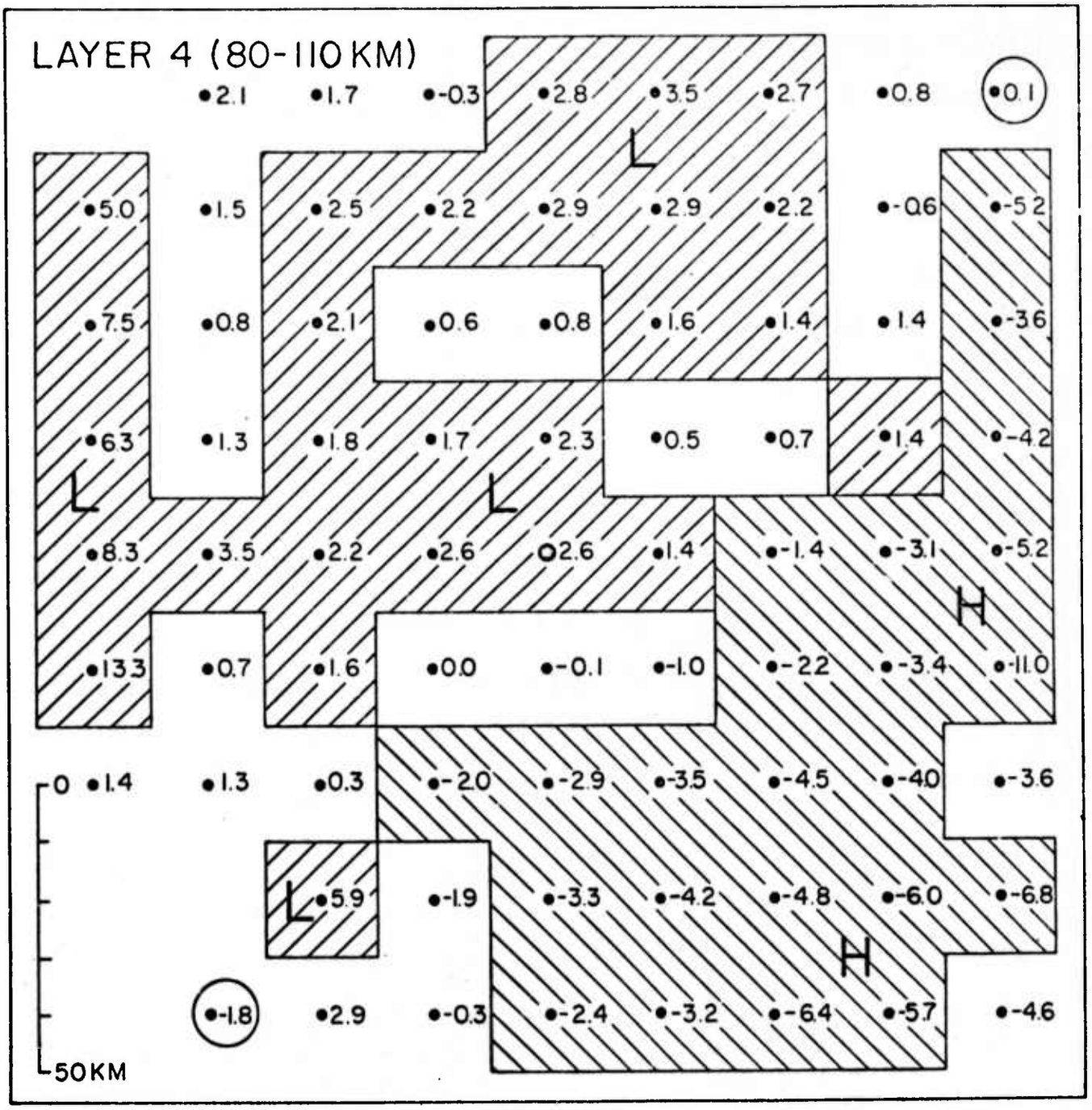
LAYER 4 (80-110 KM)
2.1 1.7 -0.3 2.8 3.5 2.7 0.8 0.1
5.0 1.5 2.5 2.2 2.9 2.9 2.2 -0.6 -5.2
7.5 0.8 2.1 0.6 0.8 1.6 1.4 1.4 -3.6
6.3 1.3 1.8 1.7 2.3 0.5 0.7 1.4 -4.2
8.3 3.5 2.2 2.6 2.6 1.4 -1.4 -3.1 -5.2
13.3 0.7 1.6 0.0 -0.1 -1.0 -2.2 -3.4 -11.0
0 1.4 1.3 0.3 -2.0 -2.9 -3.5 -4.5 -4.0 -3.6
5.9 -1.9 -3.3 -4.2 -4.8 -6.0 -6.8
-1.8 2.9 -0.3 -2.4 -3.2 -6.4 -5.7 -4.6
L
L
L
H
H
50KM

FIG 7

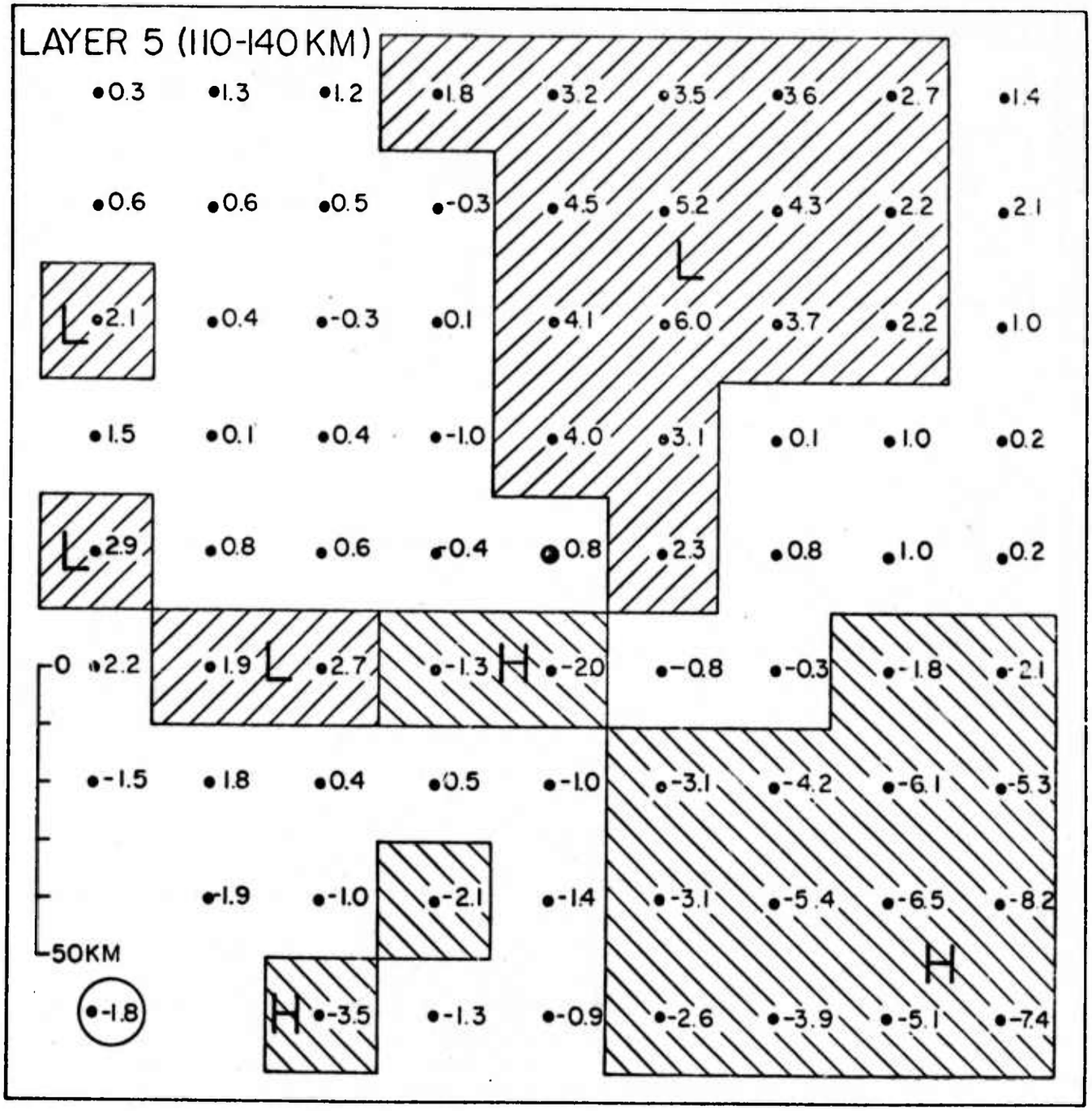
LAYER 5 (110-140 KM)
0.3 1.3 1.2 1.8 3.2 3.5 3.6 2.7 1.4
0.6 0.6 0.5 -0.3 4.5 5.2 4.3 2.2 2.1
L
2.1 0.4 -0.3 0.1 4.1 6.0 3.7 2.2 1.0
1.5 0.1 0.4 -1.0 4.0 3.1 0.1 1.0 0.2
L
2.9 0.8 0.6 0.4 0.8 2.3 0.8 1.0 0.2
0 2.2 1.9 L 2.7 -1.3 H -2.0 -0.8 -0.3 -1.8 -2.1
-1.5 1.8 0.4 0.5 -1.0 -3.1 -4.2 -6.1 -5.3
1.9 -1.0 -2.1 -1.4 -3.1 -5.4 -6.5 -8.2
50KM
H
-1.8
H -3.5 -1.3 -0.9 -2.6 -3.9 -5.1 -7.4

FIG 8

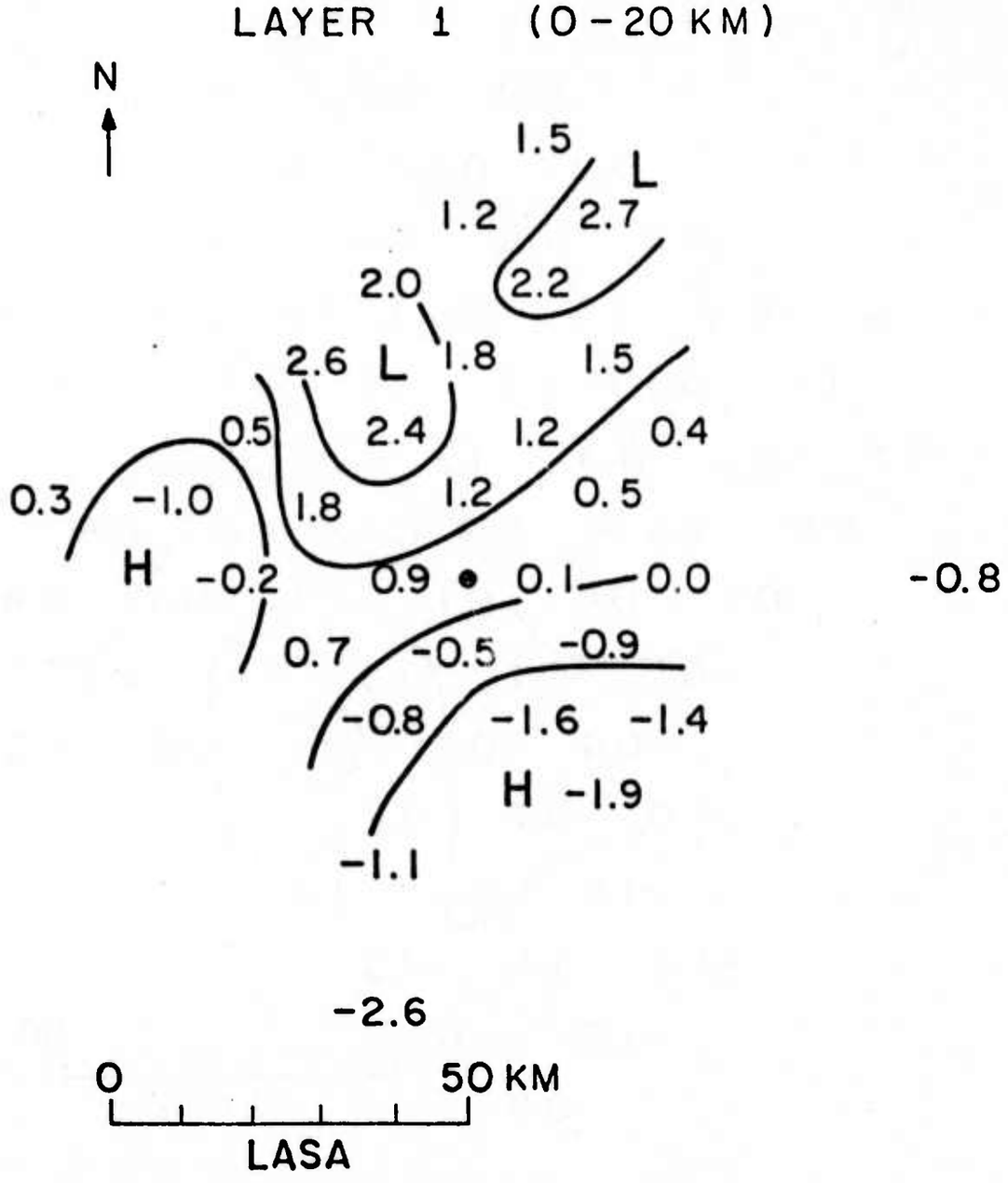
LAYER 1 (0-20 KM)
N
1.5
L
1.2
2.7
2.0
2.2
2.6
L
1.8
1.5
0.5
2.4
1.2
0.4
0.3
-1.0
1.8
1.2
0.5
H
-0.2
0.9
0.1
0.0
-0.8
0.7
-0.5
-0.9
-0.8
-1.6
-1.4
H
-1.9
-1.1
-2.6
0
50 KM
LASA

FIG 9

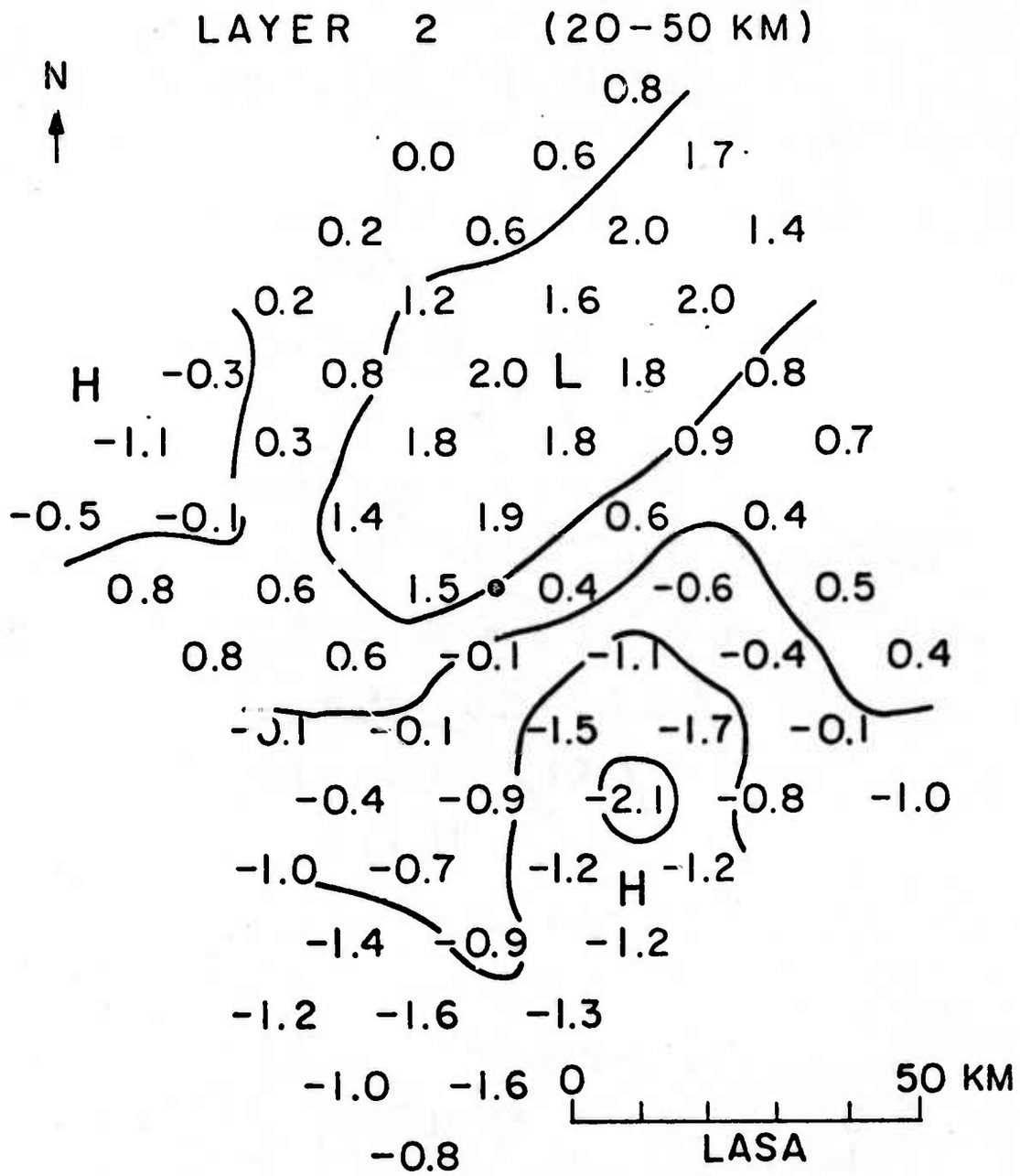
LAYER 2 (20-50 KM)
N
0.8
0.0 0.6 1.7
0.2 0.6 2.0 1.4
0.2 1.2 1.6 2.0
H -0.3 0.8 2.0 L 1.8 0.8
-1.1 0.3 1.8 1.8 0.9 0.7
-0.5 -0.1 1.4 1.9 0.6 0.4
0.8 0.6 1.5 0.4 -0.6 0.5
0.8 0.6 -0.1 -1.1 -0.4 0.4
-0.1 -0.1 -1.5 -1.7 -0.1
-0.4 -0.9 -2.1 -0.8 -1.0
-1.0 -0.7 -1.2 H -1.2
-1.4 -0.9 -1.2
-1.2 -1.6 -1.3
-1.0 -1.6
-0.8
0 50 KM
LASA

FIG 10

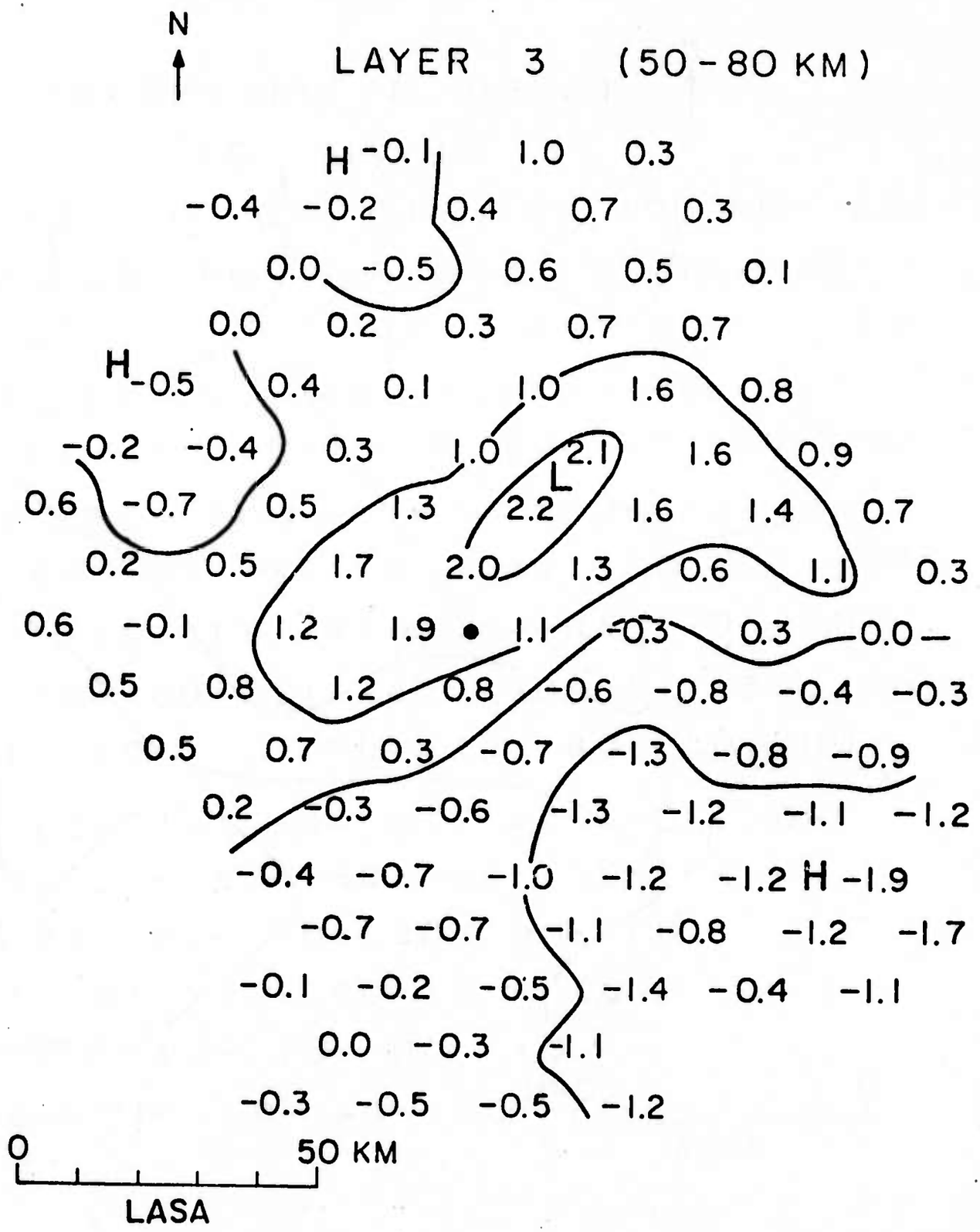
N
LAYER 3 (50-80 KM)
H -0.1 1.0 0.3
-0.4 -0.2 0.4 0.7 0.3
0.0 -0.5 0.6 0.5 0.1
0.0 0.2 0.3 0.7 0.7
H -0.5 0.4 0.1 1.0 1.6 0.8
-0.2 -0.4 0.3 1.0 2.1 1.6 0.9
L
0.6 -0.7 0.5 1.3 2.2 1.6 1.4 0.7
0.2 0.5 1.7 2.0 1.3 0.6 1.1 0.3
0.6 -0.1 1.2 1.9 1.1 -0.3 0.3 0.0
0.5 0.8 1.2 0.8 -0.6 -0.8 -0.4 -0.3
0.5 0.7 0.3 -0.7 -1.3 -0.8 -0.9
0.2 -0.3 -0.6 -1.3 -1.2 -1.1 -1.2
-0.4 -0.7 -1.0 -1.2 -1.2 H -1.9
-0.7 -0.7 -1.1 -0.8 -1.2 -1.7
-0.1 -0.2 -0.5 -1.4 -0.4 -1.1
0.0 -0.3 -1.1
-0.3 -0.5 -0.5 -1.2
0
50 KM
LASA

FIG 11

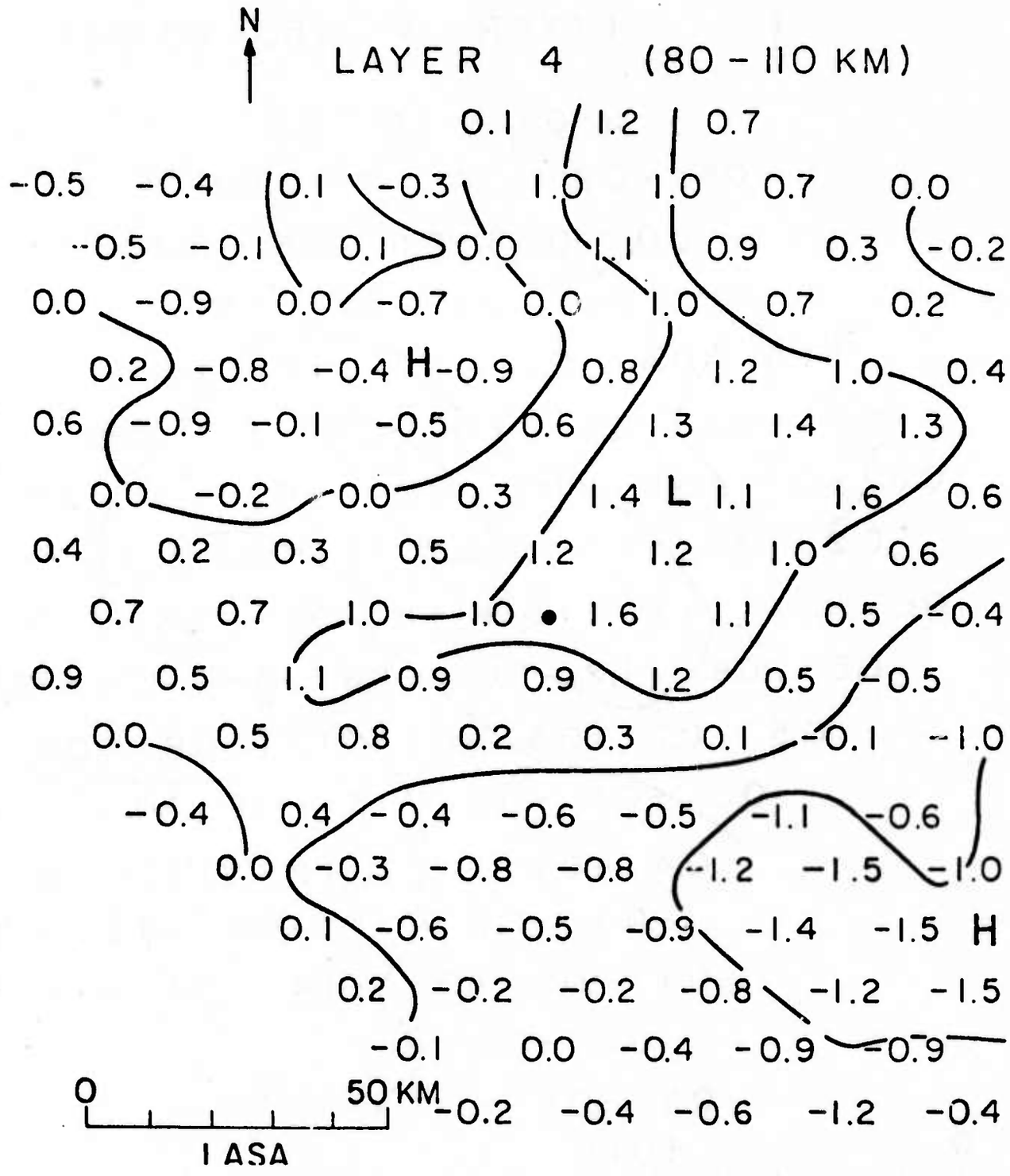
N
LAYER 4 (80 - 110 KM)
0.1 1.2 0.7
-0.5 -0.4 0.1 -0.3 1.0 1.0 0.7 0.0
-0.5 -0.1 0.1 0.0 1.1 0.9 0.3 -0.2
0.0 -0.9 0.0 -0.7 0.0 1.0 0.7 0.2
0.2 -0.8 -0.4 H -0.9 0.8 1.2 1.0 0.4
0.6 -0.9 -0.1 -0.5 0.6 1.3 1.4 1.3
0.0 -0.2 -0.0 0.3 1.4 L 1.1 1.6 0.6
0.4 0.2 0.3 0.5 1.2 1.2 1.0 0.6
0.7 0.7 1.0 1.0 1.6 1.1 0.5 -0.4
0.9 0.5 1.1 0.9 0.9 1.2 0.5 -0.5
0.0 0.5 0.8 0.2 0.3 0.1 -0.1 -1.0
-0.4 0.4 -0.4 -0.6 -0.5 -1.1 -0.6
0.0 -0.3 -0.8 -0.8 -1.2 -1.5 -1.0
0.1 -0.6 -0.5 -0.9 -1.4 -1.5 H
0.2 -0.2 -0.2 -0.8 -1.2 -1.5
-0.1 0.0 -0.4 -0.9 -0.9
0 50 KM
-0.2 -0.4 -0.6 -1.2 -0.4
1 ASA

FIG 12

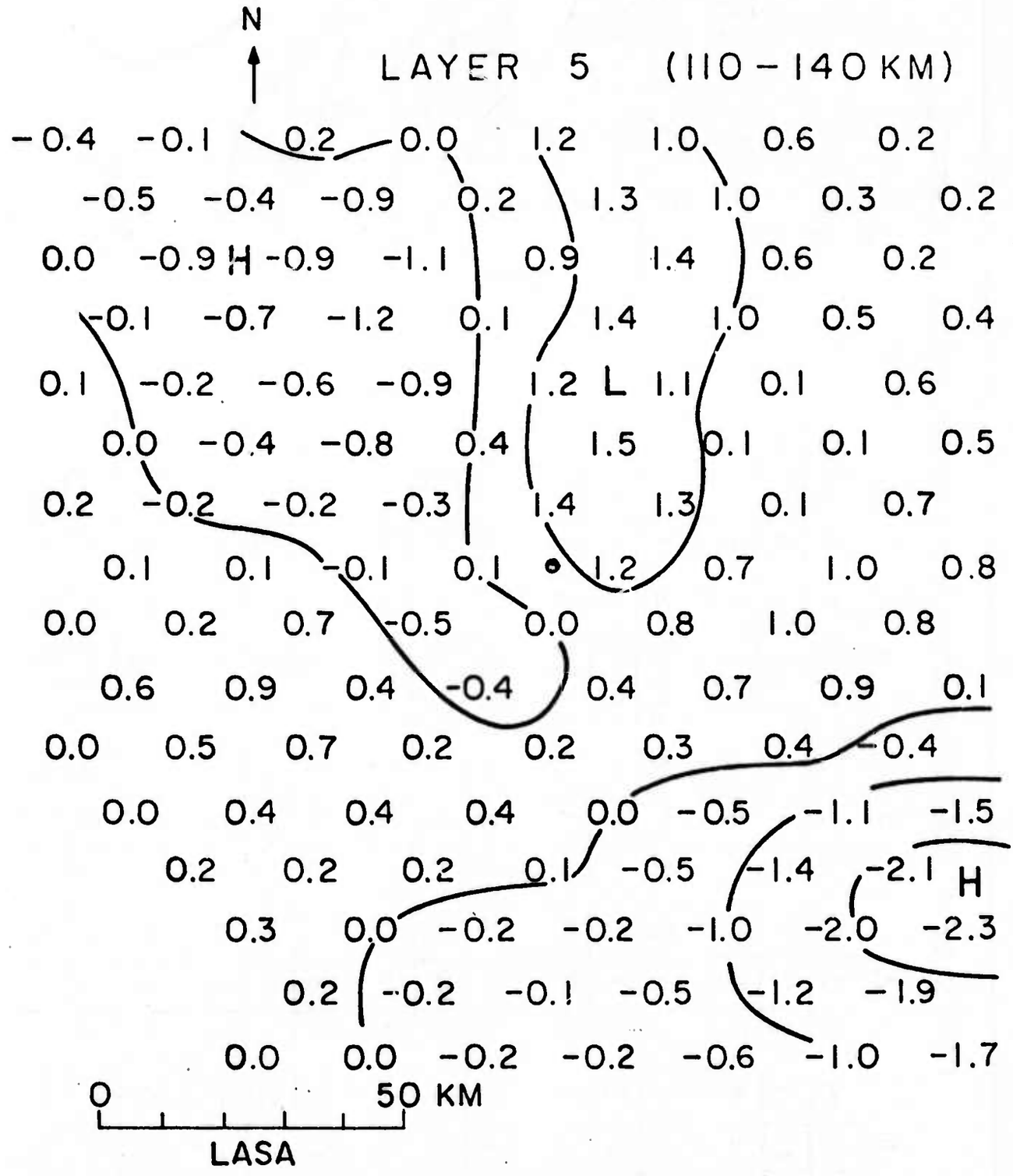
N
LAYER 5 (110 – 140 KM)
-0.4 -0.1 0.2 0.0 1.2 1.0 0.6 0.2
-0.5 -0.4 -0.9 0.2 1.3 1.0 0.3 0.2
0.0 -0.9 H -0.9 -1.1 0.9 1.4 0.6 0.2
-0.1 -0.7 -1.2 0.1 1.4 1.0 0.5 0.4
0.1 -0.2 -0.6 -0.9 1.2 L 1.1 0.1 0.6
0.0 -0.4 -0.8 0.4 1.5 0.1 0.1 0.5
0.2 -0.2 -0.2 -0.3 1.4 1.3 0.1 0.7
0.1 0.1 -0.1 0.1 1.2 0.7 1.0 0.8
0.0 0.2 0.7 -0.5 0.0 0.8 1.0 0.8
0.6 0.9 0.4 -0.4 0.4 0.7 0.9 0.1
0.0 0.5 0.7 0.2 0.2 0.3 0.4 -0.4
0.0 0.4 0.4 0.4 0.0 -0.5 -1.1 -1.5
0.2 0.2 0.2 0.1 -0.5 -1.4 -2.1 H
0.3 0.0 -0.2 -0.2 -1.0 -2.0 -2.3
0.2 -0.2 -0.1 -0.5 -1.2 -1.9
0.0 0.0 -0.2 -0.2 -0.6 -1.0 -1.7
0 50 KM
LASA

FIG 13

PARTS OF RESOLUTION MATRIX NEAR DIAGONAL ELEMENTS

LAYER	A	A	B	C	C
1	-4 -3 -4 -7 **84** -7 -8 -8 -8	0 0 1 1 0 1 0 1 1	-1 1 1 0 4 3 4 2	1 2 1 2 4 3 1 3 1	1 0 0 0 0 0 1 1 2
2	-2 1 -1 3 5 2 1 2 2	-1 1 2 1 3 0 0 2 0	-3 -7 -5 -6 **87** -6 -1 -6 -5	-5 -6 -4 -6 **90** -6 -4 -6 -5	1 2 1 1 3 1 -1 1 1
3	3 1 2 0 0 1 0 0 1	-5 -7 -4 -6 **82** -6 -4 -6 -3	2 2 0 3 3 1 1 2 1	1 2 1 1 3 2 0 2 1	-4 -6 -4 -6 **82** -5 -3 -6 -4
4	0 0 1 0 -1 0 0 -1 -1	1 5 1 1 5 1 -1 2 0	3 0 1 3 0 0 1 0 1	2 2 1 1 0 1 1 2 1	1 3 0 3 5 2 -1 2 2
5	-1 0 0 -1 -1 -1 0 -1 -1	4 4 3 2 -1 0 1 1 0	1 1 1 1 0 0 1 1 0	0 0 0 0 -1 0 1 0 0	3 2 2 4 0 1 2 2 3

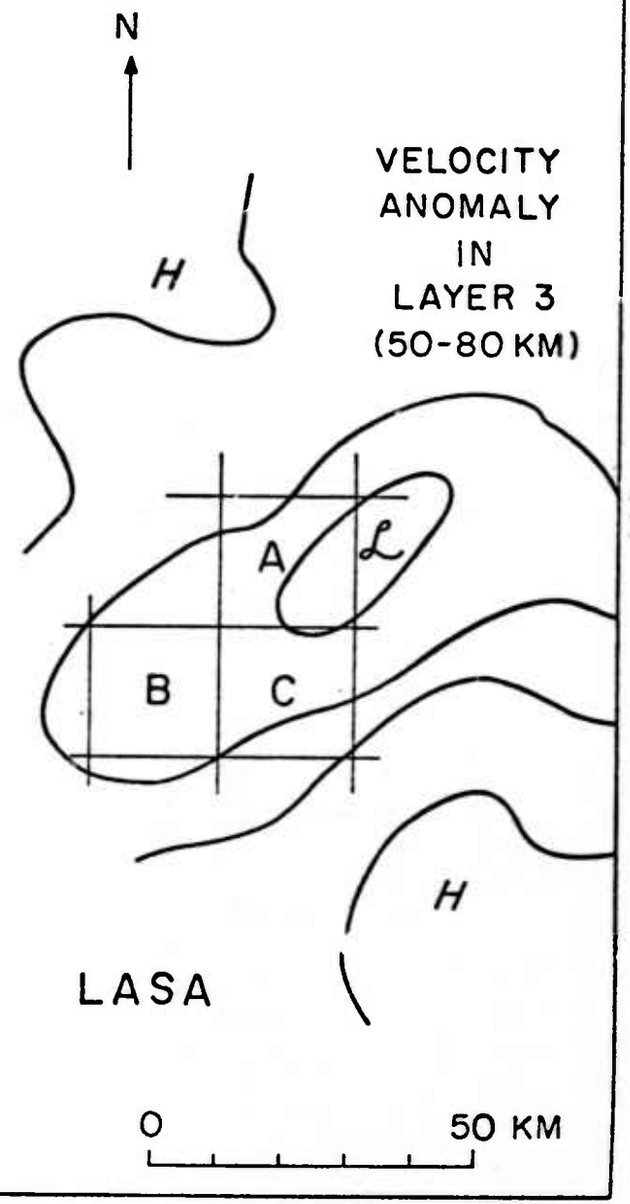

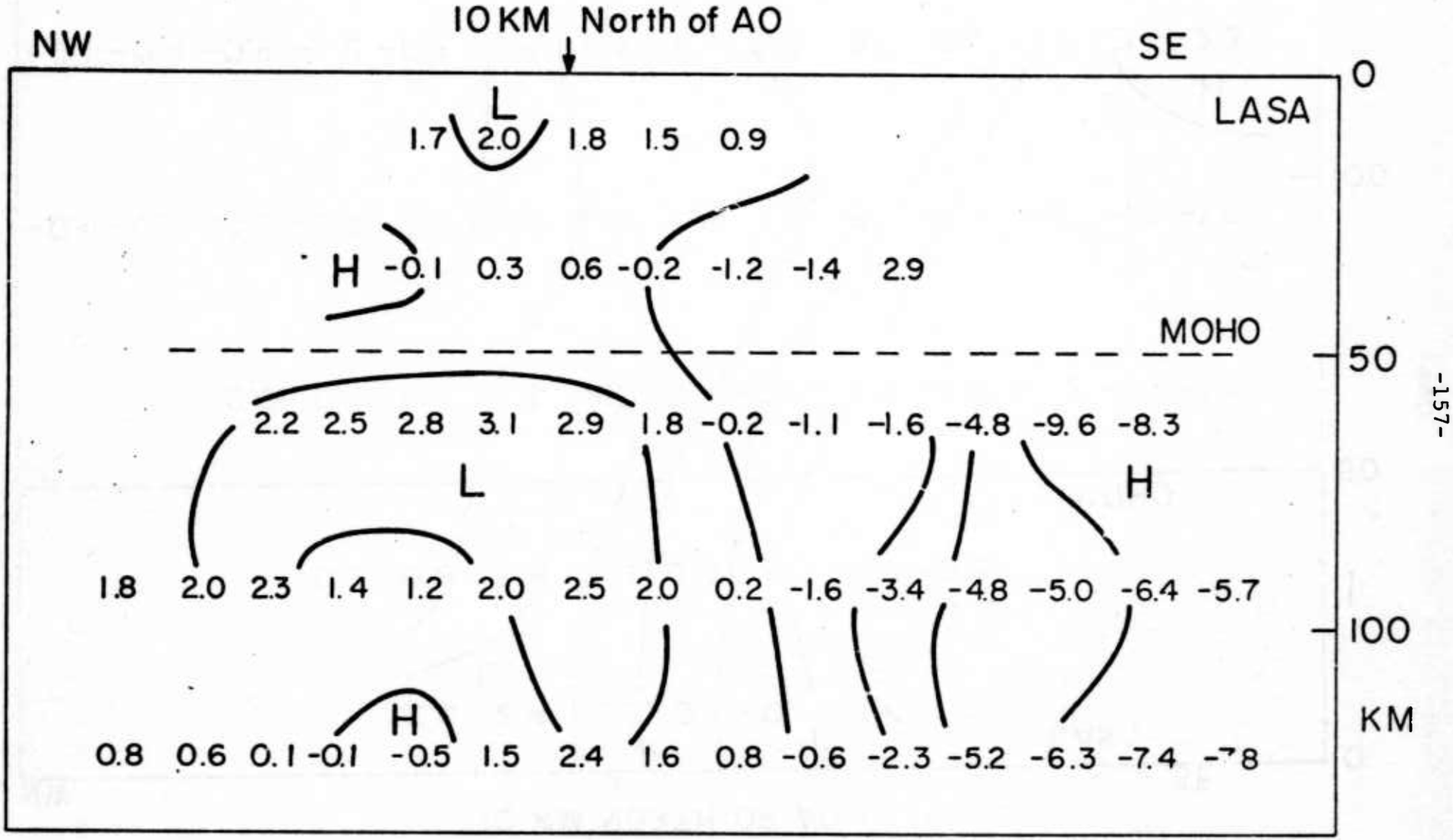
10 KM North of AO
NW
SE
0
LASA
L
1.7 2.0 1.8 1.5 0.9
H -0.1 0.3 0.6 -0.2 -1.2 -1.4 2.9
MOHO
50
2.2 2.5 2.8 3.1 2.9 1.8 -0.2 -1.1 -1.6 -4.8 -9.6 -8.3
L
H
1.8 2.0 2.3 1.4 1.2 2.0 2.5 2.0 0.2 -1.6 -3.4 -4.8 -5.0 -6.4 -5.7
100
H
KM
0.8 0.6 0.1 -0.1 -0.5 1.5 2.4 1.6 0.8 -0.6 -2.3 -5.2 -6.3 -7.4 -7.8

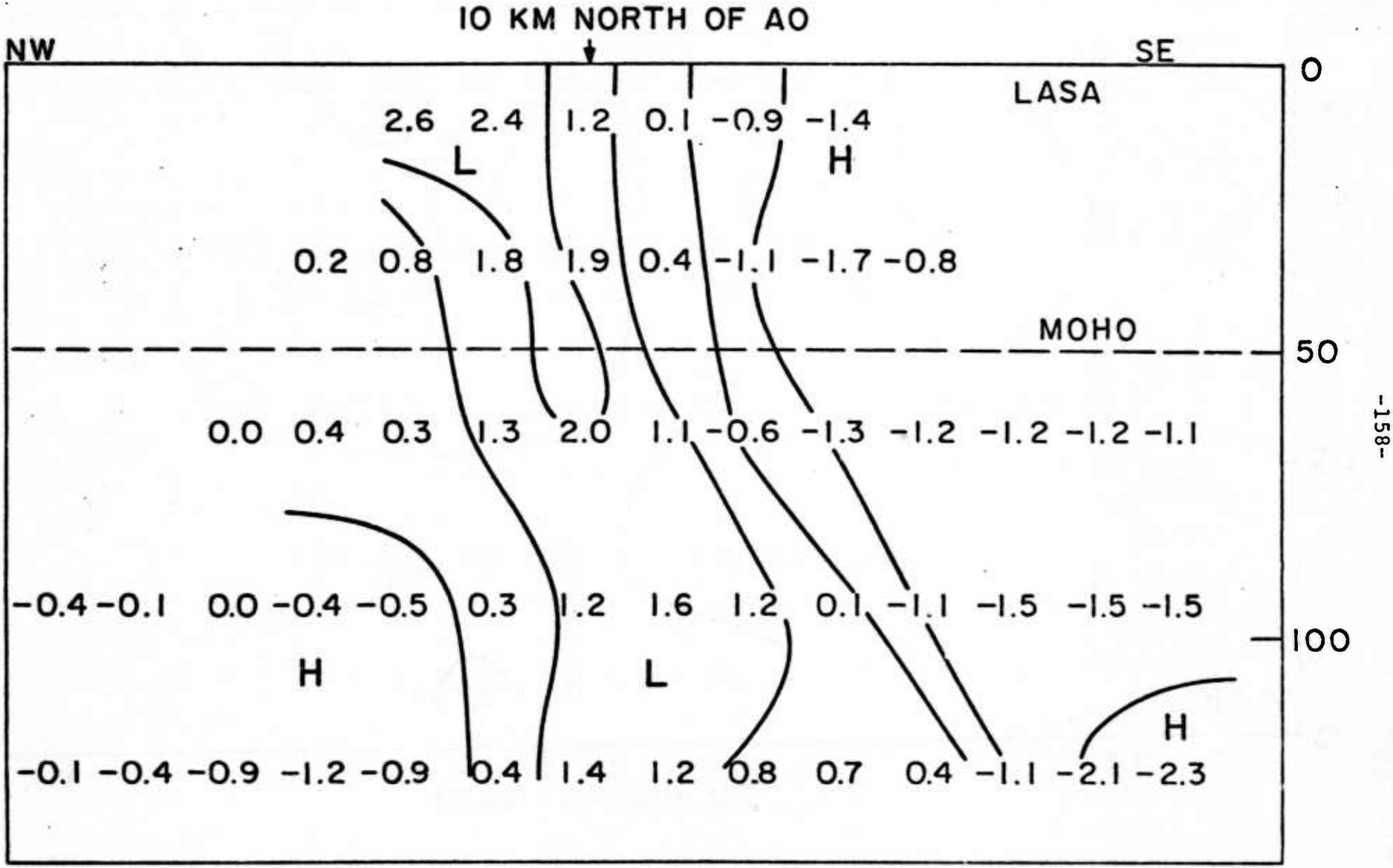
10 KM NORTH OF AO
NW
SE
LASA
0
50
100
MOHO
2.6 2.4 1.2 0.1 -0.9 -1.4
L
H
0.2 0.8 1.8 1.9 0.4 -1.1 -1.7 -0.8
0.0 0.4 0.3 1.3 2.0 1.1 -0.6 -1.3 -1.2 -1.2 -1.2 -1.1
-0.4 -0.1 0.0 -0.4 -0.5 0.3 1.2 1.6 1.2 0.1 -1.1 -1.5 -1.5 -1.5
H
L
H
-0.1 -0.4 -0.9 -1.2 -0.9 0.4 1.4 1.2 0.8 0.7 0.4 -1.1 -2.1 -2.3

4.4 Elevation of the Olivine-Spinel Phase Change in Subducted Lithosphere: Seismic Evidence by S.C. Solomon and K.T. Paw U

ABSTRACT

The top of the olivine-spinel phase change in subducted oceanic lithosphere can be located by the travel times of seismic waves which have propagated through the slab. P-wave travel time residuals from deep earthquakes in the Tonga island arc observed at Australian seismic stations are grouped according to the depth of the earthquake. The change in mean residuals with a change in earthquake depth is related to the velocity contrast between slab and normal mantle at that depth. The curve mean residual versus earthquake depth displays a region of markedly increased slope between earthquake depths of about 250 and 350 km. The most probable explanation of this observation is an elevation by 100 km of the olivine-spinel phase change within the relatively cooler slab. No evidence was found for vertical displacements within the slab of any deeper phase changes.

A temperature contrast between slab and normal mantle of about 1000°C at 250 km depth is implied. This finding confirms current thermal models for subducted lithosphere but is inconsistent with the global intraplate stress field unless only a few percent of the negative buoyancy force at subduction zones is transmitted to the surface plates.

4.5 P Wave Travel Times from Deep Earthquakes by M.K. Sengupta and B.R. Julian

ABSTRACT

A study of teleseismic P wave travel times has been made using data from deep (450-650 km) earthquakes exclusively, for which the effect of near source upper mantle heterogeneity is expected to be small and location parameters are considered reliable. About 3,300 arrival times selected from bulletins and winnowed to remove discrepant data, were used. The shape of the travel time curve and the average station anomalies found are in general agreement with the results of other works (e.g. Herrin et al., 1968) but the scatter of the data is only about half as large (∿0.6 sec), verifying that deep earthquakes are indeed more suitable than shallow ones for travel time studies. The shape of the travel time curve is determined within 0.1-0.2 seconds out to epicentral distances of 70°, but the absolute level of the curve remains uncertain within about ±1 second. This 'baseline correction' has been estimated from Nevada Test Site explosion data, for which the upper mantle velocity structure near the source is known and could be corrected for. The results of this procedure indicate that the Jeffreys-Bullen (1940) times are about 1.5 seconds late but the model of Herrin et al. (1968) has approximately the correct baseline of P travel times at least for focal depth of 550 km.

The station anomalies of this study, represented by a constant, correlate very well with large-scale tectonic features and also give a better fit to the travel time data than has been achieved in other studies which included azimuthal station terms.

Systematic regional variations in travel time of 1 second or more occur beyond 70°, and indicate that significant lateral variation occurs in the lower mantle (depth > 2000 km). A conservative lower bound of about 1% can be placed on the magnitude of these variations in compressional velocity.

4.6 Three Dimensional Model of Seismic Velocity Variation in the Earth's Mantle by M.K. Sengupta and M.N. Toksöz

Three dimensional velocity models for the earth's mantle were obtained satisfying P, S and some PcP and ScS travel time anomalies from deep focus earthquakes. A method of successive approximation was used to compute the uniform relative velocity perturbation over three dimensional blocks of size 10°x10° in longitude and latitude, and 500 km in thickness. Features of these velocity perturbations indicated that lateral heterogeneity is the most pronounced in the upper mantle and near the core-mantle boundary. The upper mantle anomalies are correlated with surface tectonic features but these are not correlated with deep mantle anomalies.

Global and regional analyses of geophysical data indicate that there are lateral heterogeneities in the earth's upper mantle as well as in the lower mantle (Toksöz et al., 1967; Davies and Sheppard, 1972; Julian and Sengupta, 1973; Jordan and Lynn, 1974; Wright and Lyons, 1975). In this paper we present three dimensional seismic velocity models of the earth's mantle derived from good quality P, S and some PcP and ScS travel time data from deep focus earthquakes. In earlier papers Davies and Sheppard (1972) and Julian and Sen Gupta (1973), using array diagram and travel time anomalies along different ray bundles, concluded that the lowermost mantle (2000-3000 km) is comparatively more heterogeneous laterally than the middle mantle (1000-2000 km). In the present paper, we look at the inverted model for the whole mantle which was divided into blocks. Since velocity variations are generally small we determine percentage perturbation of velocities relative to an average model.

Data

Travel times of compressional (P), shear (S), and some core-reflected phases (PcP, ScS) data were read from World Wide Seismic Station Network (WWSSN) seismograms of 12 deep focus (depth > 500 km) earthquakes under the Indonesian arc, Solomon Islands, New Hebrides, Kuril arc, Tonga arc, and western coast of South America. To expand the global coverage,

we also included data from two intermediate depth earthquakes from Greece and Hindikush. To increase the ray path distributions, we selected P wave arrivel time data from international bulletins for cther stations around the world. All of the travel time data from these 14 earthquakes were assumed to be free from any severe source bias as these earthquakes were among the deepest ones in the respective Benioff zones. The earthquakes were relocated after constraining the depths from readings of the depth phases (pP, sP).

Method of Inversion

The observed travel times, averaged over 2° distance cells, were fitted first with an average radial velocity model. Then, the difference between the observed and calculated travel times was averaged for each station to obtain the "station anomalies". The "station anomalies" incorporate the crustal anomalies and the short wavelength lateral variations in the upper mantle. The remaining travel time anomalies were fitted through constant velocity perturbations in three dimensional blocks of sizes 10° in longitude, 10° in latitude, and 500 km in thickness. About 2000 such blocks were sampled by 1490 P and PcP travel time data and 1400 blocks by 314 S and ScS travel time data.

To compute the velocity perturbation in each block, we used a method of successive approximation. In this method,

the rth approximation of the velocity perturbation for the mth block (= p_m^r) is given by the weighted least square solution of the system of n linear equations of the form:

$$\Delta T_{ij}^{obs} + c_{ij}^r = K_{ijm}^r \, p_m^r \qquad (1)$$

where n is the number of ray paths passing through the mth block, ΔT_{ij}^{obs} is the observed travel time anomaly for ith earthquake and jth station, c_{ij}^r is the rth approximation of the correction to ΔT_{ij}^{obs} for the perturbation of velocity in other blocks, K_{ijm}^r is the rth approximation of "data kernel" of the mth block corresponding to ΔT_{ij}^{obs}. These data kernels are actually the calculated travel times of the corresponding rays in the given block. During the computation of velocity perturbation, weights were given to each datum according to the fraction of the total travel time the ray spends in the given block. The computed relative velocity perturbation was also constrained not to exceed 5% (or 1% if there is only one datum) in any individual cycle of iteration. Altogether three cycles were performed before convergence was reached.

The model in our method of inversion depends on the sequence in which the respective blocks were chosen during inversion. So, three different sequences were chosen. In the first trial (MODEL 1), the blocks were sequenced in an ordered way starting from the core-mantle boundary and terminating on the free surface; in the second trial (MODEL 2)

the above sequence was reversed. Finally in MODEL 3, the blocks were sequenced randomly. After fit through these three dimensional models, r.m.s. deviation of 1490 P-wave travel time residuals was about 0.4 seconds, comparable to the standard deviation of the reading error. Since S-wave travel time data are fewer than those of P-waves (314 vs. 1490), the S-wave data were overfitted by the models and produced r.m.s. deviation of only 0.2 seconds.

Result of Inversion

As the absolute magnitude of the velocity perturbation depends on the size and sampling of the blocks, we discuss only the "relative variation" of the velocity perturbations with depth (Fig. 1) and with latitude and longitude (Fig. 2). The velocity perturbations for the surface layer (0-500 km) shown in these two figures include a contribution corresponding to the average of station anomalies in each block. All three models shown in Fig. 1 show a relative maximum for the surface layer (0-500 km) and for the layer near the core-mantle boundary indicating that these two layers perhaps have the largest lateral heterogeneity of compressional waves. For shear waves, the greatest heterogeneity in the upper mantle (0-500 km) is verified by all models. Heterogeneity near the core-mantle boundary is not as clearly defined.

The compressional wave data have sufficiently broad

distribution to investigate the lateral variations of the velocities. In Fig.2 we show the relative P-wave velocity perturbations (in percent) in the upper mantle and near the core-mantle boundary. These velocity perturbations were obtained using inversion with random sequencing of blocks (MODEL 3). This figure illustrates that the pattern of P velocity anomalies for the upper mantle of our model is in agreement with other seismological data and tectonic features.

Generally the tectonically active regions are characterized by slower average velocities (negative perturbations) and shield areas by higher velocities (positive perturbations) in the outer 500 km. This is obvious in North America with a contrast between the eastern and western halves. In Africa and in Europe, shield areas stand out as regions of higher average velocities. The contrasts between the stable Indian shield and the Himalayas and Tibet and Southeast Asia are similar to those observed from surface wave studies (Bird and Toksöz, 1975). In Japan our results are similar to those obtained by Kanamori (1970) from regional studies and in Australia to those obtained by Cleary (1967). Since the top (0-500 km) layer is sampled directly under the stations, the data are confined to continental areas and to a few islands where seismic stations exist. Under Hawaii the average velocities are low. In oceanic areas there are no data.

For the core-mantle boundary region, it is difficult to

verify any model because of both scarcity of proper geophysical data and of ambiguity in interpretation of those data. In our P velocity model near the core-mantle boundary, the central Pacific region stands out as having small variation in velocity (within ±5%) compared to our spherically symmetric model.

Discussion and Conclusions

Inverted velocity models are dependent on the size of the blocks and the sampling, or the number of rays passing through each block. Block sizes must be chosen small enough to delineate anomalies, and large enough to have a sufficient number of rays passing through them. The block sizes chosen in this study (of the order of 500 km) are generally larger than scale lengths of mantle heterogeneities. Detailed studies of subduction zones (Toksöz et al., 1971) and the core-mantle boundary (Doornbos, 1975) indicate that scale length of heterogeneities in the earth's mantle is between 10-50 km. Thus our models grossly average over such smaller heterogeneities. Actual local perturbations could be much larger than those given in Figs. 1 and 2.

During the inversion, we found that the number of rays sampling each block also had an influence on the results. Blocks with few hits (<5) generally had two-fold larger velocity perturbations than the blocks sampled by more data. This is partly due to the artifact of inversion especially

for the blocks with only one hit. Another reason for it may lie in the largeness of the block size compared to the scale length of heterogeneity in the real earth as mentioned in the previous paragraph. Deleting the blocks with few hits (<5) did not alter the general picture. The relative variation of P wave velocity perturbations with depth followed a similar trend as shown in Fig. 1 (top).

The basic conclusions that are consistent with the analysis of our travel time data are:

(1) Lateral heterogeneity is most pronounced in the upper mantle and near the core-mantle boundary of the earth;

(2) In the upper mantle the velocity variations are correlated with tectonic features;

(3) Comparing the features of the P velocity model for the upper mantle with those near the core-mantle boundary, one finds no relationship between the surface tectonics and the deep mantle structure.

Acknowledgements

We thank Drs. A. Dziewonski, K. Aki and B. Julian for many constructive criticisms and suggestions. Computational facilities of Group 22 of Lincoln Laboratory (M.I.T.) and the ray tracing program of Dr. Bruce Julian were used in this study. The research was supported by the Advanced Research Projects Agency, monitored by the Air Force Office of Scientific Research under contracts F44620-71-C-0049 and F44620-75-C-0064.

References

Bird, P. and M.N. Toksöz, Structure and evolution of Tibetian Plateau, presented at the Annual Meeting, Amer. Geophys. Un., Washington, D.C., June 17, 1975.

Cleary, J., P times to Australian stations from nuclear explosions, Bull. Seism. Soc. Amer., 57, 773-781, 1967.

Davies, D. and R.M. Sheppard, Lateral heterogeneity in the earth's mantle, Nature, 239, 318-323, 1972.

Doornbos, D.J., Characteristics of lower mantle inhomogeneities from scattered waves, presented at the Annual Meeting, Amer. Geophys. Un., Washington, D.C., June 16, 1975.

Jordan, T.H. and W.S. Lynn, A velocity anomaly in the lower mantle, J. Geophys. Res., 79, 2679-2685, 1974.

Julian, B.R. and M.K. Sengupta, Seismic travel time evidence for lateral inhomogeneity in the deep mantle, Nature, 242, 243-247, 1973.

Kanamori, H., Velocity and Q of mantle waves, Phys. Earth Planet. Interiors, 2, 259-275, 1970.

Toksöz, M.N., M. Chinnery and D.L. Anderson, Inhomogeneities in the earth's mantle, Geophys. J. Roy. Astron. Soc., 13, 31-59, 1967.

Toksöz, M.N., J. Minear and B.R. Julian, Temperature field and geophysical effects of a downgoing slab, J. Geophys. Res., 76, 1113-1138, 1971.

Wright, C. and J.A. Lyons, Seismology $dT/d\Delta$ and deep mantle convection, Geophys. J. Roy. Astron. Soc., 40, 115-138, 1975.

Figure Captions

Figure 1. R.m.s. relative perturbations (in percent) of P and S wave velocity for each 500 km depth interval.

Figure 2. Three dimensional P wave velocity models for the upper mantle and for near the core-mantle boundary. Each color represents a range in relative velocity perturbation (in percent). The positive values in relative velocity perturbation correspond to higher velocity than spherically symmetric model and the negative perturbation to lower velocity.

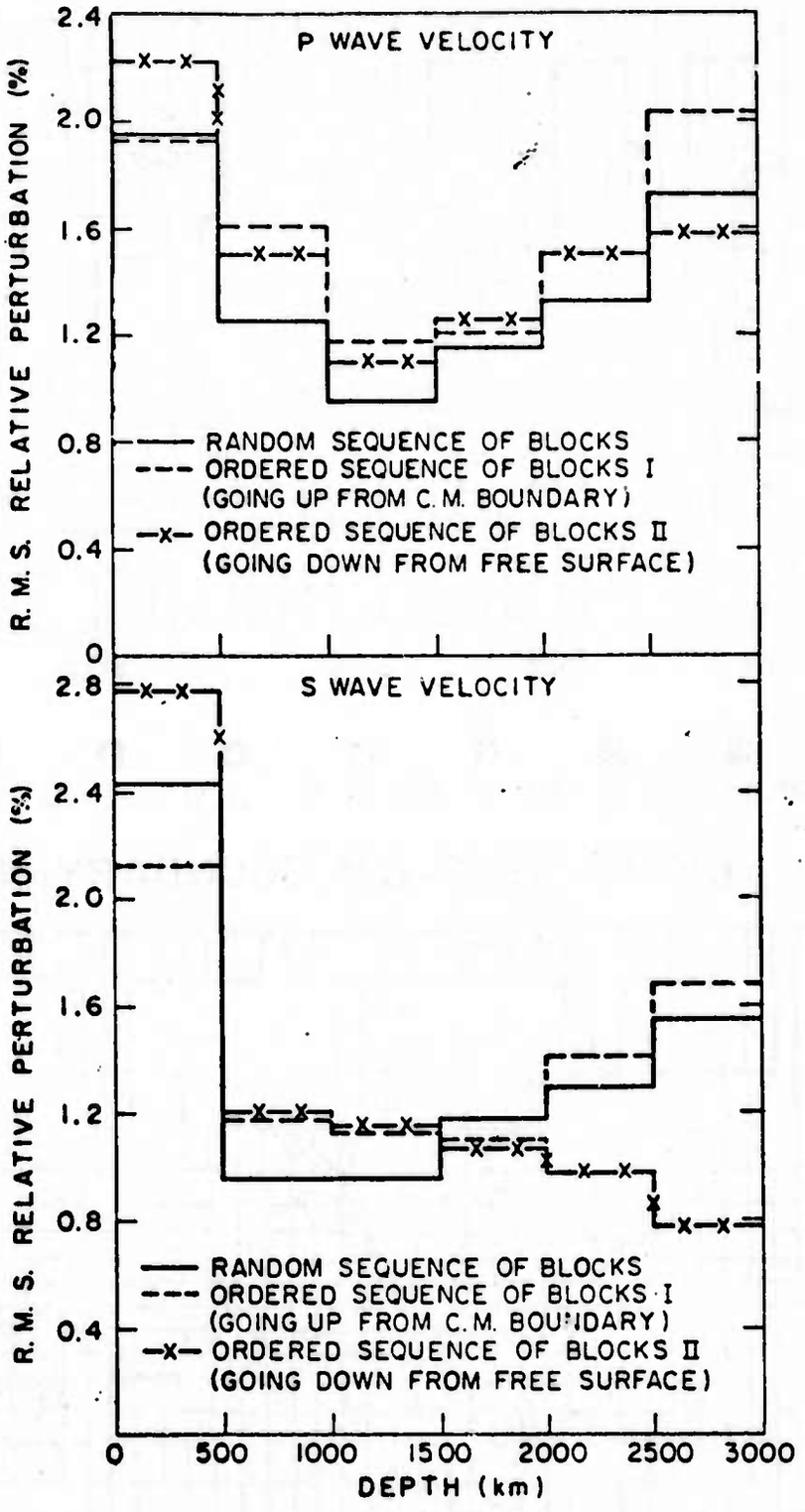
P WAVE VELOCITY
R. M. S. RELATIVE PERTURBATION (%)
2.4
2.0
1.6
1.2
0.8
0.4
0
RANDOM SEQUENCE OF BLOCKS
ORDERED SEQUENCE OF BLOCKS I
(GOING UP FROM C. M. BOUNDARY)
ORDERED SEQUENCE OF BLOCKS II
(GOING DOWN FROM FREE SURFACE)
S WAVE VELOCITY
R. M. S. RELATIVE PERTURBATION (%)
2.8
2.4
2.0
1.6
1.2
0.8
0.4
RANDOM SEQUENCE OF BLOCKS
ORDERED SEQUENCE OF BLOCKS I
(GOING UP FROM C.M. BOUNDARY)
ORDERED SEQUENCE OF BLOCKS II
(GOING DOWN FROM FREE SURFACE)
0
500
1000
1500
2000
2500
3000
DEPTH (km)

Figure 1

DEPTH 0-500 km

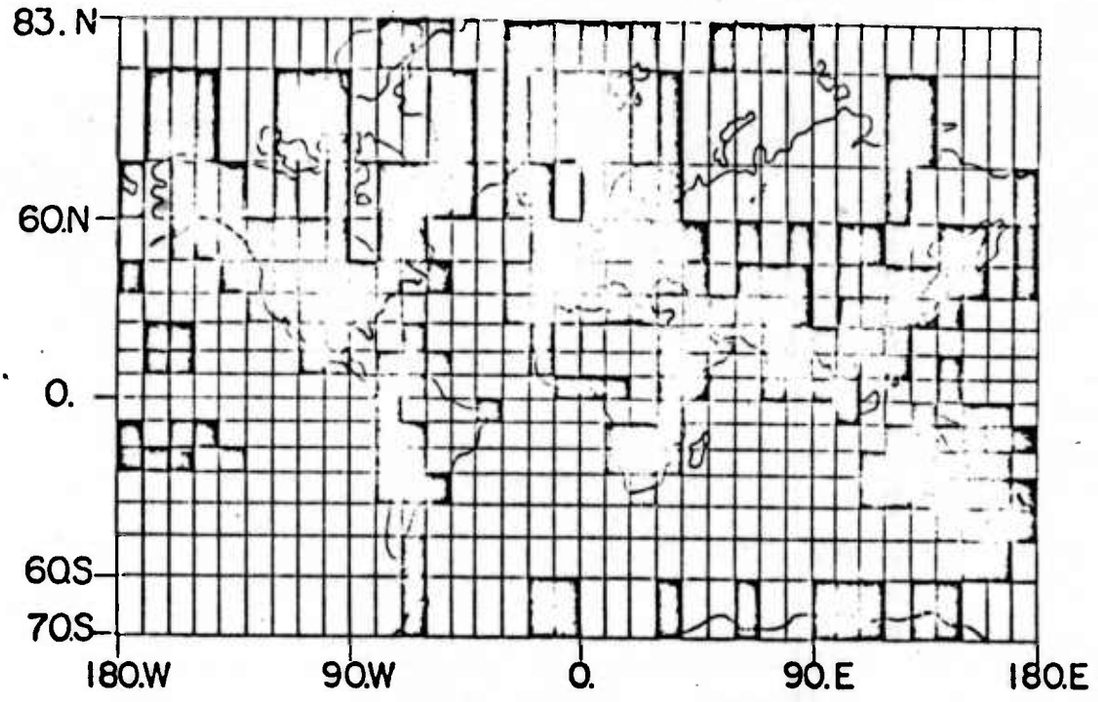

<-2.0% to -2.0 to -1.0 to -0.5 to 0 to 0.5 to 1.0 to 2.0 to >2.0%

DEPTH 2500-C.M. BOUNDARY (IN km)

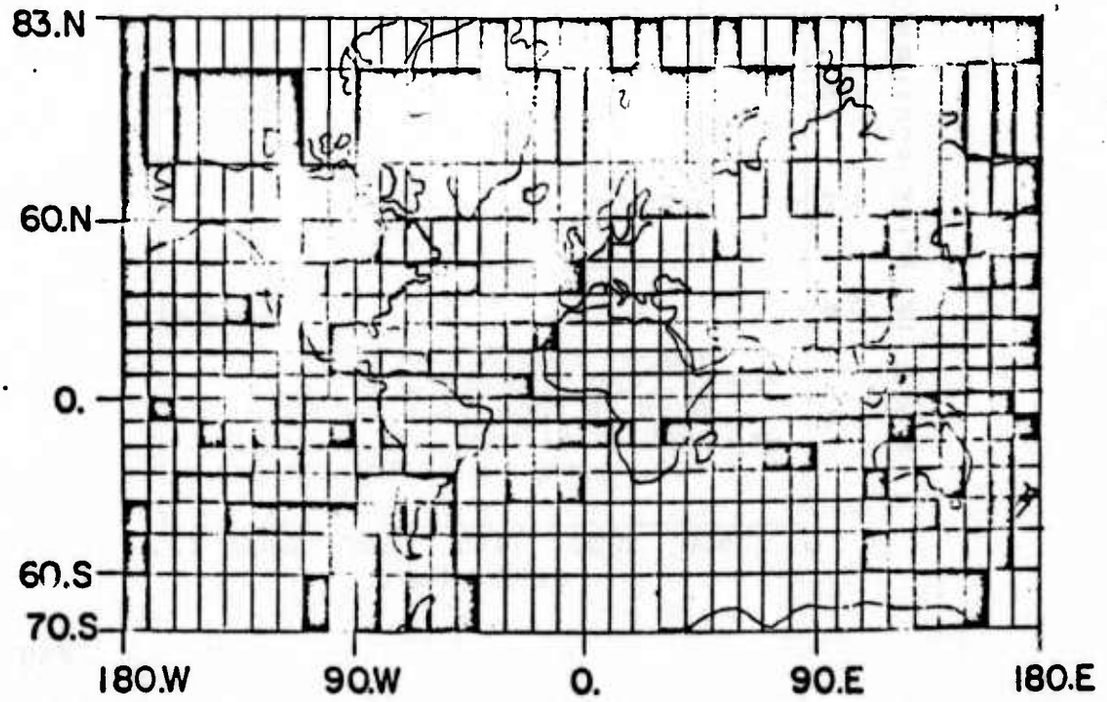

5. SCATTERING AND ATTENUATION

5.1 Origin of Coda Waves: Source, Attenuation, and Scattering Effects by K. Aki and B. Chouet

Coda waves from small local earthquakes are interpreted as backscattering waves from numerous heterogeneities distributed uniformly in the earth's crust. Two extreme models of the wave medium that account for the observations on the coda are proposed. In the single backscattering model the scattering is considered to be a weak process, and the loss of seismic energy by scattering is neglected. In the diffusion model the seismic energy transfer is considered as a diffusion process. Both models lead to similar formulas that allow an accurate separation of the effect of earthquake source from the effects of scattering and attenuation on the coda spectra. A unique difference was found in the scaling law of earthquake source spectra between central California and western Japan, which may be attributed to the difference in inhomogeneity length of the earth's crust. The Q of coda waves in the two regions is strongly frequency dependent with values increasing from 50-200 at 1 Hz to about 1000-2000 at 20 Hz. This observation is interpreted as a combined effect of variation of Q with depth and frequency-dependent composition of coda waves described below. The turbidity coefficient of the lithosphere required at 1 Hz to explain

the observed coda as body wave scattering is orders of magnitude greater than previously known values such as those obtained by Aki (1973) and Capon (1974) under the Montana LASA from the amplitude and phase fluctuations of teleseismic P waves. From the high attenuation and turbidity obtained at this frequency we conclude that at around 1 Hz the coda is made of backscattering surface waves from heterogeneities in the shallow, low-Q lithosphere. The high Q observed for the coda at frequencies higher than 10 Hz, on the other hand eliminates the possibility that these waves are backscattering surface waves. We conclude that at these high frequencies the coda must be made of backscattering body waves from heterogeneities in the deep lithosphere. The low turbidities found for deep earthquake sources under western Japan are consistent with this model of coda wave generation.

5.2 Synthesis of Teleseismic P-waves from Sources near Sinking Lithospheric Slabs by R.W. Ward and K. Aki

ABSTRACT

A wave theory method is used to determine the effect of a sinking lithospheric slab on short-period and long-period waves. We consider a simplified model of the lithospheric slab with a 10% velocity contrast and compute both short-period and long-period theoretical seismograms from a P-wave source located in or near the slab. For this model, the ray-theoretical amplitude agrees quite well with the short-period amplitude. In the ray-theoretical shadow zone the long-period seismograms typically have amplitudes 50% (or greater) of the direct P-wave amplitude and exhibit waveform broadening. Similar waveform broadening has been attributed to the dynamics of earthquake faulting. The effect of the lithosphere on long-period waves from nearby sources must be taken into account in studies which utilize the observed variation in waveform broadening to infer earthquake source dynamics.

5.3 Inversion Schemes for Surface Wave Attenuation and Q in the Crust and the Mantle by W.B. Lee and S.C. Solomon

Seismic wave attenuation, or Q^{-1}, is one of the parameters traditionally used to distinguish lithosphere from asthenosphere. As a means of inverting surface wave attenuation measurements to obtain Q^{-1} as a function of depth, a classical linear inverse problem, we introduce a set theoretical approach. The set theoretical approach includes both the square matrix inverse and the linear programming method, which agree in concept but differ in that the constraints consist of mean or extreme hyperplanes, respectively. The set theoretical approach to inverting attenuation observations has two advantages: (1) The lithosphere thickness may be readily estimated using a geometric visualization of the square matrix inverse, which identifies the feasibility of a solution. (2) The approach allows more strict regulation of solution parameters than does the least square inverse, which often leads to a negative solution for inaccurate and sparse attenuation data. We apply the set theoretical approach to inverting the measured attenuation of Love and Rayleigh waves in western and east-central United States. Identifying the base of the lithosphere as the depth at which Q^{-1} increases sharply, we obtain lithosphere thicknesses of 80±20 km and 130±30 km in the two regions, respectively. Q^{-1} in the asthenosphere is about a factor

of 2 greater beneath western than east-central United States. A decrease in Q^{-1} with depth in the lithosphere is resolvable in both regions.

6. PUBLICATIONS DURING CONTRACT PERIOD

Abe, K., Fault parameters determined by near- and far-field data: The Wakasa-Bay earthquake of March 26, 1963, Bull. Seism. Soc. Am., 64, 1369-1382, 1974.

Abe, K., Seismic displacement and ground motion near a fault: The Saitama earthquake of September 21, 1931, J. Geophys. Res., 79, 4393-4399, 1974.

Abe, K., Determination of static and dynamic fault parameters: The Saitama earthquake of July 1, 1968, Tectonophysics, 27, 223-238, 1975.

Abe, K., A fault model for the Niigata earthquake of 1964, submitted to Phys. Earth Planet. Int., 1975.

Aki, K., Earthquake mechanism, in the Proceeding of the Final UMP Symposium, Tectonophysics, 13, 423-446, 1972.

Aki, K., Recent results on the mechanism of earthquakes with implications on the prediction and control program, Tectonophysics, 14, 227-243, 1972.

Aki, K., Scaling law of earthquake source-time function, Geophys. J. Roy. Astron. Soc., 31, 3-25, 1972.

Aki, K., Scattering of P waves under the Montana LASA, J. Geophys. Res., 78, 1334-1346, 1973.

Aki, K., M. Bouchon and P. Reasenberg, Seismic source function for an underground nuclear explosion, Bull. Seism. Soc. Am., 64, 131-148, 1974.

Aki, K. and B. Chouet, Origin of coda waves: source,

attenuation, and scattering effects, J. Geophys. Res., 80, 3322-3342, 1975.

Aki, K., A. Christoffersson, and E. Husebye, Determination of the three-dimensional seismic structure of the lithosphere, submitted to J. Geophys. Res., 1975.

Aki, K., A. Christoffersson, and E. Husebye, Three-dimensional seismic structure of the lithosphere under Montana LASA, Bull. Seism. Soc. Am., in press, 1975.

Ambuter, B.P. and S.C. Solomon, An event recording system for monitoring small earthquakes, Bull. Seism. Soc. Am., 64, 1181-1188, 1974.

Bird, P., M.N. Toksöz and N.H. Sleep, Thermal and mechanical models of continent-continent convergence zones, J. Geophys. Res., in press, 1975.

Brown, R., Precursory changes in V_P/V_S before strike-slip events, Proc. Conf. Tectonic Problems of the San Andreas Fault System, R.L. Kovach and A. Nur, eds., Geological Sciences, Vol. XIII, Stanford University, 1973.

Chapman, M.E. and S.C. Solomon, North American-Eurasian plate boundary in northeast Asia, J. Geophys. Res., in press, 1975.

Husebye, E., A. Christoffersson, K. Aki and C. Powell, Preliminary results on the three-dimensional seismic structure of the lithosphere under the USGS central California seismic array, to be submitted to Geophysical

J. Roy. Astron. Soc., 1975.

Ida, Y., Cohesive force across the edge of a longitudinal-shear crack and Griffith's specific surface energy, J. Geophys. Res., 77, 3796-3805, 1972.

Ida, Y., Cohesive force and unsteady propagation of a longitudinal-shear crack, Proceedings of the Conference on Dynamic Crack Propagation, Lehigh University, July, 1972.

Ida, Y., Stress concentration and unsteady propagation of longitudinal-shear cracks, J. Geophys. Res., 78, 3429, 1973.

Ida, Y., On the maximum acceleration of the near-field seismic records, Bull. Seism. Soc. Am., 63, 959-968, 1973.

Julian, B.R. and M.K. Sengupta, Seismic travel time evidence for lateral inhomogeneity in the deep mantle, Nature, 242, 443-447, 1973.

Kuster, G. and M.N. Toksöz, Velocity and attenuation of seismic waves in two-phase media: I. Theoretical formulations, Geophysics, 39, 587-606, 1974.

Lee, W.B. and S.C. Solomon, Inversion schemes for surface wave attenuation and Q in the crust and the mantle, Geophys. J. Roy. Astron. Soc., in press, 1975.

Madariaga, R.I., Toroidal free oscillations of the laterally heterogeneous earth, Geophys. J. Roy. Astron. Soc.,

27, 81-100, 1972.

Madariaga, R.I., Dynamics of an expanding circular fault, submitted to Bull. Seism. Soc. Am., 1975.

Madariaga, R.I. and K. Aki, Spectral splitting of toroidal free oscillations due to lateral heterogeneity of earth structure, J. Geophys. Res., 77, 4421-4431, 1972.

Reasenberg, P. and K. Aki, A precise, continuous measurement of seismic velocity for monitoring in situ stress, J. Geophys. Res., 79, 399-406, 1974.

Richter, F.M. and B. Parsons, On the interaction of two scales of convection in the mantle, J. Geophys. Res., 80, 2529-2541, 1975.

Rosenman, M. and S.J. Singh, Quasi-static strains and tilts due to faulting in a viscoelastic half-space, Bull. Seism. Soc. Am., 63, 1737-1752, 1973.

Rosenman, M. and S.J. Singh, Stress relaxation in a semi-infinite viscoelastic earth model, Bull. Seism. Soc. Am., 63, 2145-2154, 1973.

Sengupta, M.K. and B.R. Julian, P wave travel times from deep earthquakes, submitted to Bull. Seism. Soc. Am., 1975.

Sengupta, M.K. and B.R. Julian, Radial variation of compressional and shear velocities in the earth's lower mantle, to be submitted to Geophys. J. Roy. Astron. Soc., 1975.

Sengupta, M.K. and M.N. Toksöz, Three dimensional model of seismic velocity variation in the earth's mantle,

Geophys. Res. Lett., submitted, 1975.

Sengupta, M.K. and M.N. Toksöz, The amplitudes of P waves and magnitude corrections for deep focus earthquakes, J. Geophys. Res., to be submitted, 1975.

Shlien, S., Earthquake-tide correlation, Geophys. J. Roy. Astron. Soc., 28, 27-34, 1972.

Shlien, S. and M.N. Toksöz, Automatic event detection and location capabilities of large aperture seismic arrays, Bull. Seism. Soc. Am., 63, 1275-1288, 1973.

Shlien, S. and M.N. Toksöz, Automatic phase identification with one and two large aperture seismic arrays, Bull. Seism. Soc. Am., 64, 221-233, 1974.

Singh, S.J., Generation of SH-type motion by torsion-free sources, Bull. Seism. Soc. Am., 63, 1189-1200, 1973.

Singh, S.J. and M. Rosenman, On the disturbance due to a spherical distortional pulse in an elastic medium, Pure and Appl. Geophys., 110, 1946-1954, 1973.

Singh, S.J. and M. Rosenman, Quasi-static deformation of a viscoelastic half-space by a displacement dislocation, Phys. Earth Planet. Interiors, 8, 87-101, 1974.

Smith, A.T., Jr., and M.N. Toksöz, Stress distribution beneath island arcs, Geophys. J. Roy. Astron. Soc., 29, 289-318, 1972.

Solomon, S.C., Seismic-wave attenuation and partial melting in the upper mantle of North America, J. Geophys. Res.,

77, 1483-1502, 1972.

Solomon, S.C., On Q and seismic discrimination, Geophys. J. Roy. Astron. Soc., 31, 163-177, 1972.

Solomon, S.C., Shear wave attenuation and melting beneath the Mid-Atlantic ridge, J. Geophys. Res., 78, 6044-6059, 1973.

Solomon, S.C. and R.G. Butler, Prospecting for dead slabs, Earth Planet. Sci. Lett., 21, 421-430, 1974.

Solomon, S.C. and B.R. Julian, Seismic constraints on ocean-ridge mantle structure: anomalous fault-plane solutions from first motions, Geophys. J. Roy. Astron. Soc., 38, 265-285, 1974.

Solomon, S.C. and K.T. Paw U, Elevation of the olivine-spinel phase change in subducted lithosphere: seismic evidence, Phys. Earth Planet. Interiors, submitted, 1975.

Toksöz, M.N., Subduction of the lithosphere and the causes of deep focus earthquakes, in press, 1975.

Toksöz, M.N. and H.H. Kehrer, Tectonic strain release by underground nuclear explosions and its effect on seismic discrimination, Geophys. J. Roy. Astron. Soc., 31, 141-161, 1972.

Toksöz, M.N., N. Sleep, and A.T. Smith, Evolution of the downgoing lithosphere and the mechanisms of deep focus earthquakes, Geophys. J. Roy. Astron. Soc., 35, 285-310, 1973.

Ward, R.W., Response of transition zones to nearby sources, Geophys. J. Roy. Astron. Soc., 35, 311-325, 1973.

Ward, R.W. and K. Aki, Synthesis of teleseismic P-waves from sources near sinking lithospheric slabs, Bull. Seism. Soc. Am., in press, 1975.

Wiggins, R.A., G.A. McMechan and M.N. Toksöz, The range of earth structure nonuniqueness implied by body-wave observations, Rev. Geophys. Space Phys., 11, 87-113, 1973.

7. THESES COMPLETED DURING CONTRACT PERIOD

Brown, R.L., A dislocation approach to plate interaction, Ph.D. Thesis, M.I.T., August 1975.

Chapman, E.D., Structure and tectonics of the Arctic region, S.M. Thesis, M.I.T., June 1973.

Johnson, C.E., Regionalized earth models from linear programming methods, M.S. Thesis, M.I.T., September 1972.

Madariaga, R.I., Free oscillations of the laterally heterogeneous earth, Ph.D. Thesis, M.I.T., 1971.

Sengupta, M.K., A travel-time study using deep-focus earthquakes, M.S. Thesis, M.I.T., 1972.

Sengupta, M.K., The structure of the earth's mantle from body wave observations, Ph.D. Thesis, M.I.T., May 1975.

Shlien, S., Automatic classification of seismic detections from large aperture seismic array, Dr. Sc. Thesis, M.I.T., 1972.

Sleep, N.H., Deep structure and geophysical processes beneath island arcs, Ph.D. Thesis, M.I.T., January 1973.

Smith, A.T., Jr., Time-dependent strain accumulation and release at island arcs: Implications for the 1946 Nankaido earthquake, Ph.D. Thesis, M.I.T., 1974.

Wang, C.F., Elastic wave propagation in homogeneous transversely isotropic medium with symmetry axis parallel to the free surface, S.M. Thesis, M.I.T., September 1975.

Ward, R.W., Synthesis of teleseismic P waves from sources near transition zones, Ph.D. Thesis, M.I.T., 1971.